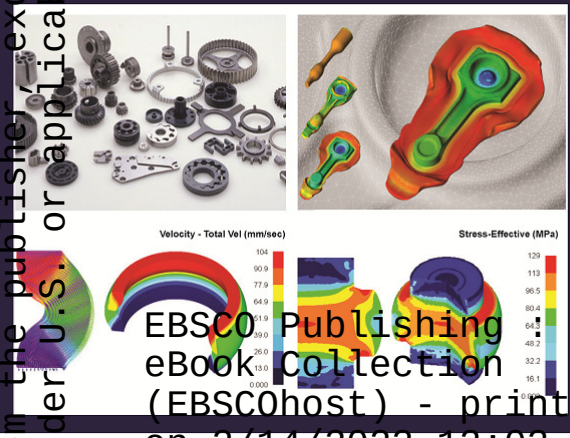

Dr. Saranjit Singh, Ph. D.
Dr. Polymersetty Chandrasekhar, Ph. D.

MECHANICAL PROCESSING OF SINTERED MATERIALS

PART 2: FINITE ELEMENT ANALYSIS OF SINTER-FORGING PROCESSES

Sciendo

Dr. SARANJIT SINGH, Ph.D
Dr. P. CHANDRASEKHAR, Ph.D

MECHANICAL PROCESSING OF SINTERED MATERIALS

PART-2:

FINITE ELEMENT ANALYSIS OF SINTER-FORGING PROCESSES

School of Mechanical Engineering
KIIT Deemed to be University
Bhubaneswar - 751024 (Odisha), India

ISBN: 978-83-66675-20-9
https://doi.org/10.2478/9788366675216

sciendo

ACKNOWLEDGMENT

I acknowledge with deep sense of gratitude and profound regards to my guides Dr. S. Kumar and Dr. A.K. Jha for the unlimited support and guidance throughout my research career. Additionally, I am thankful to all my previous colleagues from Department of Production Engineering, BIT Mesra, Ranchi, Jharkhand for their kind co-operation during conduct of the necessary experimental work as shared in the present manuscript.

I also thank my present employer, KIIT Deemed to be University and all my colleagues from KIIT School of Mechanical Engineering for providing me adequate sustenance and inspiration to compile the book.

Last but not the least, I am thankful to my family members for the continuous encouragement to bring up the present book. Without their blessings, the present dream could not have been realized.

(Saranjit Singh)

ACKNOWLEDGMENT

I express my profound sense of reverence and deepest gratitude whole heartedly to my guide Dr. Saranjit Singh, Director (Industry Engagements & Placements) and Professor, School of Mechanical Engineering, KIIT University, Bhubaneswar for his constant guidance, support, motivation and untiring help during the course of my PhD. His in-depth knowledge, in the area of metal forming technology, PM topics has been extremely beneficial for me. He has given me enough freedom during my research, and always been nice to me. He has always been caring, a source of wisdom and motivation.

I also thank my present employer, KIIT Deemed to be University and all my colleagues from KIIT School of Mechanical Engineering for providing me adequate sustenance and inspiration to compile the book.

Last but not the least, I am thankful to my family members for the continuous encouragement to bring up the present book. Without their blessings, the present dream could not have been realized.

(P. Chandrasekhar)

PREFACE

Sinter-forging, which is the subject of study under the present thesis, has gained considerable importance in the recent past. It has evolved as an advanced manufacturing technique for producing high-performance and precise quality engineering components economically in metal working industry, because of its low manufacturing cost compared to conventional metal forming processes. It uses pressed and sintered metal powder preforms as starting material having porosity in order of 15-30 percent, depending upon the processing conditions. The process includes pressing of the metal powders into green compacts, which are subsequently sintered by heating to a specified temperature (below the melting point of the metal) and pressing them with the help of dies to give desired mechanical properties and bringing down the final porosity up to 1-5% comparable with the density of the wrought metals.

The technique is a convenient way of reducing or eliminating porosity from the traditionally developed powder metallurgy components, which have inherent reduced mechanical and metallurgical properties. Thus, sinter-forging combines the advantages associated with two well-known techniques, namely, (i) Powder metallurgy, and (ii) Conventional forging technology. Powder metallurgy provides sound metallurgical structure to components, as well as, avoids large number of operations, high scrap losses, and high-energy consumption associated with conventional manufacturing process and subsequent, forging provides adequate final mechanical properties like high ductility, tensile, impact and fatigue strength by reducing or eliminating porosity. The mechanical and metallurgical properties of these final sinter-forged products are comparable, in some cases even superior to those of cast, and wrought products.

The literature survey suggests and reveals that many researchers have carried extensive investigation in the area of powder metallurgy, especially during the fabrication of the sintered preforms. Also, lot of studies have been done to investigate the deformation characteristics and their complex interaction with each other including various sinter-forming aspects, but not much work has been reported for the finite element simulation during mechanical working of sintered materials, especially sinter-forging processes. Thus, the present work is important from the view point that it is not only an attempt to simulate the sinter-forging processes, and also an effort to investigate the deformation characteristics and their complex interactions by the finite element approach. The present research also paves the way for formulating basic plasticity rules and constitutive relations for sintered materials, which can be successfully utilized to perform the finite element simulation of different sinter-forging processes.

To simulate the sinter-forging processes, DEFORMTM 2D and 3D finite element method (FEM) based process simulation system was designed to analyze complex two dimensional and three-dimensional sinter-forging processes. The simulation engine was capable of analyzing porous and rigid plastic large strain models based on the updated Lagrangian finite element codes. It includes AMG, an automatic mesh generator that

generates mesh automatically with finer elements in regions, where greater solution accuracy is required, thus reducing the overall problem size and computing requirements. The material model based on the flow curve data was incorporated in the material library. In addition to it, input of detailed process parameters such as interfacial friction coefficients, punch velocity and the dimensions of dies, which is the prime necessity to get the accurate output or simulated results were provided. The interfacial friction conditions was based on the ring compression tests performed using hollow Aluminium metal powder preforms.

The geometry of the die platens were generated in DEFORM software and were modeled as rigid, parallel and flat bodies with preform having porosity approximately 0.8 placed in between them. The geometry of preforms were generated using CATIA V5.0 software using part design module / workbench and data was imported to DEFORM software in form of STL files. The elements used for discretization was an iso-parametric quadrilateral element with bilinear shape function for both two dimensional and axisymmetric deformations respectively. Tetrahedral elements were used for three dimensional deformations. The selected elements were provided the capability of adapting the remeshing functionality. The simulation of the sinter-forging processes was performed, considering the various die or punch velocities with respect to time and number of steps with in the formability limit.

It is expected that the research work presented in the book will be highly useful for the researchers, scientists and practicing engineers in understanding the sinter-forging processes and will assist in carrying further research and development work in the associated field.

CONTENTS

LIST OF FIGURES

LIST OF TABLES

NOMENCLATURE

ρ_o	preform relative density
ρ_i	preform initial density
ρ_{io}	preform initial relative density
C_p	shape complexity factor for hollow preforms
C_f	shape complexity factor for truncated preforms
C_q	shape complexity factor for irregular preforms
r_o	outer radius of hollow preform
r_i	inner radius of hollow preform
r_{to}	larger radius of truncated conical preform
r_{ts}	smaller radius of truncated conical preform
H	height of preform
D	diameter of cylindrical preform
H/D	aspect ratio of preform
a, b, c, d	dimensions of irregular polygonal preform
R_1	upper radius of circles on the irregular preforms
R_2	lower radius of circles on irregular preforms
R	radius of preform used for closed die sinter-forging
R_o	radius of preform used for rotary sinter-forging
D_o	diameter of container used for closed die forging
α	skew angle of upper conical rotary die
ν	Poisson's ratio
U	die velocity
ε_r	strain in radial direction
ε_x	strain in 'x' direction
T	temperature
μ	coefficient of interfacial friction
m	strain rate coefficient
σ_{ij}	stress tensor
$\dot{\sigma}_{ij}$	stress rate tensor
σ_{ij}'	deviator stress tensor
ε_{ij}	strain tensor
$\dot{\epsilon}_{ij}$	strain rate tensor
ϵ'_{ij}	deviatoric strain tensor
σ_o	yield tensile strength of preform
σ_m	hydrostatic stress
ϵ_v	volumetric strain
A, C, k	constants
I_1, I_2, I_3	invariants of deviatoric stresses
δ_{ij}	kronecker delta
E	young's modulus
Y_o	yield Stress in tension
Y_R	apparent yield stress of sintered material

$\dot{\gamma}_{ij}$	engineering shear strain rate tensor
$\dot{\epsilon}_v$	volumetric strain rate
σ_x, σ_y & σ_z	normal stresses
τ_{xy}, τ_{zy} & τ_{xz}	shear stresses
J_1	linear invariant of stress tensor
J_2	quadratic invariant of stress tensor
$\dot{\lambda}$	proportionality factor in flow rule
$\dot{\overline{\epsilon}}_R$	effective strain rate
T	traction force
f	frictional stress
S_i	tool-preform interface
δu	variation of virtual velocities
$\delta\dot{\overline{\epsilon}}$	variation of strain rate
u	displacement
u_r	radial displacement
u_z	z axis displacement
N	shape function
$q_1, q_2, q_3, q_4 \ldots q_\alpha$	displacement at nodes with α number
ξ, ζ, η	natural coordinates
$\dot{\gamma}$	shear strain rate
$\theta_1, \theta_2, \theta_3, \theta_4$	internal angles of on irregular polygonal preform
ω	angular velocity of upper conical rotary die
θ	angular displacement
h_i	indentation height of upper conical rotary die

Subscripts

r	radial
x	axial
θ	circumferential
y	longitudinal
z	vertical

CHAPTER-1
INTRODUCTION

Technological developments, introduction of modern information technologies, communication and transportation technologies, as well as the political choice to consciously open cross border links in international trade and finance are conceived as the main facilitators and driving forces globalization and world economic transformation processes during last few recent years. Innovation and management of technologies, along with factors such as faster design, high product quality, improved productivity, low cost and finally cheaper product to market are some of the factors on which the strategy of competition is based. Globalization in manufacturing industries helped most of the countries to take advantage in such a way that they are now having excellent world class manufacturing hubs for leading multinational companies. The automotive, aerospace, heavy engineering, telecom industries, banking and oil sectors have benefitted most from these reforms.

To sustain the local and foreign competition, any industry has to improve their technologies and technical know-how. One such technology is 'the sintered material technology', an idea that has successfully reached to all general types of industries. It is viewed as a converging and dependable technology, which can provide many solutions to the present-day problems faced by industries of third world countries. Sintered material technology includes methods such as sinter-forging, sinter-rolling, sinter-extrusion, and sinter-drawing. Sinter-forging, which is the subject of study under the present thesis, has gained considerable importance in the recent past. It has evolved as an advanced manufacturing technique for producing high-performance and precise quality engineering components economically in metal working industry, because of its low manufacturing cost compared to conventional metal forming processes.

It uses a pressed and sintered powder metal preforms as starting material, having porosity in order of 15 to 30 percent, depending upon the processing conditions. The process

includes pressing of the metal powders into green compact, shaped into three-dimensional bodies, which are similar to those traditional powder metallurgy parts. The compact is sintered in an endothermic atmosphere by heating at a temperature below the melting point of the metal to give it the desired physical, mechanical, and chemical properties. This is followed by forging of sintered components and bringing down the final porosity up to 1-5 percent which is comparable with the density of the wrought metals [1-2]. Thus, this technique is a convenient way to reduce or eliminate this porosity from the traditionally developed powder metallurgy products, which have inherent reduced mechanical and metallurgical properties.

The present chapter gives a brief overview of operational and techno-economic aspects of sinter-forging technology along with the glimpse of its present status throughout the world. It is clearly demonstrated that one can reap huge benefits, if the technology is properly commercialized. At last, the chapter also presents the current problem along with the major findings and the organization of this present thesis. It is expected that the present chapter will be useful in understanding the fundamentals and applications of sinter-forging technology better.

1.1 SINTER-FORGING TECHNOLOGY - AN OVERVIEW

Sinter forging technology, is a continually and rapidly evolving technology among all manufacturing technologies, for producing components of superior mechanical properties with minimum waste. It combines the benefits associated with two well-known techniques, namely, (i) Powder metallurgy, and (ii) Conventional forging. Powder metallurgy is the process of mixing elemental or alloying fine powdered materials, compacting the mixture, generally performed at room temperature in a die, and heating the resultant shapes in a controlled atmosphere with in furnace to bond the particles metallurgically. Powder metallurgy provides sound metallurgical structure to components, prevents high consumption of energy associated with the conventional manufacturing process, high scrap losses, as well as a large number of operations [3-4], and subsequently, sinter-forging provides adequate final mechanical properties like high ductility, tensile, impact and fatigue strength to traditional powder metallurgy products

by reducing or eliminating porosity. The mechanical and metallurgical properties of these final sinter-forged products are comparable, in some cases even superior to those of cast, and wrought products [5]. Thus, it may be concluded that the present technology presents itself as an alternate route to many conventional manufacturing processes e.g. casting, conventional forging, machining etc.

There are two basic routes for production of sinter-forged components, namely induction heating and furnace heating routes as shown in figure 1.1. The primary difference between these routes is the method of heating green performs prior to sinter-forging operation. During induction heating route, the elemental or alloy metal powder mixed with additives in a mixing chamber is compacted in a closed compaction dies to form green compacts/preforms. Green preforms are sintered and cooled to room temperature and then again heated and sprayed with a protective graphite coating. The coating provides protection against oxidation, as well as acts as lubricant. These coated preforms are then heated within an induction heating system under a protective atmosphere to the required forging temperatures and finally forged on a mechanical press to get the finished product. During furnace heating route, green preforms are sprayed with protective coating prior to sintering, which are cooled to the required forging temperatures after sintering and finally forged directly out of sintering furnace. The toolings are sprayed with water-based lubricant for cooling action and lubrication. The induction-heating route is preferred for sinter-forging of symmetrical shaped components, *e.g.* bushings and stator clutch races for automatic transmissions, because of its automatic fast-feeding ability. On the other hand, furnace-heating route is more versatile, provides better temperature control and protection of parts in a controlled atmosphere, and is preferred for the production of non-symmetrical components. The recent trend in sinter-forging procedure is to omit the sintering step, where the green preforms heated to forging temperatures and forged immediately within the closed dies [6].

Figure 1.2 shows the sinter-forging process of connecting rod. It demonstrates that initially the metal powder is taken loose and then compacted in closed dies to form metal preforms. Finally, these preforms are forged to the required shape and size, at either room or elevated temperature and desired components are manufactured [7]

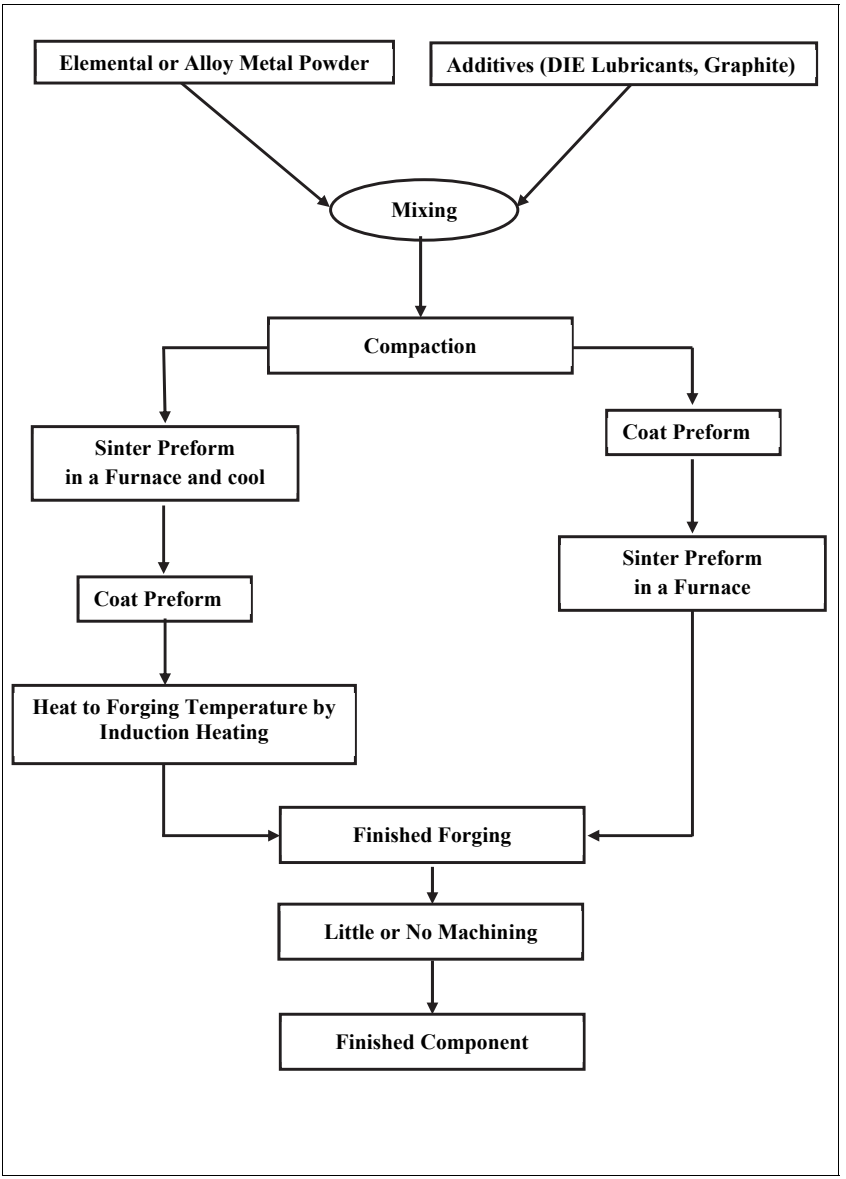

Figure 1.1: Flow Diagram of Sinter-Forging Process.

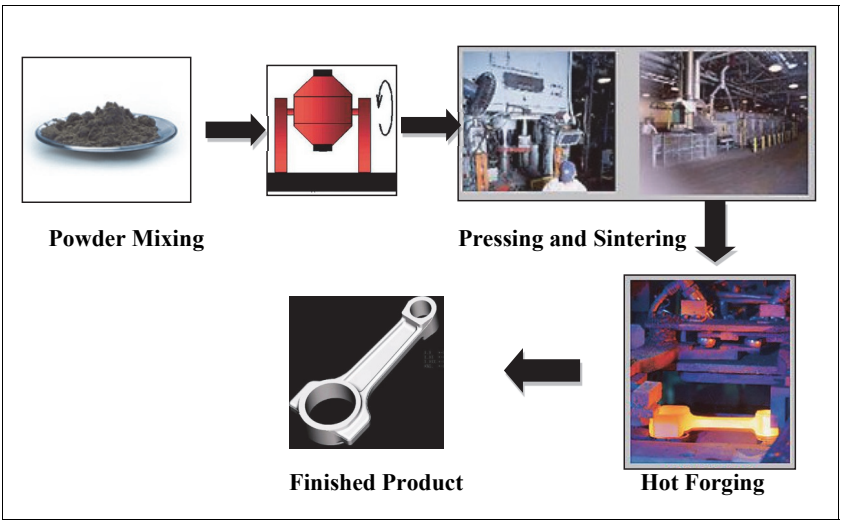

Figure 1.2: Sinter-Forging of Connecting Rod [7].

1.2 TECHNO-ECONOMIC ASPECTS AND INDUSTRIAL APPLICATIONS - SOME GLIMPSES

Sinter-forging technology, during the past few decades has gained strategic importance due to capability of producing near-net-shape components with close tolerances and greater homogeneity with regard to composition, finer microstructure, and absence of internal discontinuities. It allows manufacturers to produce products that are more consistent and predictable in their behavior in a wide range of applications. Additionally, the process has a high degree of flexibility, allowing the adaptation of the physical characteristics of the product to meet the specific properties and performance requirements [8-9]. In addition to distinct technical advantages, it also has product cost-effectiveness in comparison with other production technologies. It has the highest raw material utilization, over 95 percent in the finished parts and is suited to high- volume production requirements generally without the machining operation. Lowest energy requirement per kg of finished part alone contribute significantly to the economic

advantage and offered by the sinter-forging processes. The reduction in the number of forging steps, die manufacturing and operational cost, along with the simplicity in process has led to the better and rapid realization by most of the industries engaged in the mechanical processing of materials [10-11].

In past, the reason for choosing this route was only economical, but more recently the process has come to be recognized as an environmentally attractive process from the viewpoint of energy conservation, cleanliness and recycling. Table 1.1 shows the raw material utilization and energy requirements of various manufacturing processes with respect to sinter-forging technology as per data [12].

Table 1.1. Raw Material Utilization & Energy Requirements of Various Manufacturing Processes [12].

Sl. No.	Manufacturing Process	Raw Material Utilization (%)	Energy Requirement per Kg of Finished Part (MJ)
1	Casting	90	30-38
2	Sintering	95	29
3	Cold or Warm Extrusion	85	41
4	Hot Drop Forging	75-80	46-49
5	Machining Process	40-50	66-82

Improved cost performance ratios of the components, together with lower wastes, closer tolerances, unique properties, high reliability, use of special materials, improved design capabilities, high quality, increased performance, ability for mass production of engineering components has prompted many manufacturers to switch production to sinter-forging technology. In most industrial countries, 70-85% of finished sinter-forged components are for the automotive industry. This technology enjoys the benefits of enhanced content in light vehicles. Automotive design engineers have been converting forgings, castings, and stampings, when designing new engines and transmissions into powder forgings. Typical Sinter- forged components such as connecting rods, main bearing caps, planetary carriers, chain sprockets, and parking gears etc. are usually in modern engines and transmissions systems [13].

It was cited that now-a-days, new engines and six-speed transmissions use significant amounts of sinter-forged metal components. GM and Ford models with six-speed contains 28 to 34 pounds of sinter-forged parts per vehicle. In general, the average U.S. made vehicles in 2010 was estimated to contain 41.6 pounds of sinter-forged parts, with a slight gain of nearly 42 pounds forecast for 2011. In Europe, the average sinter-forged part consumption per vehicle in 2010 was estimated at 18.5 pounds. The 2011 Ford Edge with a 3.7-liter engine is a prime example of a heavy sinter-forged component user; with an estimated 66 pounds, which is broken down as follows: engine-26 pounds, transmission-26 pounds, transfer case-8 pounds, and suspension system-6 pounds. It is expected that new programs in the pipeline in automotive sector will add even more sinter-forged metal parts.

Sinter-forged parts consumption among North American OEMs is way up. GM is up more than 32 percent, Toyota are up 14 percent, and Nissan is up about 12 percent. Hyundai SUVs contain up to 41 pounds of sinter-forged parts, although most are made in Korea. Honda SUVs average more than 42 pounds of sinter-forged parts The 3.5 litre engine model was recently cited as having sinter-forged connecting rods, park-lock guide, and transmission clutch plates made by three leading domestic sinter-forged parts fabricators [14]. This interest is gradually extended to variety of steels, ferrous, non-ferrous metals and alloy powders like brass, aluminum, bronze, super alloys etc. [15-16]. In 2010, ferrous powders accounted for 62 percent of the total sinter-forged market by volume, and demand in 2015 is projected to reach 917 million pounds. These powders are iron, steel, and stainless steel, and are used in different applications, such as automotive components, machinery parts, chemical additives etc. The nonferrous powders, which include a much wider range of base metals such as aluminum, tungsten, gold, silver etc. is estimated to reach demand of 539 million pounds in 2015 [17].

The development in Asia-Oceania region is also not far away. The maturation of automotive market in India due to advent of number of world-class automobile manufacturers in last decade has led to strong growth of sinter-forged industry. India is now the seventh largest manufacturer of motor vehicle or car in the world and is expected to rise to fourth position by 2014. A four-wheeler made in India uses 5 – 6 kg sinter-

forged parts, while two or three wheelers use 150 kg per vehicle. As Indian automobile market share is 60% of sinter-forging market, this would mean 13,640 tons and 1,472 tons of sinter-forged parts usage in four wheelers and two or three wheelers respectively yielding a total sinter-forged parts market of 15,112 tons in motor vehicles and 6,045 tons in domestic appliances [18].

Materials in the form of sintered preforms delivered not only better physical, chemical and thermal properties, but also made new applications possible. One such pioneering application of sintered material is production of cemented carbide tools, which revolutionized the machining industry. Like other areas of materials industries, powder metallurgy (P/M) is facing unprecedented challenges in the highly competitive international market. Rising energy and raw materials costs, the challenge of customers demanding closer tolerances, which require additional sizing operations, wounded OEM automakers and customers rushing to Asia with manufacturing assembly plants are changing the way powder metallurgy companies operates. While growth in North America and Western Europe can be aligned, Asia seems to be brighter than ever before, especially in China and India [19-21].

Figure 1.3: Illustration of Sinter Forged Components [11].

1.3 FINITE ELEMENT SIMULATION - A BRIEF

Since the advent of computing technology, various general purpose computational techniques has been evolved in the recent past years to assist and support solutions for complex design and manufacturing problems. The application of finite element method for the investigation of metal forming processes allows analysis and optimization of the processes, and is increasingly used in the forming industry to support the design and development process. With the expansion of computing power, the use of three-dimensional simulations emerged to provide realistic results, and enabling accurate and detailed information in analyzing the metal forming processes. In building toward this goal, various simulations types were evaluated and several solutions to sinter-forging problems been reported. Practical application of this method focuses on the modeling and simulation of material flow, investigation of die fill, elimination of forging defects, achieving the desired grain flow and product properties, assessing and predicting the influence of process parameters and stress analysis in dies. In addition to this, computer simulation also reduces expensive shop floor trials, leading to shorter process development time, faster time to market and increased profitability [22-23].

During the present research work, the entire finite element simulations were performed using DEFORM™ software and investigations into various deformation characteristics during various categories of the sinter-forging processes, been done using the above application software. DEFORM™ 2D and 3D finite element method (FEM) based process simulation system is designed to analyze the complex two dimensional and three dimensional metal forming processes. The simulation engine was capable of analyzing porous and rigid plastic large strain model, based on the updated incremental Lagrangian finite element codes. It includes AMG, an automatic mesh generator that generates mesh automatically with finer elements in the regions that require high accuracy solution, thereby reducing the overall size of the problem and the computational requirements [24].

1.4 OBJECTIVE OF THE PRESENT RESEARCH WORK & THESIS ORGANIZATION

The literature survey suggests and reveals that many researchers have carried extensive investigation in the area of powder metallurgy, especially during the fabrication of the sintered preforms. Also, lot of studies have been done to investigate the deformation characteristics and their complex interaction with each other including various sinter-forming aspects, but not much work has been reported for the finite element simulation during mechanical working of sintered materials, especially sinter-forging processes. Thus, the present work is important from the view point that it is not only an attempt to simulate the sinter-forging processes, and also an effort to investigate the deformation characteristics and their complex interactions by the finite element approach. The present research also paves the way for formulating the basic plasticity rules and constitutive relations for the sintered materials, which can be successfully used for performing the finite element simulation of different sinter-forging processes.

The present research work utilizes sintered Aluminium metal powders to fabricate the sinter-forged components and the reasons for the selection of the Aluminium metal was due to its inherent advantages of higher strength-to-weight ratio, improved energy effectiveness and high compressibility at lower compaction loads. This unique property of compaction of Aluminium metal powders, where 90-95 percent of theoretical density can be achieved only at 11-20tonf of compaction load, enabling the material to deliver high yield density components along with the requirements of smaller, faster and cheaper presses were also the chief reasons for its selection. Sintering temperatures for Aluminum metal powder being much lower, i.e. 300° to 500°C, as compared to other ferrous metal powders leads to significant energy savings in the manufacturing of sinter-forged components. The present research work being a pilot research study at laboratory scale, the selection and use of the Aluminium metal powder for the analysis of various sinter-forging processes was thus fully justified.

The present research work was meticulously planned with three different problems based on the general categories of forging technology, e.g. open-die sinter-forging, closed-die sinter-forging and rotary sinter-forging processes. Further, three different cases under

open-die sinter-forging were considered, based on the different generic shapes of the preforms, i.e. hollow, truncated conical and irregular trapezoidal preforms. The idea was to envelope various types of generic shapes, which can be added or subtracted during solid modeling to create any complex shaped component. The closed-die forging problem was formulated on the flashless concept, where deforming preform was completely enclosed within the closed die-set to form a double-hub flange component. The rotary sinter-forging problem investigates in detail the rotary forging of sintered Aluminium cylindrical preforms using conical dies.

In order to carry out the finite element analysis of all the three categories of the sinter-forging processes as mentioned above, it was necessary to carry out initial basic experimental work, which included fabrication of Aluminium metal powder preforms and subsequent forging of these preforms to analyze various deformation characteristics related to sinter-forging. The data recorded was utilized to generate few useful information, e.g. stress-strain variations, related flow curve, interfacial frictional conditions, and formability analysis (crack-free deformation), which was utilized to formulate the plasticity laws and governing equations for finite element analyses of various sinter-forging problems undertaken in the present research work. Firstly, the Aluminum metal powder compacts were prepared by compacting the pure Aluminum powders within the closed circular cavity powder compaction die-sets and sintering them at required temperatures. The compacts having different aspect ratios (l/d ratios) and shapes were prepared with different compaction pressure, compaction time, sintering temperature and sintering time. Finally, these compacts were forged under open-die condition at room temperature and various related deformation characteristics were measured.

To simulate the sinter-forging processes, DEFORM^{TM} 2D and 3D finite element method based process simulation system was used. The material model based on the flow curve data was incorporated in the material library. In addition to it, input of detailed process parameters, such as, the dimensions of dies, interfacial friction coefficients and punch velocity, which is the prime necessity to get the accurate output for simulated results were provided. The interfacial friction conditions and selection of the corresponding

friction factors during the analysis of various categories of sinter-forging processes under consideration in the present research work was based on the ring compression tests performed using hollow Aluminium metal powder preforms. The data for the change in outer and inner radii of hollow preform during deformation were recorded and friction factors were numerically computed.

The geometry of the die platens were generated in DEFORM software and were modeled as rigid, parallel and flat bodies with preform having porosity approximately 0.8 placed in between them. The geometry of preforms were generated using CATIA V5.0 software using part design module / workbench and data was imported to DEFORM software in form of STL files. The elements used for discretization was an isoparametric quadrilateral element with bilinear shape function for both two dimensional and axisymmetric deformations respectively. Tetrahedral elements were used for three dimensional deformations. The selected elements provided the capability of adapting the remeshing functionality. The simulation of the sinter-forging processes was performed, considering the various die or punch velocities with respect to time and number of steps with in the formability limit.

The present research work compiled in form of thesis, has been organized into following chapters:

- **Chapter 1: Introduction**
- **Chapter 2: Literature Survey**
- **Chapter 3: Basic Experimental Work**
- **Chapter 4: Plasticity Model & Finite Element Formulation for Sintered Materials**
- **Chapter 5: FEM Analysis of Open-Die Sinter-Forging of different Generic Shaped Preforms**
- **Chapter 6: FEM Analysis of Closed-Die Sinter-Forging of Double-Hub Flange Preforms**
- **Chapter 7: FEM Analysis of Rotary Sinter-Forging of Cylindrical Preforms**
- **Chapter 8: Conclusions & Scope for Future Work**

Chapter 1 introduces about sinter-forging technology and highlights its advantages over the conventional manufacturing processes. It presents the techno-economic advantages of sinter-forging technology and gives a glimpse of its present status along with the possible applications throughout the world. It also presents the implementation of FEA in the area of metal forming. At the end of the chapter, a brief report regarding the present research work along with the problem definition and organization of the present thesis are presented.

Chapter 2 presents the literature review with respect to research carried in the field of powder metallurgy, sinter-forming technology (especially sinter-forging process), and finite element simulation process in the metal forming area. The literatures related to production of metal powders, metal powder compacts and sintered components, which include processes like mixing and blending, compaction under pressure causing the bulk movement and deformation of the individual particles, their densification behavior, various sintering procedures, effect of various lubricants, temperature and other alloying elements, yielding of porous materials, plasticity theories, etc been presented and discussed. The literatures related to design and optimization of various preform shapes for improved dimensional accuracy of final sintered components, closed-die forging of wrought materials with and without flash has been discussed and presented. A brief survey of rotary-forging of wrought materials from various technical aspects has also been given. The research related to effect of die speed on various deformation characteristics during mechanical processing of sintered materials been also discussed. At the end, research survey of the papers related to the effect of process variables on deformation behavior of sintered materials using finite element methods been presented.

Chapter 3 reports on basic experimental work required to investigate the fundamental deformation characteristics and their complex interaction during forging of sintered materials. Considering the three categories of the forging processes in the present research work, the basic experimental work related to open-die, closed-die and rotary sinter-forging processes has been presented in this chapter. This basic experimental work for mechanical processing of sintered materials serves as the starting point for the formulation of plasticity rules and constitutive relations required to carry out the

necessary finite element simulations. The complete experimental work is segmented into three major parts, i.e. fabrication of forging dies, fabrication of Aluminium metal powder preforms with required dimensions under various process conditions and performing sinter-forging experiments along with the measurements of various important deformation characteristics. The complete details of the production of forging dies involving fabrication of closed-cavity powder compaction dies for the compaction of Aluminium metal powder, die-sets for flashless closed-die sinter-forging, and rotary forging upper conical tool for performing rotary sinter-forging process has been presented. The process details during fabrication of metal powder preforms along with the characterization of the Aluminium metal powder used during experimentation and associated process characteristics has been presented. The details of all the Aluminium metal powder preforms with different generic shapes, e.g. hollow disc, truncated conical, irregular trapezoidal and cylindrical preforms is also presented in the present chapter. The details of the ring-compression tests, forgeability tests along with the measurement of various deformation characteristics during open-die, closed-die and rotary sinter-forging processes of Aluminium sintered preforms has been presented in the form of graphs.

Chapter 4 discusses in detail the vital characteristics of plastic deformation model of the sintered materials. In characterizing the mechanical response of porous materials, a suitable yield function / criterion, that affects not only the deviatoric component of stress but also sensitive to hydrostatic stress component was proposed. It was shown that homogeneous and isotropic porous materials begin to yield only, when the apparent total distortion energy reaches a critical value. Up to yield point, as there is no appreciable change in the density and the behavior of the porous material being linear; it was shown that the densification begins upon yielding. Being the behavior to be linear up to the yield point, the Von-Mises yield criterion was extended for the sintered porous materials, assuming that the yielding occurs when the distortion energy reaches a threshold value. The finite element formulations to be applied for the present problems of sinter-forging under consideration in the present research work was also presented. The finite elements used for the preform discretization (axisymmetric isoparametric quadrilateral element with bilinear shape function for all two-dimensional deformations, and four-node

tetrahedral elements having remeshing capabilities for three dimensional deformations) were critically analyzed and justified for the present research work.

Chapter 5 presents the finite element analysis of open-die sinter-forging of different generic shaped preforms, and has been divided into three sections; namely, finite element analysis of sinter-forging of hollow preforms, finite element analysis of sinter-forging of truncated conical preforms and, finite element analysis of sinter-forging of irregular trapezoidal preforms. The finite element simulation and parametric discussions of all the above-mentioned sinter-forging processes have been presented along with the general assumptions. Four major assumptions made during the present analyses are that the circumferential flow or rotation of preforms, , the normality of plastic strain rates to the yield surface which holds anisotropy that occurs during deformation, the elastic portion of deformation and the thermal properties of porous materials were neglected and assumed to be negligible. Additionally, during the sinter-forging of truncated conical preforms, deformation was assumed to be concentrated at smaller end of preform and radial flow of large diametric end of preform was considered almost negligible. For irregular trapezoidal preform, the additional assumption was that velocity discontinuities or jumps along common boundaries of various regions of velocity field within the deforming irregular trapezoidal preform were considered to be negligible based on the basic experimental analysis. The preform shape variations on different characteristics been studied by introducing shape-complexity factors, which were defined mathematically. In case of hollow preforms it is the ratio of outer radius to inner radius, for truncated conical preforms it is expressed as the ratio of larger to smaller radius of preform and in case of irregular trapezoidal preforms it is defined as the ratio of the radius of the inscribing circles from the intersection of angle bisectors of preform corners. The influence of die velocity, internal energy dissipations, die loads, final bulged shape of preforms, strains at preform free surfaces, respective strain rates and their interrelationships along with the distributions of effective strain, stress, total deformation, and velocity vector, have been critically investigated and displayed graphically. The variation of effective stress, strain, internal energy dissipation, forging load with forging time were also studied and suitable plotted.

Chapter 6 deals with finite element analysis of closed-die sinter-forging of cylindrical preforms into double-hub flange components. In general, closed-die forging process tends to be an extremely complex process with respect to independent variables (like workpiece geometry, material characteristics, tool and die geometry, and amount of deformation), dependent variables and also both independent and dependent interrelationship variables. The most useful need for the designer is to predict and estimate the maximum stress distribution on the dies, the maximum load required by the equipment and the total energy necessary to complete deformation, further enabling to calculate strains and stresses on the dies during the closed-die forging process. The present analysis of closed-die sinter-forging of cylindrical preforms was performed by centrally locating the cylindrical preforms respect to the central axis of the closed die-sets. The process comprises of moving upper and stationary lower counter punches housed in a die-container considering the circumferential flow or rotation of preforms being negligible. The complete deformation takes place in two subsequent stages. The first stage consists of the bulging of free vertical side of the cylindrical preform, till it reaches and touches the die-container sidewalls and the second stage consists of constrained deformation of bulged preform, where die-corners are formed and filled. The die load has been computed at the end of sinter-forging process, when die cavity is just about to be filled completely, as it is assumed that the forging load shall be maximum at that point of time. The objective of this chapter was to investigate and simulate the effect of die velocity, and preform aspect ratio on internal energy dissipations, die cavity fills and die loads. The variation of effective strain, stress, strain rate, forging load and internal energy dissipation with forging time were investigated. The distribution of total displacement, effective stress, strain and velocity vector in form of color codes and contours on the preform surface were obtained. To investigate these distributions over the preform profile, slicing was done and the results were again plotted. The validation of the simulation was done by comparing results with the experimental results, which were found to reasonably agree with each other, which indicated that finite element simulation represents fairly well with the present sinter-forging process.

Chapter 7 deals with finite element analysis of rotary sinter-forging of cylindrical preforms. The analysis of rotary sinter-forging process is considered to be complex, as it

introduces both the combinational effect of rolling and pressing action between fixed flat bottom die and rotating or swiveling upper die with an inclined conical working face. The finite element simulation of rotary sinter-forging of Aluminium preforms was performed using Deform ^{TM} -3D software, which is based on the updated Lagrangian finite element code. The rotary dies were modeled as rigid bodies with required dimensions using CATIA software (as *.CATPART files) and later imported as STL files. The geometry of the cylindrical preforms with required dimensions were modeled in the Deform software. As there is a possibility that during rotation of upper conical die, the cylindrical workpiece may struck and rotate together with it, a constraint was exerted between bottom surface of preform and top surface of lower die considering it to be a sticking zone. There are two contact pairs; one between the conical surface of upper die and the upper end surface of the cylindrical preform and the other between the upper surface of the lower die and lower surface of preform. The two contact pairs were inter connected allowing to have a relative sliding motion of two surfaces, contributing to describe the interfacial friction conditions of the contact pairs with coulomb friction model. The effective coefficient of interfacial friction considered was 0.3 and 0.05. The cylindrical preforms were considered as a 3D deformable porous body with initial density of 0.8 and the entire body was discretized with numbers of tetrahedral elements. Finer meshes were generated close to the face edges in order to better scope the forging process. The complete simulation was performed in 10 steps having stroke movement of the die platens in each step equal to 0.25 mm. The variation of effective strain, stress, strain rate, forging load and internal energy dissipation with sinter-forging time were analyzed and plotted. The distribution of effective stress, strain and velocity vector in form of color codes and contours on the preform surface were obtained and suitable plotted.

Chapter 8 summarizes the total research work in form of important conclusions related to the finite element simulation of open-die, closed-die and rotary sinter-forging processes considered under the present research work followed by the scope for the future work.

It is expected that the present research work will be extremely helpful in understanding the complex deformation characteristics involved during sinter-forging processes, using finite element technique. It is also anticipated that the research work will be highly useful for the scientists and practicing engineers during design and fabrication of the tools and equipments required for the sinter-forging operations.

CHAPTER 2
LITERATURE SURVEY

Over the past few years, metal powder components occupied an important position in industry, as they have been used successfully in a wide range of applications. Metal powder products manufactured by sinter-forging technology are comparable in terms of both mechanical and metallurgical properties and even in some cases superior to cast and wrought products. This has made large number of research workers to get attracted to the field and work in the area of mechanical processing of sintered materials. Literature survey has indicated that a lot of work has been reported on the production of metal powders and metal compacts, which include processes like mixing and blending, compacting under pressure causing the bulk movement and deformation of individual particles, and sintering *Hirschhorn* [25]. Investigations in studying the deformation and densification behavior of sintered Preforms under cold axial deformation, in order to understand the influence of various parameters such as effect of die speed, compaction pressure, green density, green strength and hardness of metal powder compacts was also reported by various researchers.

Morgan et. al. [26], *Alexander et. al.* [27], *Shima et. al.* [28], *Fischmeister* [29], *Stein et. al.* [30], *Wang and Davies* [31], *Elwakil and Davies* [32], *Vitvaz and Roman* [33] and *Kumar et. al.* [34] have studied the isostatic metal powder compaction method, in which pressure is applied by sealing the powder in a flexible envelope and immersing the assembly in a fluid that can be pressurized. Variation of process developed and investigated the effect of different modes of applications of pressures, absence of tool/powder friction, green density, green strength and hardness of metal powder compacts.

Wang et. al. [35], *Biner and Spitzig* [36] and *Kim* [37] have evaluated the effects of hydrostatic pressures on densification mechanism and density distribution during powder compaction process. A reason was proposed for the behavior observed and a modified

model was introduced taking internal pressure effects in account, and exhibited with an excellent agreement with the experimental observations.

Jha [38] as stated in porous metals density does not remain constant and changes with deformation. The compressive force, which is directly proportional to the real contact area, gradually increases the real density to apparent relative density. Also, the density distribution did not appeared uniform throughout, and was high in the central region and low at the edges. The density distribution was more uniform for small coefficient of friction for higher initial density.

Chandramouli et. al., [39] who studied the effect of material flow constraints during cold forming on the deformation and densification behavior of hypo eutectoid powder metallurgy ring preforms, and stated the deformation behavior during metal powders compression is entirely different from the compression of wrought metals, as it is characterized by change in volume due to change in porosity of the compact. A sintered preform with high relative density (pores of small size and number) yields at relatively high stress, whereas a low relative density preform (pores of large size and number) yields at relatively low stress.

Zape [40], *Ward and Biullington* [41], *Lindskog* [42], *Kao and Koczak* [43], *Hwang and Kobayashi* [44] and *Brakpool* [45] have studied critically the deformation characterization of metal powders and effect of addition of various additives like lubricants and other alloying metals during powder metal compaction process.

Hamiuddin and Upadhyaya [46, 47], *Borland et. al.* [48] and *Tengzelius and Blande* [49] have studied the sintering procedures and effect of temperature and alloying metals on final density, strength and hardness of the metal powder compacts.

A lot of researchers have developed plasticity theory and yield criterion for porous solids and reported their investigations about the governing compatibility conditions during metal powder compression process. *Green* [50], *Downey and Kuhn* [51], *Elwakil* [52], *Shima and Oyane* [53] and *Lewis and Khoei* [54] have carried extensive investigations during compression of metal powders and established the plasticity upper-bound and

slip-line field theories for sintered powder materials. It was found that yielding of sintered materials is sensitive to hydrostatic stresses component imposed, as yield surface closes on the hydrostatic stress axis.

Tabata and Masaki [55], *Thomas* [56], *Kim* [57], *Lee and Kim* [58], *Akisanya et. al.* [59], *Griffiths et. al.* [60] and *Justinoet. et. al.* [61] studied the plastic yield behavior of porous metals and proposed the principal strain increments, volumetric strain increments and corresponding yield criterion for powder metallurgy materials. The compatibility conditions were studied critically and various constitutive models for plastic analysis of porous sintered materials were established.

These established plasticity theories, yield criterions and compatibility conditions been used and investigated by lot of researchers to analyze theoretically and predict the pressure distribution, deformation load, strain rates, bulged profiles, final density and energy dissipations during problems related to mechanical processing of sintered materials. *Nakagawa et. al.* [62], *Huppmann* [63] and *Standring et. al.* [64] studied the deformation characteristics, *e.g.* forging load, metal flow and magnitude of strains involved during cold sinter-forging of sintered metal powder preforms with different generic shapes both theoretically and experimentally. *Tabata, Masaki and Hosokawa* [65-66] estimated experimentally the measure of coefficient of interfacial friction during sinter-forging and flow stress of porous sintered preforms. *Kim et. al.* [67-69] and *DeSilva and Ramesh* [70] carried out the investigations into rate-dependent deformation behavior and strain hardening responses of sintered porous materials under various stress conditions. *Difai* [71], *Forguson et. al.* [72], *Suh and Kuhn* [73], *Tiwari et. al.* [74], *Chitkara and Liaghat* [75] studied the forgeability, fatigue, fracture and deformation modes of metal powder preform during sinter-forging process and suggested possible preventive criterion. *Marx et. al.* [76], *Fischmeister et. al.* [77], *Cook* [78], *Im and Kobayashi* [79], *Wang and Zaidi* [80-81] investigated the effect of temperature on various deformation characteristics during hot sinter-forging process. *Rahman et. al.* [82] and *Huang et. al.* [83] studied the effect of relative density on the forming limits of PM compacts in upsetting under different operation conditions including the billets aspect ratio (height to diameter ratio), frictional conditions and void volume fraction during

deformation. A workability factor was considered, which described the effectiveness of mean stress, and was used as a function of the relative compact density. They reported that the forming limit strain during upsetting of P/M compacts depends on its relative density.

Narayanasamy, Ramesh and *Pandey et. al.* [84] reported some aspects of workability studies in cold forging of pure aluminium powder metallurgy compacts, a detailed discussion on workability factor of aluminium powder metallurgy compacts with respect to the combined effect of the mean stress and the effective stress was described and compared for the cases of uniaxial upsetting, plane stress upsetting and triaxial stress state of upsetting.

Pokorska [85] studied the deformation of powder metallurgy materials in cold and hot forming and presented the theory of deformation of powder metallurgy materials. This information derived was used for subsequent quantitative design, as well as, for optimization of the powder metallurgy process in hot forming.

Sutradhar et. al. [86-87] investigated into various aspects of cold forging of iron powder preforms (solid & hollow), which were compacted and sintered from atomized iron powder. An upper bound solution was constructed for determining the die pressures developed during the cold forging of iron powder under axi-symmetric and plane-strain condition. They reported that the sinter-forging of metal powder preforms creates a lot of interest around the world, as one of the most economical method of manufacturing technology and the process is becoming more popular because of its simplicity and flexibility.

A considerable research work including both theoretical and experimental analysis of closed-die forging of wrought materials have also been carried by researchers. *Ibhadode* and *Dean* [88] investigated the influence of process parameters on load and accuracy during forging in a closed die, effect of billet location on completely closed cavity die forging, corner filling characteristics in precision forging, and demonstrated that the inaccuracies in billet location significantly affect the forging load requirements and dimensional accuracy and die cavity filling. Also, the velocity field which leads to a

better prediction of the load is not that, which closely describes the changes in the billet geometry.

Kwan [89] analyzed the closed die forging of a general non-axisymmetric shape by upper bound elemental method, and compared the proposed velocity field with theory and experimental results.

Altan and Fiorentino [90], *Singh et. al.* [91] investigated the flow behavior of powder preforms during corner filling of the closed dies. The double hub flange component was fabricated using cylindrical Aluminium powder preforms as initial material and the analyses was performed based on the Upper Bound approach. Two different types of the deformation modes were considered and the results were compared.

Altan and Henning [92] and Shen *et. al.* [93] analyzed the flash dimension, billet size and material savings during closed-die forging process of round-shape bars. *O'Connell et. al.* [94], *Takemasu et. al.* [95], *Lee et. al.* [96], Akgerman *et. al.* [97] and Kim and Chitkara [98] investigated the metal flow and preform optimization, *i.e.* optimal preform shape and design for improved dimensional accuracy of final forged components during flashless closed-die forging.

Though sinter-forging technique being a prominent and appreciable one in metal forming industries, With increase in competition in market to have cost effective with high accuracy, good surface finish rotary forging on sintered metal preforms had become one of the most important forming processes. This process is advantageous because of the load requirement to carry out the deformation which is very low due to having relatively small area of instantaneous contact surface. Thisalso leads to high tooling life and requirement of low capacity presses resulting into reduced initial investment and maintenance cost. *Stranding P.M.* and *Appleton E* [99] confirmed through his investigation that the sinter rotary forged components find applications in various industrial and commercial fields, e.g. high power semiconductor, automotive, agriculture, sports, industrial automation, oil & gas etc. but the tilt angle between the two dies plays a major role in determining the amount of forging force that is applied to the workpiece. A larger tilt angle causes greater frame deflection within the forge, making it

difficult to maintain a consistently high level of precision. *Kubo* and *Hirai* [100], *Zhang* [101], *Jeswiet et. al.* [102] investigated in calculating the force and energy requirements during rotary-forging, and concluded by limiting the area of contact of the upper die and workpiece to a small portion of the whole surface, the advantage of load reduction offered during rotary forging as compared with the conventional forging has been to between 10:1 and 30:1. That is why this process recieves considerable attention worldwide.

Hayama [103], *Kobayashi* [104] and *Marciniak* [105] carried out investigation into sinter-forging of components using rotary-forging press and reported experimental and theoretical research work on warm and cold rotary-forging of axi-symmetric and thin components. *Choi et. al.* [106] proposed a simple velocity field at given velocity boundary conditions, during rotary forging process. Upper-bound force was determined and velocity distribution was investigated by minimizing the total power consumption choosing some selected parameters.

Finite element simulations of metal powder compaction and sintering are at the top of the powder metallurgy industry's wish list. There are many anticipated advantages in such efforts, as the implementation of three-dimensional simulations provide realistic outputs. Recently, these simulations have provided valuable three-dimensional procedure to predict the final size and shape of the components after sintering. As the pressed green body is not homogeneous, backward solutions are needed to select the powder, compaction, and sintering attributes to provide the target properties with different tool designs, compaction presses, and sintering furnaces. In building toward this goal, various simulation types and solutions for sinter-forging problems were evaluated and reported. *Hwang and Kobayashi* [107] applied finite element method to analyze the compaction pressures involved during powder metal compaction process.

Im. and *Kobayashi* [108-110] and *Ranek et. al.* [111] applied finite element method technique to simulate and analyze the plastic deformation behavior and densification of metal powder preforms during sinter-forging process. In addition, a considerable amount of research work has been reported on various technological aspects of sintered preforms during sinter-rolling and sinter-extrusion processes. *Fereshteh* and *Jaafari* [112] have made a comparison between analytical, experimental and finite element simulation

results obtained during close-die forging of two axi-symmetrical components. Two sets of results were compared, and found in some cases, the slab methods predictions are as reliable as the FE results, even if the previous methods involve more simplifications and unable to consider much detail about the process. The computational time and the software and hardware requirements for the slab method are considerably less than the FE method. *Altan* [113] and *Majerus et. al.* [114] carried the computer simulation of precision axi-symmetric closed-die forging process to predict the load, stress and metal flow and compared the results experimentally also. *Jolgaf et. al.* [115] developed a CAD/CAM system for the closed-die forging process.

Kwan [116] applied concave circular parallelepiped elements to model and analyze the three-dimensional closed-die forging process having a concave curved surface. Its application capability been demonstrated by doing forging experiments on commercially pure lead billets at ambient temperature. Theoretical forging load predictions correlated well with the experimental results, and found to increase with decreasing flash height.

Literature survey has also indicated lot of work that has been reported on rotary forging process using finite element analysis method. *Guangchun et. al.* [117] proposed methods to deal with certain problems in analyzing rotary forging with the finite element method and initial application to a ring workpiece.

Jang and *Liou* [118] had studied the stresses developed in axi-symmetric products processed by radial forging using a 3-D non-linear finite-element method. In order to study the formation of residual stress due to radial forging, a three-dimensional theoretical model was developed using a non-linear finite-element method program. The workpiece used in the calculations was alloy steel MILS 11595 and was assumed to have elasto-plastic behavior during forging. The coulomb friction law was applied to simulate the contact behavior between the workpiece and the mandrel and between the workpiece and the die.

Wang and *Guoqun* [119] performed a three-dimensional rigid plastic FEM analysis of rotary forging deformation of a ring workpiece. Velocity fields and stress strain fields of the ring workpiece in the rotary forging deformation are obtained. *Yuan, Wang, Liu* and

Cho [120] analyzed and performed the precision forming of pin parts by cold-drawing and rotary-forging using the finite-element method. The determination of the drawing loads and the rotary forging loads, and the deformation mechanism and product quality are discussed.

Liu et. al. [121] gave the insight explanation to the mushroom effect during rotary-forging of cylindrical components. A cylindrical billet is likely to be formed in a mushroom-shape after rotary forging, but not as drum shape in upsetting. *Ameli* and *Movahhedy* [122] presented the parametric study on residual stresses and forging load in cold radial forging process. In this work, a comprehensive study of radial forging process was presented through 2-D axi symmetric and 3-D finite element simulations while considering internal tube profile. The tube used in this investigation has four internal helical grooves along its length. The material was modeled with the elastic-plastic behavior, and friction model at the die workpiece and mandrel-workpiece contacts. The numerical results in the 2-D case are compared with available experimental data. Residual stresses, stress concentration around the grooves, pressure distribution on the hammers and mandrel and maximum forging load in the forged product are critically studied.

Hua and *Han* [123-124] carried three dimensional finite element modeling simulation of cold rotary forging of a cylinder workpiece. The reliability of the proposed 3D FE model was verified experimentally. Through simulation, the distributions and histories of different field-variables such as stress, strain and force and power parameters are investigated in detail. The research results provide valuable guidelines for better understanding the deformation characteristics of cold rotary forging of the ring workpiece.

Deng et. al. [125] presented the finite element analysis and experimental investigation of cold rotary forging of a 20CrMnTi alloy spur bevel gear. 3D rigid-plastic finite element (FE) model of cold rotary forging of a 20CrMnTi alloy spur bevel gear was developed under the DEFORM-3D platform. To ensure the validity of the proposed finite element model, a series of experiments performed to identify the mechanical properties of

20CrMnTialloy and the realistic friction conditions prevailing at the die-workpiece interface. By utilizing this FE model, the workpiece geometry is optimized with the intention of achieving a better filling of gear shape and a lower forming load requirement, and then the distribution of different field-variables such as flow velocity and effective strain are thoroughly investigated. For verification purposes, the cold rotary forging experiments of 20CrMnTi alloy spur bevel gears are subsequently conducted.

Domblesky, Shivpuri and *Painter* [126] applied the finite-element method to the radial forging of large diameter tubes. A rigid-thermo visco-plastic finite-element based model was considered, and the effective strain, strain rates, and temperature distributions in the forged tube was presented. The deformation was uniform and sensitive to the axial feed-rate. Strain rates were found to be sensitive to the axial feed rate and were within the range typical for a mechanical press. Across the wall thickness in the tube large temperature gradients were predicted.

The deformation pattern during sinter-forging process is influenced by several important factors like preform density, strength, elongation, barreling, shape-complexity, temperature, flow stress and die-workpiece interface frictional conditions, die velocity and acceleration, as well as factors related to forging equipment, like deformation speed and contact times under load. The problem lies in recognition of these important factors, which interact with each other in a complex manner and estimation of dynamic effects, which critically influence the average die load involved during sinter-forging process, especially at higher die velocities.

A very few investigators have carried out research into dynamic effects during mechanical processing of wrought materials. *Lippmann* [127] carried research to generalize the elementary theory of plasticity for the case of forging with high acceleration, when inertia effects can no longer be neglected. The wave propagation effects were neglected as the velocity of stress waves is expected to lie higher than 200 m/s. The analysis based on equilibrium approach considers high-speed compression of a specimen between plane rigid parallel platens of a hydraulic press up to relative die velocity of about 7 m/s. According to investigations, the dynamic effects can occurs in

three ways. Firstly, when die with a certain relative velocity before the beginning of deformation loses a part of it by the impact, during which the specimen gets the kinetic energy. In this case, the entire forging operation is considered as one plastic impact. Secondly, during the real deformation processes, the die velocity reduces to zero and initially accumulated kinetic energy supports the plastic flow with diminishing forging force. Lastly, the negative forces have also formally generated, which in reality has moved the specimen away from the dies and thus, deformation proceeds only by means of specimen's own kinetic energy.

Hilllier [128] estimated the dynamic forces in case of very high-speed impact forging of disks and slabs under axi-symmetric and plane strain condition respectively with both smooth and perfectly rough dies. The analysis considered coulomb friction law and three methods of analysis *i.e.* approximate equilibrium approach, energy method and upper-bound approach based on kinematically admissible velocity field. The strain hardening, strain rate and temperature effects were neglected. The material was assumed to be homogeneous and isotropic and yield stress value was adjusted to take into account of strain rate, strain hardening and temperature suitably for all practical purposes. The material was considered to be incompressible, *i.e.* elastic strains were neglected and obeys Von Mises yield criterion. The inertia forces normal to the die face were considered to be negligible compared to inertia forces parallel to the die face. The influence of plastic waves was also not considered. The dynamic effects were illustrated by calculating the die velocity required to double the maximum die pressure, as compared with a slow static forging. The investigations showed about 40 percent underestimate in die pressure, when dynamic effects were neglected at a die velocity of about 200 m/s.

Osakada et. al. [129] carried experimental investigations to study the impact of dynamic effects on mechanical properties of mild steel specimen during cold and warm high-speed forging under plane strain condition. The effect of deformation speed, strain and temperature on yield stress, flow stress, ultimate tensile stress, work hardening, elongation, cross-section reduction and hardness of mild steel specimen during high-speed forging are critically studied, discussed and results were compared with those after low-speed forging. The high-speed forging operations were performed on a Hi-fomac

press driven by nitrogen gas with maximum impact energy of 1.1 ton m and pressure of 150 kg/cm^2. The forging speed was kept at about 15 m/s at an average strain of about 500/s. The low-speed forging was performed in a 100-ton hydraulic press with a ram speed of 0.3 mm/s at an average strain of about 0.015/s. It was concluded from the investigations that at room temperature, high-speed forging showed lower yield stress, ultimate tensile stress and hardness than low-speed forging. Consequently, higher values of elongation, reduction in area and impact strength was obtained. The impact strength values of high-speed forging are greater than those of low-speed forging with same hardness, although the tensile test results exhibit same values for the same hardness. The yield stress and hardness were maximum at 400^0 C for a forging strain of 0.14 under high-speed forging and hence, considered to be optimum temperature of high-speed forging. It was observed that yield stress and hardness of high-speed forging were lower than those of low-speed forging at forging temperatures up to 400^0 C and the relation was reversed at temperatures above 400^0 C.

Dean et. al. [130] and *Jones et. al.* [131] carried out both theoretical and experimental investigations of dynamic effects in high-velocity compression of electrolytically pure copper specimens under plane strain and axi-symmetric conditions. The experiments were carried on an explosively driven compression-testing machine up to strain rates as high as 4000/s with an objective to study dynamic aspects *e.g.*strain rates and inertia effects. The analysis assumed free-flight of moving press platen prior to impact. The plastic wave propagation effects were neglected. The investigations concluded that experimental strain rate variations were in reasonable agreement with the theory. The material work hardens during deformation at ambient temperature and thus, produces higher strain rates than a perfectly plastic material. The stress-strain curves obtained during high-velocity plane strain and axi-symmetric compression, although similar in level, were markedly different in shape. The high-speed plane strain compression compared with upsetting operation produces increased stresses at low strains and lower stresses at intermediate strains, which tend to increase with increase in billet size. It was demonstrated that the effects of billet inertia on flow stress are considerably more pronounced in plane strain than in axi-symmetric compression. Finally, it was concluded

that experimental strain rate variations are in reasonable accord with the analysis, however, inertial theory was in qualitative agreement with results of high-velocity plane strain and axi-symmetric compression tests.

Tobias et. al. [132-133] studied the effect impact of die speed and lubrication conditions on interfacial friction conditions, die pressure, metal flow pattern, die cavity fill and required forging load during high-speed hot forging process. The experiments were performed on Mk II Petro-Forge machine capable of providing ram speed of 6.5 to 20 m/s approximately. The comparisons were made with slow-speed forging, which was performed on a hydraulic press capable of providing die speed up to 0.06 m/s. Four different interfacial friction conditions were considered using graphite, clean dry dies and lightly oxidized billets. Ring test were employed to determine the frictional restraints at billet-die interface during metal flow. It was concluded from the investigations that for a given condition of lubrication, the coefficient of friction decreases with increased with impact velocity and depends modest on the change in die velocity during deformation. The frictional forces are lowest for copaslip and graphite lubricants in case of Petro-Forge machines and hydraulic press respectively, though pressure rise was observed highest using copaslip. The deformation load required to upset ring specimens increases with interfacial friction and lower upsetting load were required using copaslip than graphite lubricant. The mode of flow during deformation is similar on Petro-Forge machines irrespective of type of lubricant used.

Chitkara and *Bhutta* [134] estimated the dynamic forces during high-speed impact forging. The dynamic heading of triangular, hexagonal, and octagonal shaped heads, specimens made of tellurium lead and commercially pure aluminium was experimentally investigated. During deformation of the materials into head shapes conducted under low-velocity drop weight impact situations the characteristic die load-time and die movement-time results were observed. Results were compared to those calculated from a modified simple upper bound analysis which takes into account the inertia forces in the undeformed material. And found in general, 20% - 40% higher than the similar quasi-static loads, showing good correlations with the experimental results.

Jha et. al. [135] and *Singh et. al.* [136-138] reported various technological aspects of a high-speed sintered forging process. Experiments were conducted and measurement were made in development of barreling strain variation at free surface and densification during dry lubricated high-speed cold forging of sintered copper powder discs. The theoretical analysis for both plane strain and axi-symmetric deformation was done based on Upper Bound approach and the inertia effects were thoroughly analyzed using inertia factor.

The literature survey suggests and reveals that many researchers have carried extensive investigation in the area of powder metallurgy, especially during fabrication of the sintered preforms, deformation characteristics and their complex interaction and other sinter-forming aspects including as finite element simulation of wrought materials. But not much work has been reported for the finite element simulation of sintered materials, especially sinter-forging processes. Thus, the present work is strategically important from the point of view that it is not only an attempt to simulate the sinter-forging processes but has also provided the basic formulations for the associated plasticity model for sintered materials, which can be successfully utilized to perform the finite element simulation of various sinter-forging processes.

CHAPTER 3
BASIC EXPERIMENTAL WORK

In order to carry out the finite element analysis of all the three categories of the sinter-forging processes, i.e. open-die sinter-forging, closed-die sinter-forging and rotary sinter-forging, it was necessary to carry out initial basic experimental work, whose results can be utilized to formulate the plasticity model and finite element constitutive relations for sintered materials. The basic experimental work consists of fabrication of powder compaction die, fabrication of forging die-sets and measurement of various deformation characteristics during different sinter-forging processes considered under the present research work.

3.1 FABRICATION OF POWDER COMPACTION & FORGING DIES-SETS

Closed cavity powder compaction die-sets of hardened alloy steel having good surface finish were fabricated for the fabrication of preforms with different shapes as required for the present research work. For fabrication of cylindrical preforms, closed circular cavity powder compaction die-sets having bore diameters as 20.0, 25.0, 30.0 and 40.0 mm were fabricated as shown in figure 3.1. For fabrication of square preforms, closed square cavity powder compaction die-sets having cavity side length as 35 mm were fabricated as shown in figure 3.2. All the die-sets were fabricated in three separate parts, i.e. flat upper punch, lower counter punch with obtrude recess and a central container to house punch and counter-punch and the inner walls were finished to a good surface finish with polishing paste. These preforms were then subsequently machined to required dimensions to fabricate cylindrical preforms with varying aspect ratios, hollow preforms, truncated conical preforms and trapezoidal preforms. To conduct experiments for closed-die sinter-forging of cylindrical preforms into double-hub flange components, closed die-set comprising of moving upper and stationary lower counter punches housed in a central container of 30.0mm diameter has been used. Both the punches have cylindrical recess-cavities, with depth and diameter equal to length 5.0mm and diameter 20.0mm

respectively as shown in figure 3.3 (a) & (b). These cavities help in minimizing the variability and difficulty in preform location within the closed-die sets. The inner walls of all the die sets has been finished to a good surface finish with polishing paste. For rotary forging tool, upper conical dies with half cone angle as 5^0, 10^0, and 15^0 with vertical axis been fabricated. The design of upper conical rotary forging die and die tool holder are shown in figure 3.4 (a) & (b). As evident from the figures, the conical front face of the upper die has been fabricated separately and assembled with the backing face in such a way that when the axis of the die is kept vertical, one of the generator of the conical front face of the upper die is horizontal and parallel to the top surface of the cylindrical preform. Further, the complete from end of the upper die is then assembled with the die tool holder which is used to mount the die on the rotary spindle. Figure 3.5 (a) & (b) shows the conical front end of rotary die and the assembled rotary forging die-set. Table 3.1 summarizes the description of all the die-sets fabricated for the present research work.

(a)

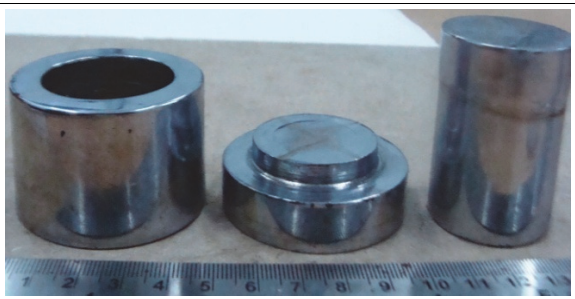

(b)

Figure 3.1(a) & (b): Closed Circular Cavity Powder Compaction Die-Sets.

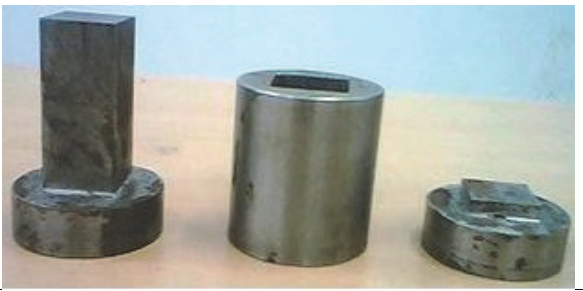

Figure 3.2: Closed Square Cavity Powder Compaction Die Set.

Figure 3.3: Die Set for Closed-Die Sinter-Forging.

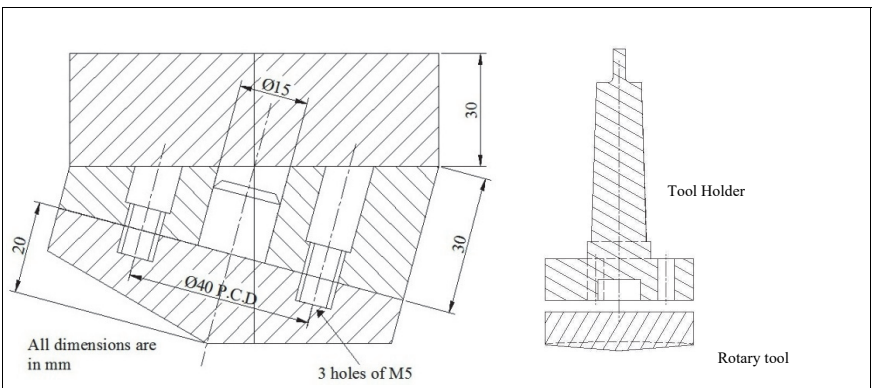

Figure 3.4: Design of Upper Conical Rotary Forging Die and Die Tool Holder.

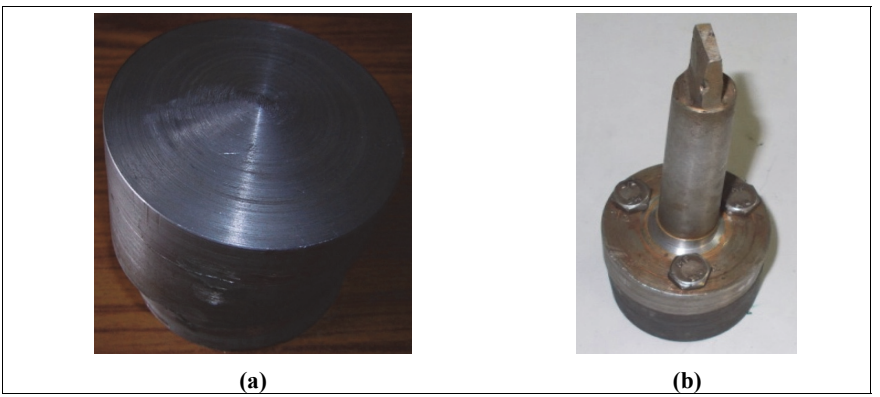

(a) **(b)**

Figure 3.5: Illustration of Conical Front End of Rotary Die & Assembled Rotary Forging Die.

TABLE 3.1: Summary of Different Die-Sets Fabricated.

SL. No.	Die Type	Dimension	Description	Function
1.	**Closed Circular Cavity Powder Compaction Die-Sets**	Bore Diameter = 20.0, 25.0, 30.0 and 40.0 mm	Moving flat upper punch, stationary lower counter punch with obtrude recess and central container to house punches	Fabrication of metal powder hollow, truncated conical and cylindrical preforms
2.	**Closed Square Cavity Powder Compaction Die-Set**	Cavity side length = 35.0 mm		Fabrication of metal powder trapezoidal preforms
3.	**Closed-Die Forging Die-Set**	Bore diameter of central cylindrical = 30.0 mm, Depth of cylindrical recess-cavity = 5.0 mm with diameter = 20.0 mm		Closed-die sinter-forging of cylindrical preforms into double-hub flange components
4.	**Rotary Forging Die-Set**	Cone apex angle = 170^0, 160^0 & 150^0	Cone axis of upper die inclined at an angle of 5^0, 10^0 & 15^0 with vertical axis	Rotary sinter-forging of cylindrical preforms

3.2 FABRICATION OF ALUMINIUM METAL POWDER PREFORMS

Atomized Aluminium metal powder having purity and particle size more than 99 percent and 13.0 microns respectively has been used to fabricate metal powder preforms of required shapes. Based on requirements of the basic experimental work, cylindrical, hollow disc, truncated conical and trapezoidal preforms were fabricated by machining the compacts prepared by compacting the metal powder. The physical characteristics, such as particle sizes, apparent and tap densities along with the chemical characteristics for Aluminium metal powder is shown in tables 3.2 [136], as provided by the manufacturer.

TABLE 3.2: Physical & Chemical Characteristics of Aluminium Metal Powder.

Particle Size (µ)	Weight Under (%)	Chemical Analysis	Weight (%)
118.0	100.0	Aluminium	99.500
88.1	98.9	Iron	< 0.1700
65.6	95.5	Silicon	< 0.1313
48.8	88.8	Zinc	< 0.0053
36.3	79.0	Manganese	< 0.0023
27.0	65.8	Magnesium	< 0.0016
17.4	40.1	Apparent density	1.25 gm / c.c.
13.0	25.5	Tap density	1.50 gm / c.c.

The metal powders were compacted in respective closed circular cavity and square cavity compaction dies using a 100-ton hydraulic compaction universal testing machine as shown in figure 3.6 (a). The compaction of Aluminium metal powder has been performed at pressures of 5-8 tonf approximately. The die walls were lubricated with graphite paste prepared by mixing fine graphite powder and mineral oil. The Aluminium metal green compacts were sintered at about 400^0 C temperature for four hours in an endothermic atmosphere. The sintering operations were carried in order to develop mechanical strength in the metal powder compacts. Subsequently, these compacts were wrapped in a 'Teflon' sheet and repressed at the same compaction pressure in the same die and again re-sintered at the same temperature for same duration of time, to obtain uniform density

distribution. All the sintering operations were carried in a muffle-type furnace, which is capable of providing temperatures up to 1200^0 C as shown in figure 3.6 (b).

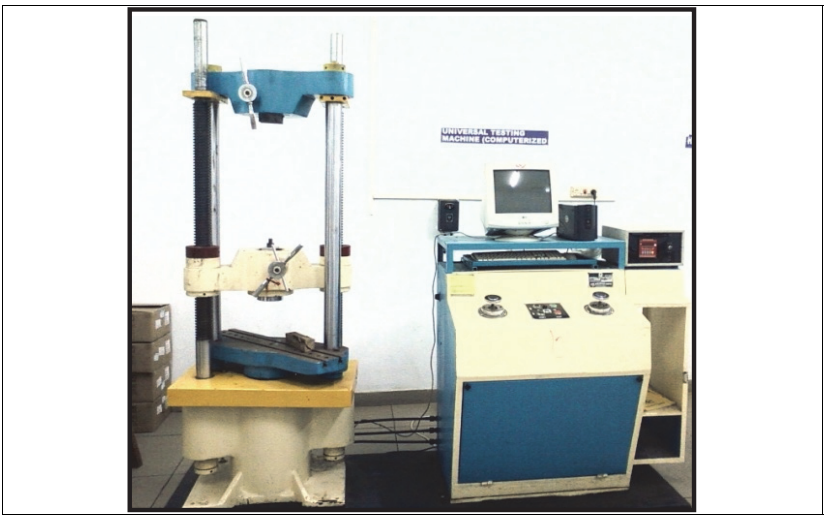

Figure 3.6 (a): UTM for Powder Compaction.

Figure 3.6 (b): Muffle Furnace.

The sintered compacts were finally machined to the required dimensions and polished with coarse and fine emery papers. The preforms actual densities were computed by

measuring its dimensions and weight. The relative densities were obtained as the ratio of actual density of the preform to the density of corresponding wrought metal. The Aluminium metal powder cylindrical preforms have been machined to the required dimensions of 20.0, 15.0 and 10.0 mm radius with heights corresponding to the preform aspect ratio of 1.0, 0.75, 0.50 and 0.25 respectively for open-die sinter-forging analysis as shown in figure 3.7(a) and (b). Additionally, the sintered metal powder compacts having initial diameter as 30.0 mm were machined to obtain hollow preforms with height as 10.0mm, outer radius as 12.0 mm and varying inner radius as 4.0, 6.0, 7.5 & 10.0 mm corresponding to the respective shape-complexity factors as shown in figure 3.8. The truncated conical preforms has been obtained by machining cylindrical compacts with 30.0mm initial diameter to height as 17.0 mm, larger radius as 12.0 mm and varying smaller radii as 7.5, 9.0 & 11.0 mm corresponding to half cone angles 15^0, 10^0 and 5^0 respectively and respective shape-complexity factors as shown in figure 3.9. The trapezoidal preforms were obtained by machining Aluminium metal powder square compacts with 35.0 mm initial side-length to the required dimensions depending upon the corresponding shape-complexity factors as shown in figure 3.10. To investigate the flow of material during sinter-forging trapezoidal preforms and to approximate the regions of kinematically admissible velocity field, the preform surface was divided into different zones having symmetrical regions. These regions were obtained by drawing perpendiculars to the sides of the preform from the point of intersection of angle bisectors as shown in the figure 3.11. For closed-die sinter-forging analysis, the cylindrical preforms were machined to the required dimensions of 10.0 mm radius and height as 20.0, 15.0 & 10.0 mm corresponding to the preform aspect ratio of 1.0, 0.75, and 0.50 respectively. The dimensions of all metal powder preforms used for basic experimental investigation are summarized in tables 3.3 and 3.4.

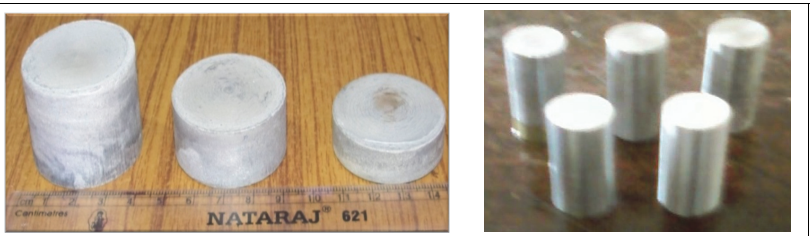

(a) (b)

Figure 3.7 (a) & (b): Cylindrical Metal Powder Preforms.

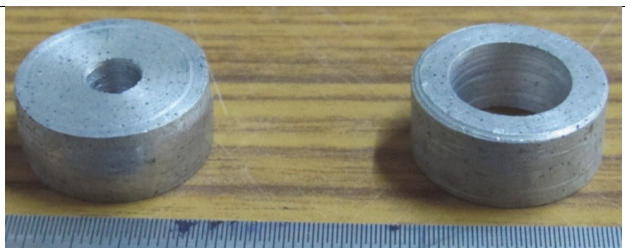

Figure 3.8: Hollow Aluminium Metal Powder Preforms.

Figure 3.9: Truncated Conical Aluminium Metal Powder Preforms.

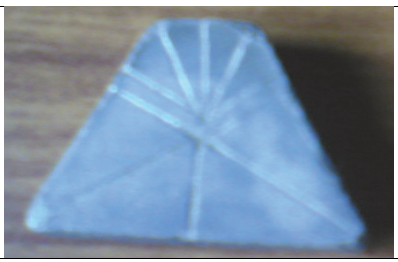

Figure 3.10: Irregular Polygonal Aluminium Metal Powder Preforms.

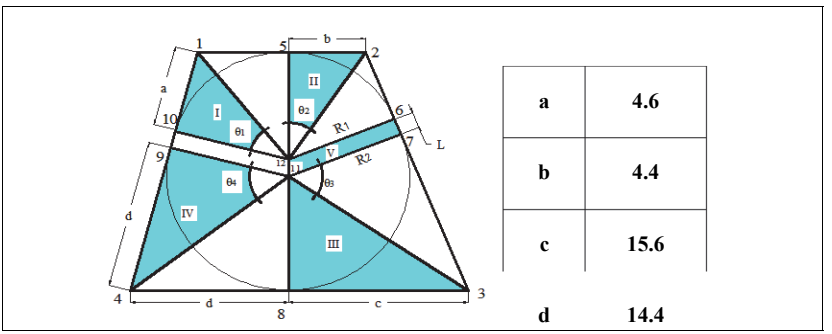

a	4.6
b	4.4
c	15.6
d	14.4

Figure 3.11: Trapezoidal Preform with Symmetrical Regions.

TABLE 3.3: Dimensions of Sintered Metal Powder Preforms for Open-Die Forging

(all dimensions are in mm).

Preform Shape	Preform Characteristics								
Cylindrical	$\rho_o = 0.8$								
	Diameter	40.0			30.0			20.0		
	Length	10.0	20.0	30.0	7.5	15.0	22.5	5.0	10.0	15.0
	Aspect Ratio	0.25	0.5	0.75	0.25	0.5	0.75	0.25	0.5	0.75

Hollow	$\rho_o = 0.80$, $r_o = 12.0$, H = 10.0	
	$C_p = r_o / r_i$	r_i
	3.0	4.0
	2.0	6.0
	1.5	8.0
	1.2	10.0

Truncated Conical	$\rho_o = 0.80$, $r_{to} = 12.0$, H = 17.0		
	$C_f = r_{to} / r_{ts}$	α	r_{ts}
	1.1	5^0	11.0
	1.3	10^0	9.0
	1.6	15^0	7.5

Irregular Trapezoidal	$\rho_o = 0.80$, H = 17.0							
	$C_q = R_1 / R_2$	a	b	c	d	L	R_1	R_2
	0.85	6.5	5.5	16.0	14.0	0.8	9.2	10.8
	0.60	4.6	4.4	15.6	14.4	3.6	7.5	12.5

TABLE 3.4: Dimensions of Sintered Metal Powder Preforms for Closed-Die & Rotary Forging ***(all dimensions are in mm).***

Forging Operation	Preform Shape	Preform Characteristics
Closed-Die Forging	**Cylindrical**	**ρ_o = 0.8, R = 10.0, R_o = 15.0, H = 30.0, 22.5 & 15.0 H/R_o = 0.5, 0.75 & 1.0**
Rotary Forging	**Cylindrical**	**ρ_o = 0.8, R_o = 15.0, H = 10.0**

3.3 MEASUREMENTS OF SINTER-FORGING CHARACTERISTICS

Basic experiments were conducted to determine and investigate the effect of various compaction characteristics like compaction pressure, sintering temperature, sintering time on preform relative density during the fabrication of the preforms and the data was suitably plotted. Also, the complex interactions of the various deformation characteristics like strain rates, preform height reduction, Poisson's ratio, densification rate, forging load during various categories of sinter-forging processes were investigated and the relevant graphs were also plotted.

Figure 3.12 shows the variation of perform relative density with respect to the compaction pressure. It was found that relative density of the perform increases with increase in compaction pressure and this is because high compaction pressure leads to better consolidation of the powder particles and decrease in the inter particles pores within the preforms, which is confirmed with the research work of *Kao* [40], who carried out extensive investigation to the compacting behavior of ferrous powders. Figure 3.13 shows the variation between preform relative density and sintering temperature and it is evident that relative density increases with increase in sintering temperature and also the corresponding values of the relative density is higher for higher compaction pressure. The increase in relative density is attributed due to some kind of diffusion process happening within the performs during sintering, which leads to better bonding between the powder particles, as well as, decreases the inter particle pores size. This is confirmed by work carried out by *Difai* and *Standring* [68, 96].

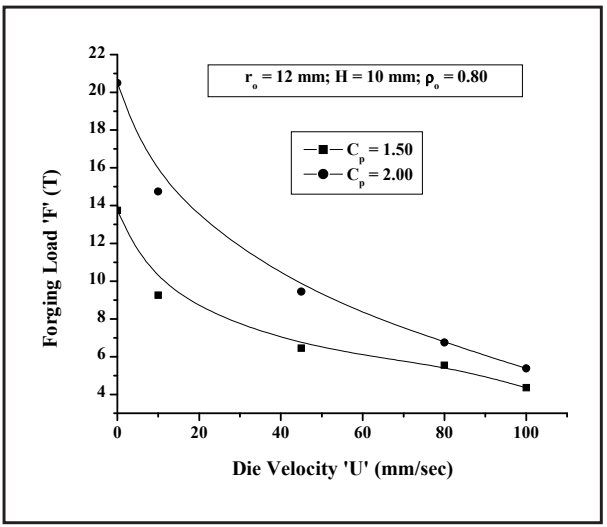

Figure 3.12: Variation of Relative Density with Compaction Pressure.

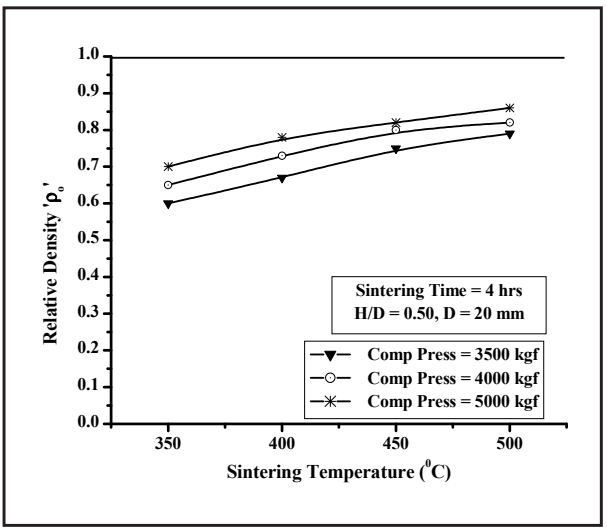

Figure 3.13: Variation of Relative Density with Sintering Temperature.

3.3.1 Measurements during Sinter-Forging of Cylindrical Preforms

The compacted cylindrical Aluminium metal powder preforms were forged using UTM under lubricated interfacial friction condition (graphite paste prepared by mixing fine graphite powder and mineral oil) and dry condition (no lubricant) at room temperature under open-die forging condition using flat and parallel die platens. The various deformation characteristics like percentage height reduction, percentage change in radius, forging load, axial strain, radial strain, Poisson's ratio, change in relative density and rate of densification were investigated. In order to evaluate forgeability, the cylindrical preforms of known initial relative density were forged at room temperature and, the forging load was gradually increased until a crack was observed by the naked eye on the equatorial free surface of the preform. The strains, height reduction at corresponding forging load at the instant of the appearance of the cracks were recorded for all the specimens at varying die speed and different frictional conditions at room temperature. The maximum height reduction without the occurrence of external cracks was observed to be about 42 percent under lubricated conditions at highest die speed, whereas for lower die speeds and high interfacial friction conditions, the formability was been observed to be low, i.e. 30 to 35 percent of preform height reduction. This holds good only under the forging conditions as described above.

Suitable graphs were plotted using the data measured and recorded during the experimentation, which were critically examined and investigated and results were reported and discussed. Figures 3.14 shows the illustrations of the cylindrical Aluminium metal powder preform with cracks after forging process.

Figure 3.14: Formation of Cracks on Cylindrical Aluminium Preform.

Figure 3.15 shows the variation of relative density of perform with height reduction of the specimen during forging. It is evident that relative density increases with increase in height reduction and becomes comparable to that of wrought materials at the end operation. The lubricated performs exhibit better densification than the unlubricated ones (dry conditions). Also the preforms with higher aspect ratio become more densified as compared to the ones having smaller aspect ratio. This is so because of flow of preform material is better in case of slender performs and at lubricated conditions. This completely agrees with the work of *Fischmeister* [29]. Figure 3.16 shows the variation of radial and axial strains with preform height reduction under lubricated and dry frictional conditions. The radial and axial strain increases exponetionally with the preform height reduction, which was also detected by *Kuhn* [1]. It can also be seen that the strains during lubrication friction condition is higher as compared to the dry condition due to better flow of the material. Figure 3.17 shows the variation of Poisson's ratio with preform height reduction. The theoretical curve for Poisson's ratio represents the relation between radial and vertical strains for a fully dense material (slope of one half, i.e. $\nu = 0.5$) or wrought materials. The curves for porous materials are below the theoretical curve (slope less than 0.5) but gradually become parallel to it, as full density is approached. The variation of Poisson's ratio for sintered materials may be plotted from this curve, as well as the theoretical variation of Poisson's ratio may also be plotted by empherical

equation, $\nu = 0.5\ \rho_o^2$ given by *Elwakil* [49]. It can be seen that the Poisson's ratio is higher for the lubricated conditions due to the better flow of material.

Figure 3.18 it shows relationship between Poisson's ratio with preform relative density under lubrication condition. It is evident that as deformation proceeds, the compaction of the preform takes place simultaneously with the deformation. Therefore, the relative density of preform increases, as well as, the Poisson's ratio also increases and approaches the theoretical value, i.e. $\nu = 0.5$, as shown by the extrapolated line on the graph. Figure 3.19 shows the forgeability evaluation on the sintered performs as per the conditions of the experimentation. It is evident that forgeability is better in lubricated conditions and higher for performs with higher aspect ratio. The forgeability is measured by the maximum possible height reduction of the preform just before start of the cracks on the equatorial regions. This is also confirmed by the work of *Tiwari* [71] and results completely agree with it. Figure 3.20 shows that the densification rate with preform relative density. Densification rate is defined as the ratio of change in preform relative density with time of deformation. The densification rate decreases with increase in relative density. This is because as preform are more densified during forging operation; their resistance to further deformation increases at same forging condition leading to decrease in the rate of densification.

Figure 3.21 it is variation of axial strain with forging load. It can be seen from figure that axial strain increases with the forging load but the curve is not similar to that of wrought materials and steels. The curve is below the curve for steels, which is due to the porosity present in the powder performs. During the sinter-forging process, the compaction of preform occurs simultaneously with the compression, where compaction leads to the closing of pores and hence preform densification, whereas, compression leads to deformation of the preform. Due to this phenomenon, some fraction of forging energy is expended for the densification of the preform, which is also confirmed by the work of *Huppmann* [60].

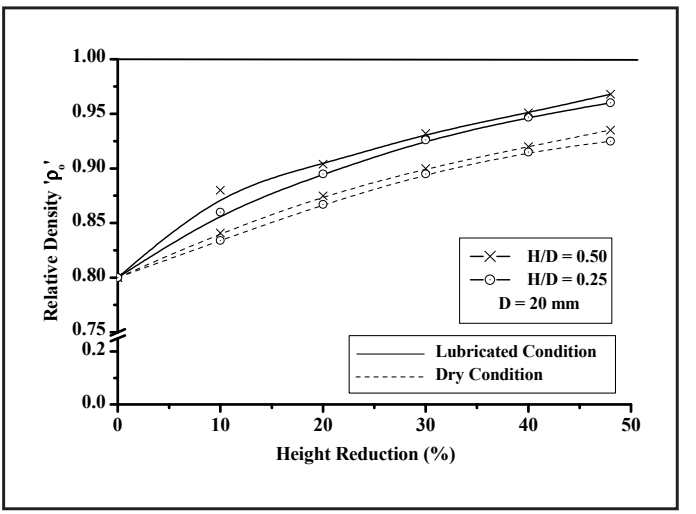

Figure 3.15: Variation of Relative Density with Height Reduction during Sinter-Forging of Cylindrical Preforms.

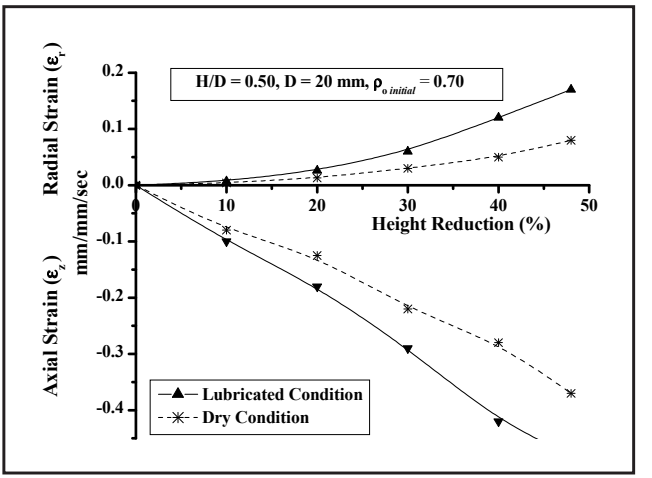

Figure 3.16: Variation of Radial & Axial Strains with Height Reduction during Sinter-Forging of Cylindrical Preforms.

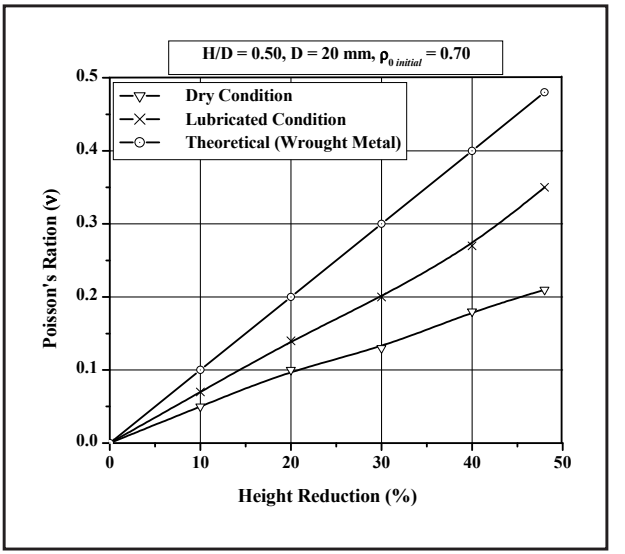

Figure 3.17: Variation of Poisson's Ratio with Height Reduction during Sinter-Forging of Cylindrical Preforms.

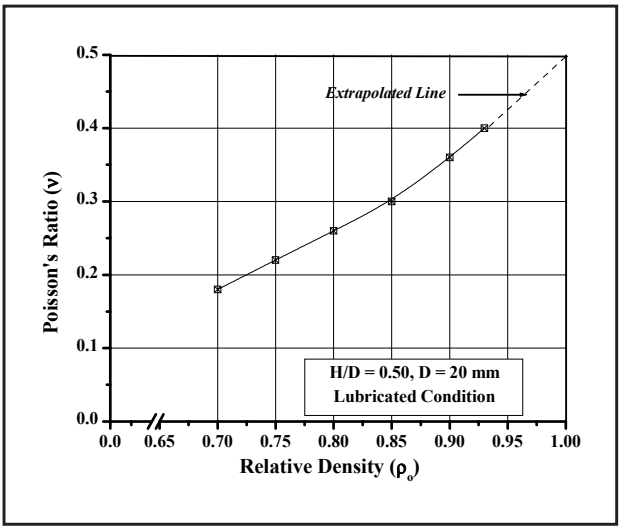

Figure 3.18: Variation of Poisson's Ratio with Relative Density during Sinter-Forging of Cylindrical Preforms.

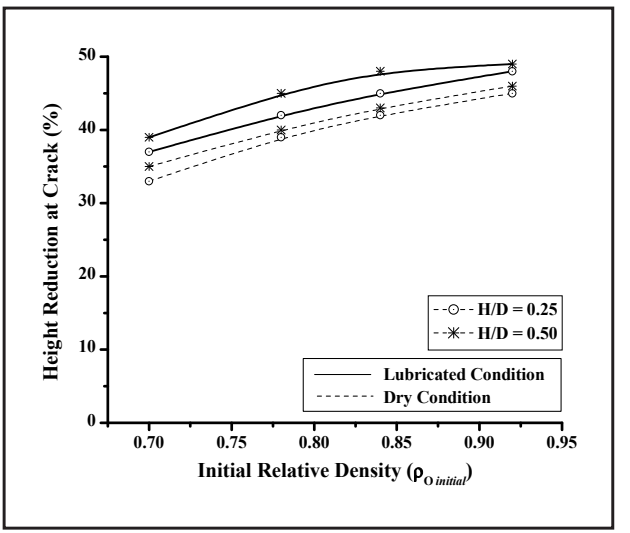

Figure 3.19: Variation of Forgeability with Initial Relative Density during Sinter-Forging of Cylindrical Preforms.

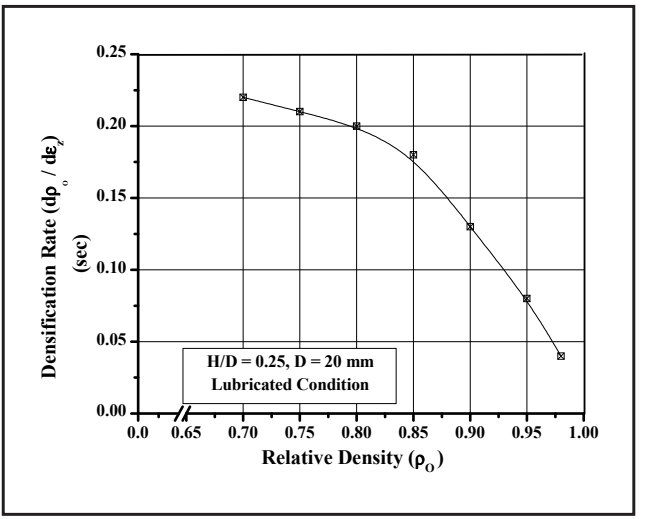

Figure 3.20: Variation of Densification Rate with Relative Density during Sinter-Forging of Cylindrical Preforms.

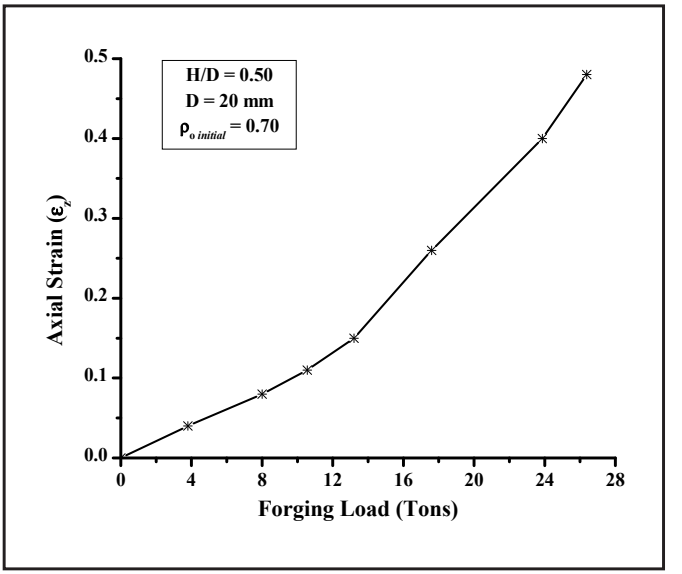

Figure 3.21: Variation of Axial Strain with Forging Load during Sinter-Forging of Cylindrical Preforms.

The photomicrographs of sintered preforms after forging were obtained at two different magnifications 200 and 500 X as shown in figure 3.22. Firstly, the preforms are rough grinded using different grades of emery papers, i.e. 180, 220, 320, 400, 600, 800, 1000 and fine polished with a 0.3mm diamond paste. Then, the specimens are washed and cleaned by ethyl alcohol and etched with krolle reagent (solution of 95ml distilled water, 3ml HNo_3 and 2 ml HF). The etched surface for all the samples were observed under metallurgical microscope and microstructures with grain boundary orientation were captured for detailed study. The microstructure of preform with percentage of height reduction revealed the pores to be much larger, irregular and more segregated at the initial stage and finally leading to well-defined grains with lesser porosity and increase in preforms relative density.

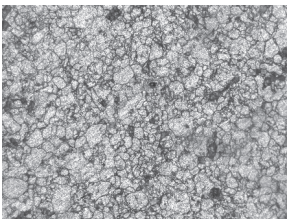

0% Reduction

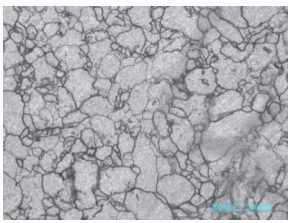

0% Reduction

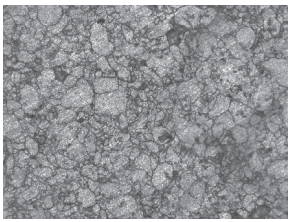

20% Reduction

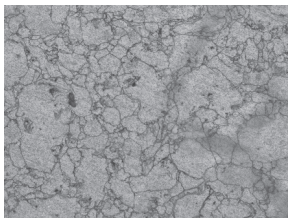

20% Reduction

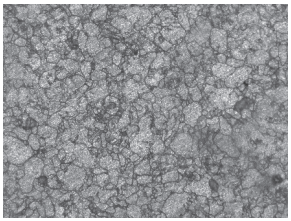

30% Reduction

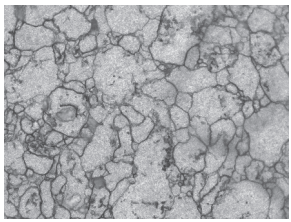

30% Reduction

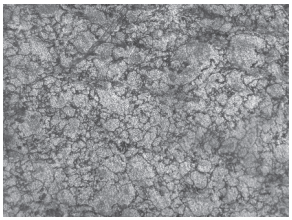

44% Reduction
(a) 200X Magnification

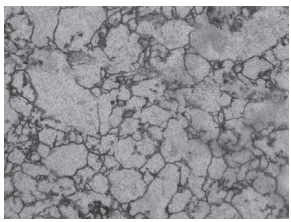

44% Reduction
(b) 500X Magnification

Figure 3.22: Photomicrographs of Sinter-Forged Preforms.

3.3.2 Measurements during Sinter-Forging of Hollow Preforms

To investigate various deformation characteristics, like percentage in height reduction, change in radius, corresponding forging load and preform relative density, during open-die sinter-forging of Aluminium hollow preforms, experiments were conducted considering three different die velocities 5, 10, and 100 mm/sec respectively, with high and low interfacial friction conditions of values 0.3 and 0.01. Suitable graphs were plotted using the data measured, which were examined and results were reported. Figure 3.23 shows the illustration of the specimen after the occurrence of cracks on the peripheral regions of the preforms. Figure 3.24 (a) and (b) shows the variation of outer and inner diameters with height reduction during open-die sinter-forging of hollow preforms. It is evident that percent change in diameters decreases with the increase in the die velocity. This is because higher die velocity results into impact loading due to small contact time and leads to higher densification of preform, as compared to sinter-forging operations at lower speeds. Also, the percent change in inner radius is observed to be small at low interfacial friction condition. This is because, the position of neutral radius lies in between the outer and inner radii of hollow preform for low interfacial friction conditions and the preform material in between inner and neutral radii, flows inwards and the rest flows outwards, resulting into small change in the inner radius.

Figure 3.25 shows the variation of relative density with the reduction in height of hollow preform at different die velocity under dry and lubricated frictional conditions. It was observed that compressive forces during plastic deformation gradually close down the inter-particle pores leading to decrease in the preform volume and increases the relative density, which in turn becomes comparable to that of wrought materials at the end of the forging process. Figure 3.26 shows the variation of die load with die velocity for hollow preforms under dry interfacial friction conditions. It can be seen that die load decreases with increase in die velocity. Sinter-forging operations with higher die speeds are characterized by very small contact time under deformation. The low duration of intimate contact between preform and die restricts the internal heat

generated due to plastic working to dissipate quickly and hence, reduces the preform resistance against deformation.

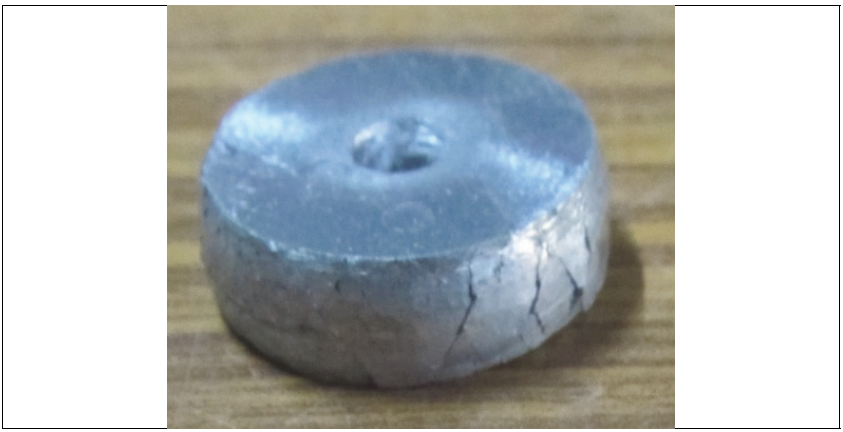

Figure 3.23: Formation of Cracks on Hollow Disc Preform.

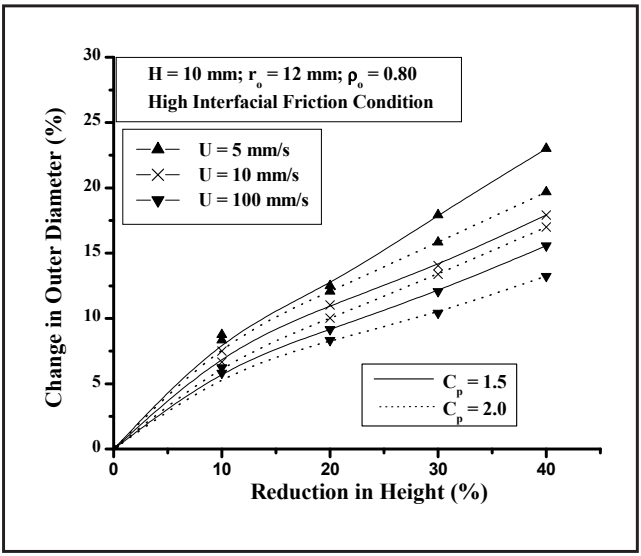

Figure 3.24 (a): Variation of Outer Diameter with Height Reduction during Open-Die Sinter-Forging of Hollow Preforms.

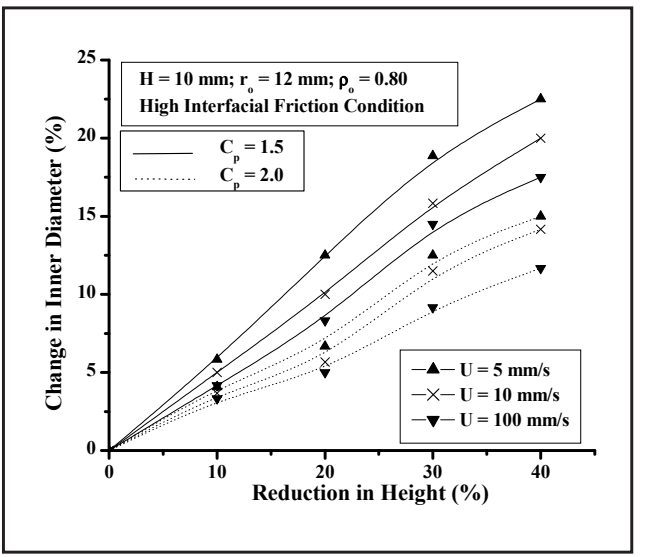

Figure 3.24 (b): Variation of Inner Diameter with Height Reduction during Open-Die Sinter-Forging of Hollow Preforms.

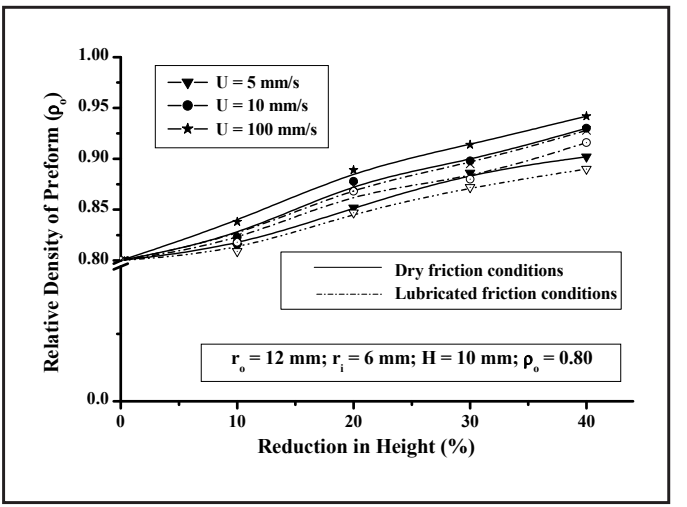

Figure 3.25: Variation Relative Density with Height Reduction during Open-Die Sinter-Forging of Hollow Preforms.

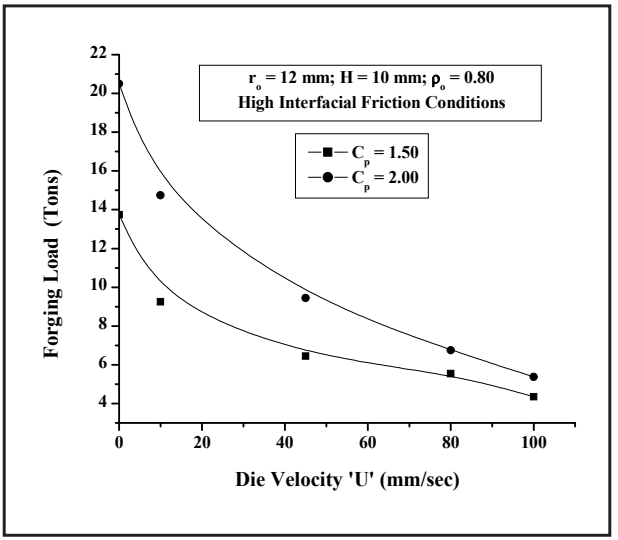

Figure 3.26: Variation of Die Load with Die Velocity during Open-Die Sinter-Forging of Hollow Preforms.

3.3.3 Measurements during Sinter-Forging of Truncated Conical Preforms

The present experimental investigation of sinter-forging of Aluminium truncated conical preforms, deals with the heterogeneous deformation due to barreling of its vertical sides, composite die-preform interfacial friction conditions and, densification along with compression. Three different die velocities 10, 100, and 150 mm/sec respectively, along with high and low interfacial friction values 0.3 and 0.01 respectively and preforms having different shapes were considered during the present analysis. The shape complexity factors tends to reduce to unity, when the shape of truncated conical preform approaches to that of an enclosing cylinder i.e. $r_{ts} \approx r_{to}$. Figure 3.27 shows the fractured truncated conical preforms after sinter-forging process. The variation of average forging load with die velocity under high interfacial friction condition for different shape-complexity factors is shown in figure 3.28. It is evident that die load decreases rapidly with the increase in die velocity. This is due to short contact time under deformation during sinter-forging operation at higher die velocity. The requirement for load is higher

for preform with low shape-complexity factor and high initial relative density. Thus, more densified un-lubricated preforms exhibit higher resistance against deformation and requires higher die load for deformation, as compared to less densified preforms.

Figure 3.27: Formation of Cracks on Truncated Conical Preform.

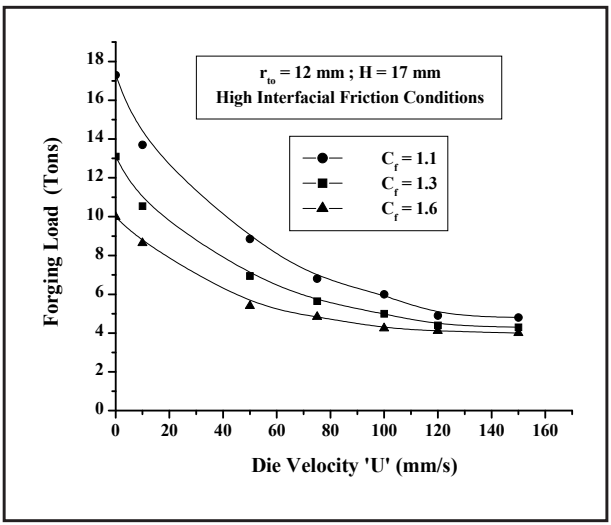

Figure 3.28: Variation of Forging Load with Die Velocity during Open-Die Sinter-Forging of Truncated Conical Preforms.

Figures 3.29 and 3.30 shows the variation and contour plot of radial and axial strain rate with preform height reduction at different die velocities respectively. It can be seen that both the strain rates increases exponentially with preform height reduction and the rate of

increase in axial strain is higher than the rate of increase in radial strain rate with increase in the die velocity. Also, the measure of the change in the strains observed at the two different faces of the truncated conical preforms are different. The end with lower diameter has more appreciable flow and deformation as compared to the end with larger diameter and this also confirms the assumption to be made during the subsequent finite element analysis. The contour plot also gives the measure of the Poisson's ratio of the sintered material, which is varying in nature due to closing of the inter-particle pores. It can be clearly seen that Poisson's ratio increases and becomes almost 0.5 (comparable to wrought materials) at the end of the sinter-forging process due to densification of the preforms. Figure 3.31 shows the variation of relative density with percent height reduction for different shape-complexity factors and interfacial friction conditions. It is clear from the figure that relative density of preforms increases with deformation and becomes comparable to that of wrought metals at the end of operation.

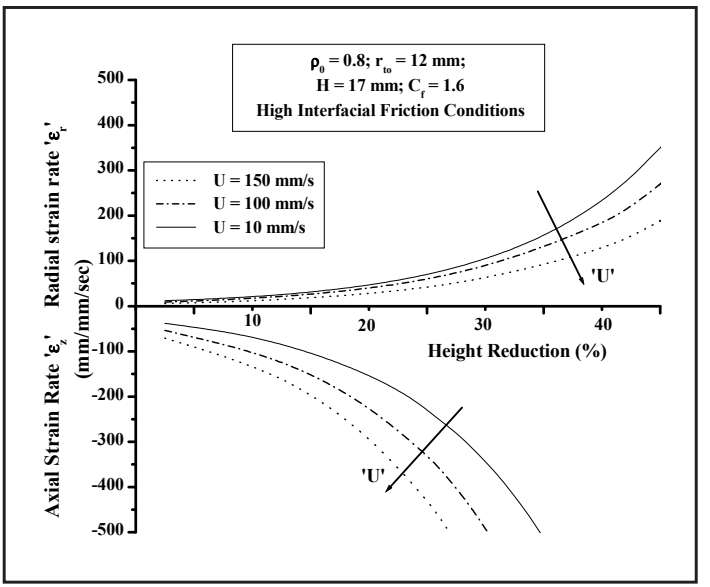

Figure 3.29: Variation of Radial & Axial Strain Rates with Height Reduction during Open-Die Sinter-Forging of Truncated Conical Preforms.

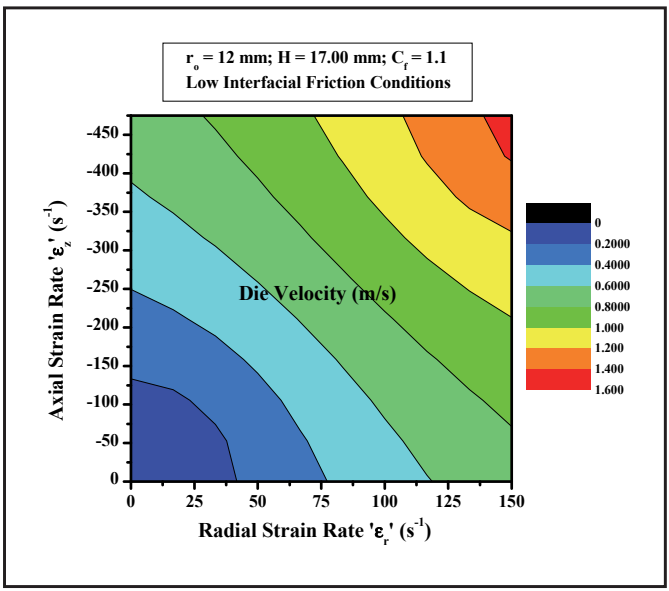

Figure 3.30: Contour Plot of Radial & Axial Strain Rates during Open-Die Sinter-Forging of Truncated Conical Preforms.

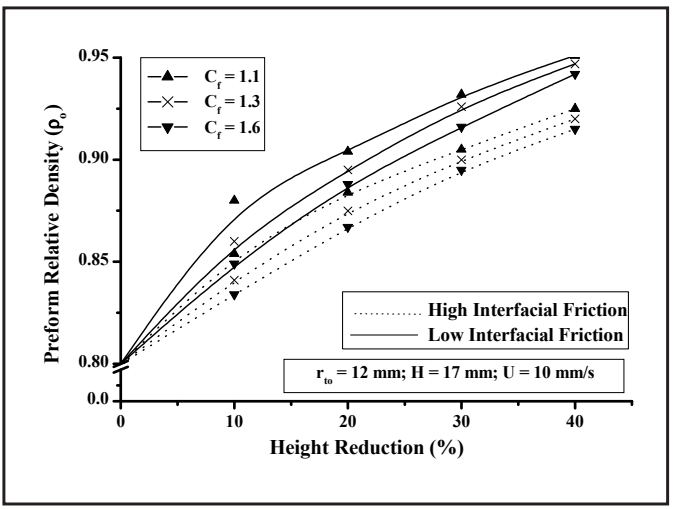

Figure 3.31: Variation of Preform Relative Density with Height Reduction during Open-Die Sinter-Forging of Truncated Conical Preforms.

3.3.4 Measurements during Sinter-Forging of Irregular Trapezoidal Preforms

During sinter-forging of Aluminum irregular trapezoidal preforms three different die velocities 10, 100, and 150 mm/sec, with high and low interfacial friction conditions of values 0.3 and 0.01 respectively were considered. Figure 3.32 shows the illustration of the irregular trapezoidal preforms before and after sinter-forging process. It can be seen that symmetrical regions on the surface of the preform remains unaltered and the lines dividing these regions remain straight confirming zero or negligible velocity jumps across the boundaries regions and thus, are having kinematically admissible velocity field. The variation of relative density of preform with the height reduction is shown in figure 3.33. It can be seen that as forging proceeds, preform height reduces and its relative density increases exponentially till 0.9, and later remains fairly constant. This confirms that both compaction (closing of inter-particle pores) and compression (deformation) occurs simultaneously but initially, compaction dominates over compression and increase in relative density is predominant but in the latter stages of forging, it is found vice-versa. Figure 3.34 the variation of die load with die velocity for different shape complexity factors. It can be noted that preform requires higher forging load to deform, with decrease in the die velocity. The load decreases rapidly and become asymptote to x-axis at higher die speeds, which is due to smaller contact time between die and preform.

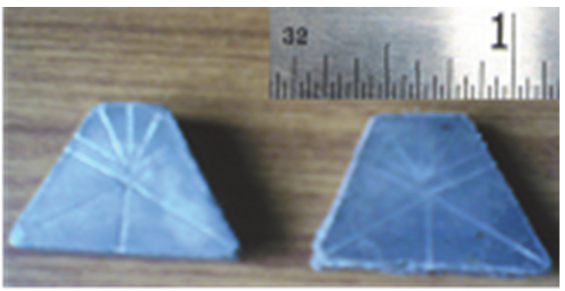

Figure 3.32: Symmetrical Regions on the Irregular Trapezoidal Preforms before and after Open-die Sinter-Forging Process.

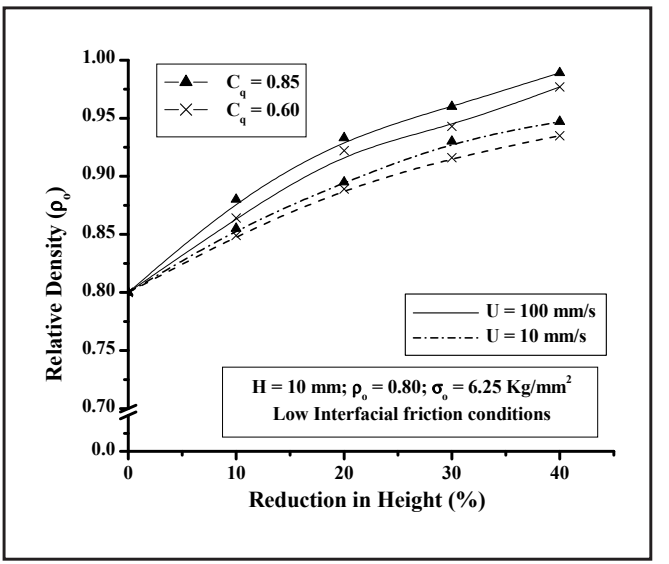

Figure 3.33: Variation of Relative Density with Height Reduction during Open-die Sinter-Forging of Irregular Trapezoidal Preforms.

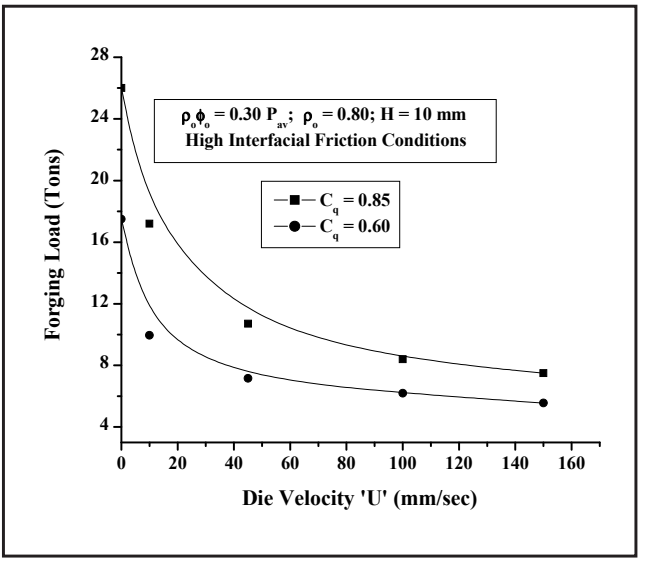

Figure 3.34: Variation of Die Load with Die Velocity during Open-die Sinter-Forging of Irregular Trapezoidal Preforms.

3.3.5 Measurements during Closed-Die Sinter-Forging of Double-Hub Flange Components

Flashless closed-die sinter-forging is an extremely complex process from the point of view of deformation characteristics, due to unsteady state and non-uniform metal flow along the die constraints. The non-uniformity in density distribution and complex die-preform-container interfacial friction conditions during processing of sintered materials further adds to the complexity and the difficulty in the analysis. Cylindrical preforms were centrally located within the closed-die sets and forged to different die travels (height reductions) till the die corner fillings were complete. The die loads and preform dimensions were noted at subsequent instances of the height reductions and die corner fillings to compute the percentage of unfilled volume of the dies. It was assume that the die filling is almost complete, when the forging load has increased exponentially high. The entire forging operations were performed at three different die velocity, i.e. 1, 10 and 100 mm/sec and suitable graphs were plotted using the data measured during the experimentation, which were investigated and results are reported. Figure 3.35 shows the double-hub flange components after two subsequent stages of sinter-forging process. It could be observed that as deformation proceeds, the free vertical face of the cylindrical preform bulges out with reduction in height till it reaches and touch the die-container sidewalls. Subsequently, the constrained deformation of bulged preform follows, where die-corners are formed and filled.

The variation in height reduction with die velocity for different preform aspect ratio during closed-die sinter-forging has been recorded and is displayed in figure 3.36. It is evident from figure that preform with higher aspect ratio exhibits higher percent reduction in height, which indicates that during compression or deformation, slender preforms deforms comparatively more than shorter preforms under same forging loads. Figure 3.37 shows the change in relative density of preform with forging load and, it is found to increase with increase in forging load, and die-cavity fills (as the preform material flows along the container and die-wall constraints). The densification is also comparatively better for sinter-forging process at slower die velocity than at higher velocity. Figure 3.38 shows the variation of average forging load with the ratio of unfilled

volume of die to components' actual volume for different preform aspect ratios and die velocity. Die filling was determined based on the dimensions of the sinter-forged preforms. A profile projector was used for tracing corner profiles of forging in order to find the unfilled volumes at the top and bottom of the die cavity. It is can be observed from the figure that forging load increases and becomes exponentially high at the end of forging operation. This is attributed due to high constraint deformation and resistance against metal flow during final stages of the die filling. The load curves are also higher for higher preform aspect ratio. It seems to be mainly of two prominent reasons. Firstly, the geometry of corners differs with preform aspect ratio, due to difference in barreling (during free deformation stage) and secondly, the preform with lower aspect ratio will have smaller contact areas with container walls, resulting into low friction shear energy dissipations.

Figure 3.35: Sinter-Forged Double-Hub Flange Components.

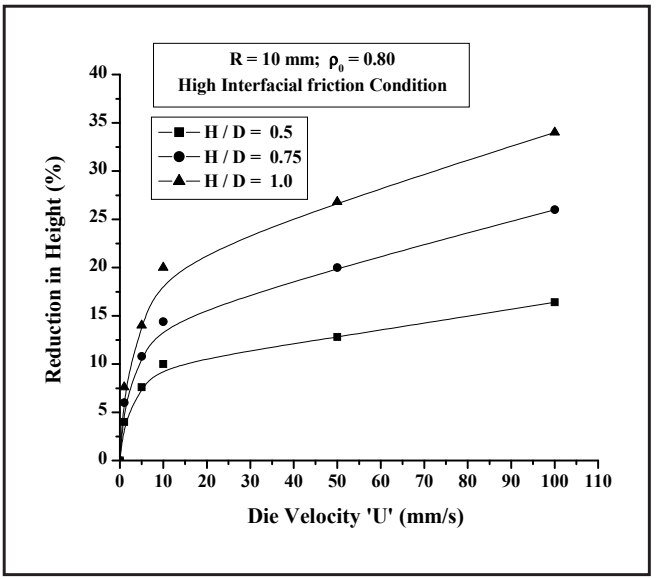

Figure 3.36: Variation of Height Reduction with Die Velocity during Closed-Die Sinter-Forging of Double-Hub Flange Component.

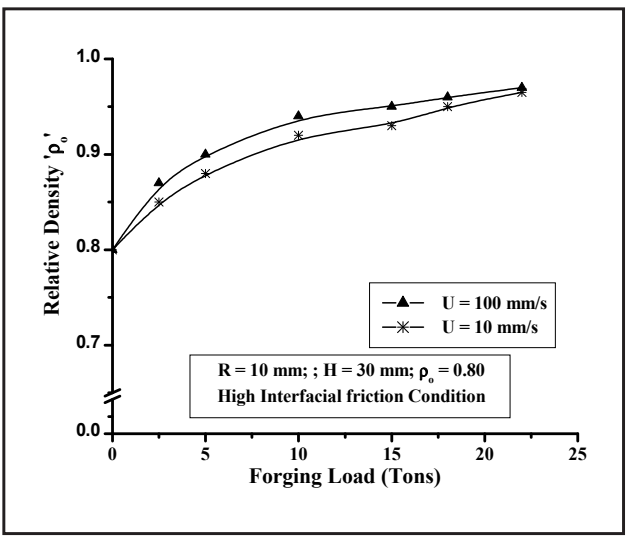

Figure 3.37: Variation of Relative Density with Forging Load during Closed-Die Sinter-Forging of Double-Hub Flange Component.

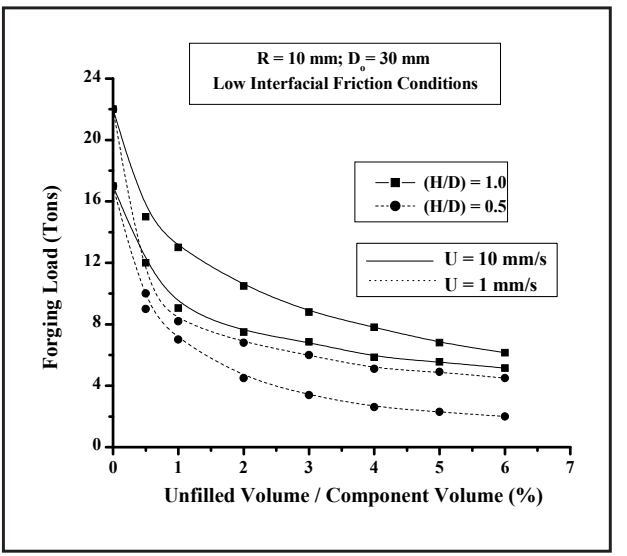

Figure 3.38: Variation of Forging Load with Ratio of Unfilled Die Volume to Components' Actual Volume during Closed-Die Sinter-Forging of Double-Hub Flange Component.

3.3.6 Measurements during Rotary Sinter-Forging of Cylindrical Preforms

The rotary sinter-forging of cylindrical preform with known initial relative density of 0.80 has been performed using an upper conical die with skew contact angle of 5^0, 10^0 and 15^0. Preform was slowly deformed between an upper conical die having orbital motion with an inclined rotating axis, and the lower die moving upwards. The effect of skew contact angle of the conical upper die on the flow behavior of the material and, forging load were critically investigated. Figure 3.39 shows the variation of height reduction with increment of diameter of cylindrical preform the relationship is found to be almost linear in nature. It is clearly evident from the figure that as the height of the preform reduces with the axial movement of the lower die and orbital movement of the upper conical die, the diameter of the preform increases. The changes in relative density and percent reduction in the height along with the corresponding angular velocity during rotary sinter-forging has been recorded and is displayed graphically in figure 3.40. The

relative density of preform is found to increase with decrease in angular velocity of upper conical die, which is attributed due to the predominant dynamic effects exhibited during the rotary sinter-forging process.

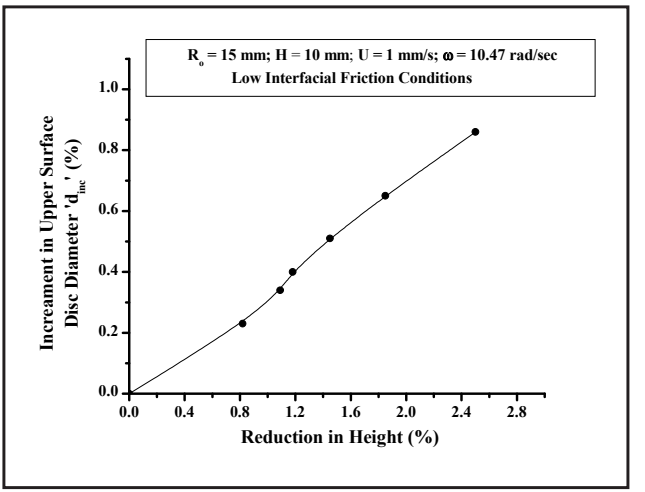

Figure 3.39: Variation of height reduction with upper surface disc diameter during the rotary sinter-forging of cylindrical preforms.

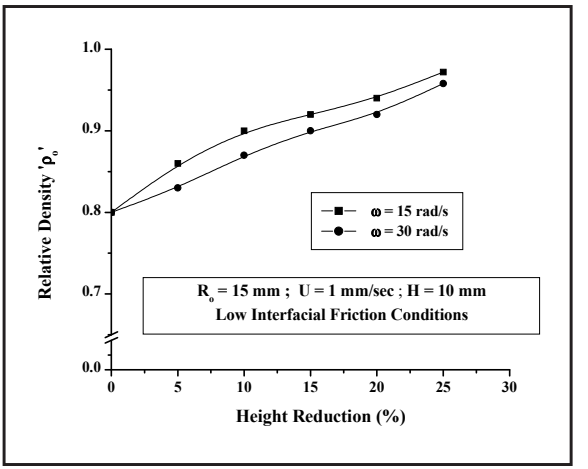

Figure 3.40: Variation of Relative Density with height reduction during the rotary sinter-forging of cylindrical preforms.

The present experimental study has revealed that the deformation characteristics on preform relative density, formability, change in dimensions, forging load and die velocity etc. are related to each other in a complex manner during sinter-forging processes.

CHAPTER 4

PLASTICITY MODEL & FINITE ELEMENT FORMULATION FOR SINTERED MATERIALS

The plastic deformation behavior of sintered materials and preforms, during mechanical processing is totally different as compared to that of the conventional wrought materials. Various theories and methods of analysis been established and successfully implemented for analyzing the problems in conventional metal forming processes, but the same cannot be applied directly to powder metallurgy processes. This is attributed mainly, because of the presence of porosity causing the changes in volume during the deformation of sintered materials. During upsetting or forging of sintered materials, where very large amount of deformation and shear is involved, the mode of deformation is the function of both density and the hydrostatic stress *Jha A.K. et. al* [139]. Preforms with higher relative density yields at higher stress values, and align in the direction perpendicular to that of forging. The application of compressive hydrostatic stress, leads the pores to collapse and increase in relative density of the preform, whereas tensile hydrostatic stress makes the pores to grow, and decrease the relative density of the preform. Even pure hydrostatic stress can lead to yield a metal powder preform, since the yield surface is closed to the hydrostatic stress axis. *Lawley A* and *Chin Gilbert Y.* [140]. The current chapter deals with important characteristics during plastic deformation of sintered materials e.g. yield criterion, densification rules, associated finite element formulations, die-preform interfacial friction conditions, associated compatibility conditions and constitutive relations.

4.1 PLASTICITY MODEL

4.1.1 Yield Criterion & Compatibility Equations

In characterizing the mechanical response of porous materials, deriving yield function is fundamental to the development of plasticity theory and process modeling of sintered metal powder preforms working operations. A yield criterion is a law defining the limit of plasticity under any possible combination of stresses and is expressed as:

$$f(\sigma_{ij}) = C \text{ (a constant)} \tag{4.1}$$

where, $f(\sigma_{ij})$ is function of stresses called yield function

For isotropic materials, plastic yielding of a material depends only on the magnitude of three principal stresses and not on their direction. Thus, any yield criterion may be expressed in the form as:

$$f(I_1, I_2, I_3) = C \tag{4.2}$$

From the literature survey, it is well-known that the yielding of conventional wrought material is unaffected by moderate hydrostatic stress, but depends only on the principal components of the deviatoric stress tensor resulting in the form of:

$$\sigma_{ij}' = \sigma_{ij} - \delta_{ij}\sigma_m \tag{4.3}$$

where,

δ_{ij} $(= 0, \text{if } i \neq j)$, & $(=1, \text{if } i = j)$

For the analysis of metal deformation, Von Mises criterion is found to be in extensive use stating that yielding occurs when 'J_2' reaches a critical value. For fully dense material, the onset of yielding is given by:

$$\frac{1}{2}\sigma'_{ij}\epsilon'_{ij} = k \text{ (a constant)} \tag{4.4}$$

where,

$$\epsilon'_{ij} = \left(\frac{1+\nu}{E}\right)\sigma'_{ij} \quad (4.5)$$

resulting the yield function in the form as:

$$Y^2_o = A\, J_2' \quad (4.6)$$

But this Von Mises' yield function cannot be used for the development of the plasticity theory for porous powder metallurgy or sintered materials. In case of sintered materials, the yielding is influenced not only by deviatoric stress component but also the hydrostatic stress due to presence of porosity. Thus, it is proposed that homogeneous and isotropic sintered porous materials begin to yield, when the apparent total distortion energy reaches a critical value. It is also approximated that up to the yield point, there is no permanent change in the density (relative density) of the sintered materials, as well as the behavior of such sintered materials is considered to be linear. Densification only begins upon yielding. Deformation behavior being linear up to the yield point, Von Mises criterion may be extended, saying that the yielding occurs when the distortion energy reaches a constant value, which can be expressed as:

$$\frac{1}{2}\sigma'_{ij}\epsilon'_{ij} + \frac{1}{2}\sigma_m \epsilon_v = k \quad (4.7)$$

The above expression can be rewritten using equations 4.4, 4.5 & 4.7 as:

$$2(1+\nu)J_2' + \left(\frac{1-2\nu}{3}\right) J_1' = Y_R^2 \quad (4.8)$$

which represents the yield function for sintered materials and it can be observed that it depends on both deviatoric as well as the hydrostatic stresses. Thus resulting in the form as shown, and been considered by many researchers *Green R. J.* and *Downey C. L. et. al.* [50-51] as:

$$f(\sigma_{ij}) = A\, J_2' + B\, J_1^2 = Y_R^2 \quad (4.9)$$

where,

Y_R = Apparent yield stress of the sintered materials

$A = 2(1+\nu)$

$B = \frac{1-2\nu}{3}$

Alternatively, equation 4.9 may be expressed as [as B = 1 – (A/3)]:

$$f(\sigma_{ij}) = A[\tfrac{1}{6}[(\sigma_x - \sigma_y)^2 + (\sigma_y - \sigma_z)^2 + (\sigma_z - \sigma_x)^2] + [(\tau_{xy})^2 + (\tau_{yz})^2 + (\tau_{zx})^2]] + (1 - \tfrac{A}{3})(\sigma_x + \sigma_y + \sigma_z)^2 \quad (4.10)$$

It may be noted that equation 4.10 can be converted to Von Mises' criterion by assuming fully dense incompressible material, where $\nu = 0.5$ leading to A = 3 & B = 0.

4.1.2 Densification Behavior

The apparent yield stress depends on the property of the wrought materials and the relative density 'ρ_o', which is the ratio of the volume of wrought materials to the volume of the sintered materials as proposed by *Zhdanovich* [141] may be expressed as:

$$\nu = 0.5(\rho_o)^n \quad (4.11)$$

where, n = 2 for sintered components

The above relation as expressed in equation 4.11 was also verified by *Kuhn* [142] experimentally for Aluminum and other ferrous metal powders and was used subsequently in the modeling of powder metallurgy deformation processes. Thus, the above yield function for sintered materials may also be expressed as:

$$2(1+\upsilon)J_2' + \left(\frac{1-2\upsilon}{3}\right)J_1^2 = Y_R^2 = \eta Y_0^2 \quad (4.12)$$

and expressed in terms of ρ_o is:

$$\left(2+\rho_o{}^2\right)J_2' + \frac{1-R^2}{3}J_1^2 = Y_R^2 = \eta Y_0^2 \quad (4.13)$$

Where 'A' and 'B' in terms of relative density are given as:

$A = 2 + \rho_o{}^2$ & $B = \frac{1-\rho_o{}^2}{3}$

Substituting, $\eta = 2\rho_o{}^2 - 1$, the expression for yield function may be expressed as:

$$f(\sigma_{ij}) = A J_2' + B J_1^2 = Y_R^2 = \eta Y_o^2 \quad (4.14)$$

The constitutive relation using the yield function as mentioned in expression 4.10, and its associated flow rules are expressed by,

$$\dot{\epsilon}_{ij} = \frac{\partial f}{\partial \sigma_{ij}} \dot{\lambda} \quad (4.15)$$

further,

$$\dot{\epsilon}_{ij} = \dot{\lambda}[A\, \sigma_{ij}' + \frac{2(3-A)}{3} \delta_{ij} J_1] \quad (4.16)$$

hence the strain rate in terms of effective strain rate and the yield stress of the sintered materials may be expressed as:

$$\dot{\epsilon}_{ij} = \frac{\dot{\overline{\epsilon_R}}}{2Y_R}[A\, \sigma_{ij}' + \frac{2(3-A)}{3} \delta_{ij} J_1] \quad (4.17)$$

where,

$\dot{\overline{\epsilon_R}}$ is the effective strain rate for the sintered materials and expressed as:

$$(\dot{\overline{\epsilon_R}})^2 = \frac{1}{A} \left[\frac{2}{3} \{[(\dot{\epsilon}_x - \dot{\epsilon}_y)^2 + (\dot{\epsilon}_y - \dot{\epsilon}_z)^2 + (\dot{\epsilon}_z - \dot{\epsilon}_x)^2\} + [\dot{\gamma}^2_{xy} + \dot{\gamma}^2_{yz} + \dot{\gamma}^2_{zx}] + \frac{1}{3(3-A)} \dot{\epsilon} \right. \quad (4.18)$$

where,

$\dot{\lambda}$ is the proportionality factor in the flow rule given as:

$$\dot{\lambda} = \frac{\dot{\overline{\epsilon_R}}}{2Y_R} \quad (4.19)$$

Also, in general the expression for stresses induced in the sintered materials is expressed as:

$$\sigma_{ij} = \frac{Y_R}{\dot{\epsilon}_R}\left[\frac{2}{A}\dot{\epsilon}_{ij} + \frac{1}{3(3-A)}\delta_{ij}\dot{\epsilon}_v\right] \quad (4.20)$$

Expressions 4.18 and 4.20 are used to determine the effective strain rate and stress for the sintered materials.

The change in relative density in terms of volumetric strain can be expressed as:

$$\rho_o = \rho_{io} e^{(-\Delta\epsilon_v)} \quad (4.21)$$

Where ρi_o is the initial relative density of sintered preform.

4.2 FINITE ELEMENT FORMULATION

For an accurate finite element prediction and its ability to account for large plastic deformations, complex tool-preform interactions, boundary conditions and the material evolution during metal forming analysis, the formulations derived should satisfy the needed conditions. Development of numerical procedures built on the flow formulations, application of finite element method to metal forming processes were mainly in the analysis of compression and other simple deformation processes *Kobayashi. et.al.* [22]. The deformation process for sintered material is assumed to obey the yield criterion, its associated flow rule related with the boundary value problem, satisfying both the stress and velocity field solutions in the equilibrium equations, the constitutive equations in the domain, and finally the given velocity and tractions on the boundary.

4.2.1 Basis for Finite-Element Formulation

The basis of finite element analysis of sintered metal forming is a plasticity theory, because the practical forming process involves very large amounts of plastic deformation based on the infinitesimal theory.

The assumptions made during formulating and developing FE model includes:

- The elastic portion of the deformation is neglected

- The normality of plastic strain rates to the yield surface holding anistrophy during deformation is negligible
- The thermal properties of porous materials are independent of temperatures

The variational form, minimum work rate principle, as a basis for finite-element discretization can be expressed mathematically in functional form as:

$$\pi = \int_V \overline{\sigma}\dot{\epsilon} dV - \int_s T\mathbf{u} dS - \int_{S_i} f\mathbf{u} dS = 0 \quad (4.22)$$

$$\delta\pi = \int_V \overline{\sigma}\delta\dot{\epsilon}\, dV - \int_s T\delta\mathbf{u} dS - \int_{S_i} f\delta\mathbf{u} dS = 0 \quad (4.23)$$

where,

$'\delta'$ denote variations, i.e. $'\delta u'$ is the variation of virtual velocities, $\delta\dot{\epsilon}$ is the variation of strain rate, 'T' is the traction prescribed on surface and 'f' is the frictional stress on the tool-preform interface 'S_i'.

It can be shown that $\overline{\sigma}\,\delta\dot{\epsilon} = Y_R\,\delta\dot{\bar{\varepsilon}}_R$ and thus, equation 4.23 can be expressed as:

$$\delta\pi = \int_V Y_R\,\delta\dot{\bar{\varepsilon}}_R\, dV - \int_s T\,\delta\mathbf{u}\, dS - \int_{S_i} f\,\delta\mathbf{u}\, dS = 0 \quad (4.24)$$

4.2.2 Numerical Analysis Procedure

The finite element method procedure outlined below was executed in computer program by generating an assumed solution velocity, evaluating the elemental stiffness matrix for the velocity term and imposing velocity conditions over all the elements defined in the preform. Finally assembling the element stiffness matrix to form a global stiffness equation and solving it using Newton Raphson iteration method until the velocity solution converged. When the converged velocity solution is obtained, the geometry of the preform is updated using the velocity of nodes during a time increment and this process repeated until the desired degree of deformation is achieved. The flowchart is shown in figure 4.1.

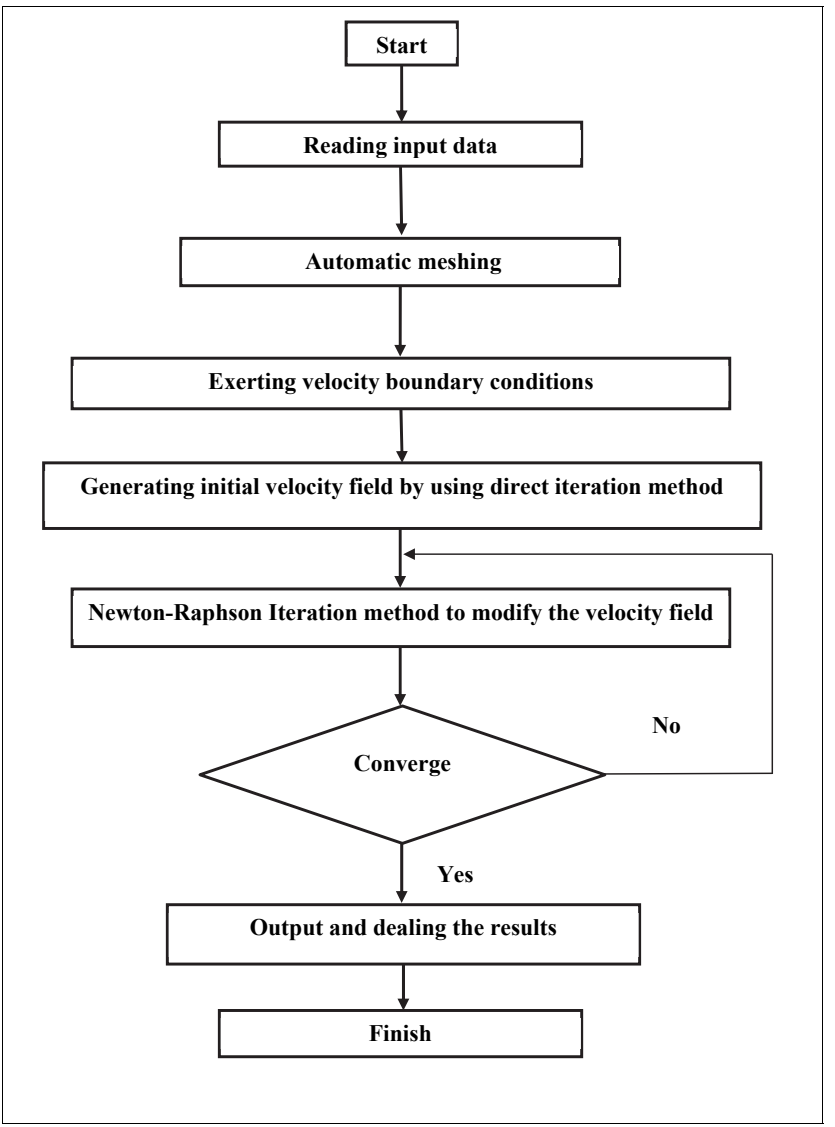

Figure 4.1: Flow Chart of FEM Process.

4.2.2.1 Case - 1 (Axi-Symmetric Isoparametric Quadrilateral Element)

The elements used for discretization is an axisymmetric isoparametric quadrilateral element with bilinear shape function as shown in figure 4.2 for the two-dimensional deformations.

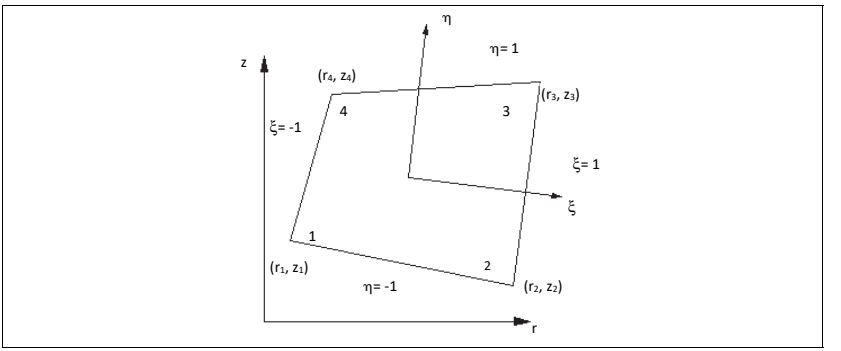

Figure 4.2: Quadrilateral Element and Natural Coordinate System.

The elemental velocity field is approximated by shape function in terms of nodal velocity as:

$$\mathbf{u} = \begin{Bmatrix} u_r \\ u_z \end{Bmatrix} = \mathbf{N^T v} \tag{4.25}$$

Where 'v' is the velocity vector of nodal-point value and '**N**' is the shape function matrix. Appling differentiation to equation 4.25, the strain rate vector in term of local nodal velocities can be written as:

$$\dot{\varepsilon} = \begin{Bmatrix} \dot{\varepsilon}_r \\ \dot{\varepsilon}_z \\ \dot{\varepsilon}_\theta \\ \dot{\gamma}_{rz} \end{Bmatrix} = \begin{bmatrix} \partial/\partial r & 0 \\ 0 & \partial/\partial z \\ 1/r & 0 \\ \partial/\partial z & \partial/\partial r \end{bmatrix} \begin{Bmatrix} u_r \\ u_z \end{Bmatrix} = \mathbf{Bv} \tag{4.26}$$

The matrix '**N**' and '**B**' have been defined for a quadrilateral element as:

$$\mathbf{N^T}=\begin{bmatrix} q_1 & 0 & q_2 & 0 & q_3 & 0 & q_4 & 0 \\ 0 & q_1 & 0 & q_2 & 0 & q_3 & 0 & q_4 \end{bmatrix} \quad \text{with} \tag{4.27}$$

$$q_1 = \frac{1}{4}(1-\xi)(1-\eta), \qquad q_2 = \frac{1}{4}(1+\xi)(1-\eta) \tag{4.28a}$$

$$q_3 = \frac{1}{4}(1+\xi)(1+\eta), \qquad q_4 = \frac{1}{4}(1-\xi)(1+\eta) \tag{4.28b}$$

$$\mathbf{B} = \begin{bmatrix} X_1 & 0 & X_2 & 0 & X_3 & 0 & X_4 & 0 \\ 0 & Y_1 & 0 & Y_2 & 0 & Y_3 & 0 & Y_4 \\ P_1 & 0 & P_2 & 0 & P_3 & 0 & P_4 & 0 \\ Y_1 & X_1 & Y_2 & X_2 & Y_3 & X_3 & Y_4 & X_4 \end{bmatrix} \tag{4.29}$$

where,

$$\begin{Bmatrix} X_1 \\ X_2 \\ X_3 \\ X_4 \end{Bmatrix} = \frac{1}{8|J|} \begin{Bmatrix} z_{24} - z_{34}\xi - z_{23}\eta \\ -z_{13} + z_{34}\xi + z_{14}\eta \\ -z_{24} + z_{12}\xi - z_{23}\eta \\ z_{13} - z_{12}\xi + z_{23}\eta \end{Bmatrix} \tag{4.30}$$

$$\begin{Bmatrix} Y_1 \\ Y_2 \\ Y_3 \\ Y_4 \end{Bmatrix} = \frac{1}{8|J|} \begin{Bmatrix} -r_{24} + r_{34}\xi + r_{23}\eta \\ r_{13} - r_{34}\xi - r_{14}\eta \\ r_{24} - r_{12}\xi + r_{23}\eta \\ -r_{13} + r_{12}\xi - r_{23}\eta \end{Bmatrix} \tag{4.31}$$

$$z_{ij} = z_i - z_j, \qquad r_{ij} = r_i - r_j$$

$$P_i = \frac{q_i}{r} = \frac{q_i}{\sum_\alpha (q_\alpha r_\alpha)} \tag{4.32}$$

where 'α' is the node number.

4.2.2.2 Case – 2 (3-D Four Node Tetrahedral Element)

The elements used for discretization is a three dimensional four-node tetrahedral element for the three-dimensional deformations as shown in figure 4.3. Using the master element with x as ξ, y as η, and z as ζ, the shape functions may be defined as:

$$N_1 = \xi \qquad N_2 = \eta \qquad N_3 = \zeta \qquad N_4 = 1 - \xi - \eta - \zeta \tag{4.33}$$

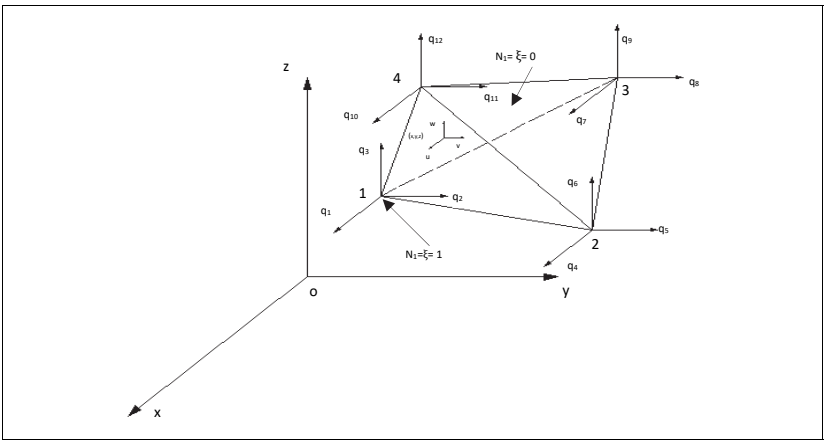

Figure 4.3: Tetrahedral Element.

The elemental velocity field within an element is approximated by shape function in terms of nodal velocity as:

$$u = \begin{Bmatrix} u_x \\ u_y \\ u_z \end{Bmatrix} = \mathbf{N^T v} \tag{4.34}$$

where,

$$\mathbf{N^T} = \begin{bmatrix} q_1 & 0 & 0 & q_2 & 0 & 0 & q_3 & 0 & 0 & q_4 & 0 & 0 \\ 0 & q_1 & 0 & 0 & q_2 & 0 & 0 & q_3 & 0 & 0 & q_4 & 0 \\ 0 & 0 & q_1 & 0 & 0 & q_2 & 0 & 0 & q_3 & 0 & 0 & q_4 \end{bmatrix} \tag{4.35}$$

Appling differentiation between x, y, and z and ξ ,η, and ζ and the assumed elemental velocity field, the strain rate vector can be expressed as:

$$\dot{\epsilon}^{T} = \{\dot{\epsilon}_x, \dot{\epsilon}_y, \dot{\epsilon}_z, \dot{\gamma}_{xy}, \dot{\gamma}_{yz}, \dot{\gamma}_{zx}\} \tag{4.36}$$

$$\dot{\epsilon} = \mathbf{Bv} \tag{4.37}$$

where, '**B**' is a (6 X 12) matrix given by taking the space derivatives of velocities,

$$\mathbf{B} = \begin{bmatrix} A_{11} & 0 & 0 & A_{12} & 0 & 0 & A_{13} & 0 & 0 & -\widetilde{A}_1 & 0 & 0 \\ 0 & A_{21} & 0 & 0 & A_{22} & 0 & 0 & A_{23} & 0 & 0 & -\widetilde{A}_2 & 0 \\ 0 & 0 & A_{31} & 0 & 0 & A_{32} & 0 & 0 & A_{33} & 0 & 0 & -\widetilde{A}_3 \\ 0 & A_{31} & A_{21} & 0 & A_{32} & A_{22} & 0 & A_{33} & A_{23} & 0 & -\widetilde{A}_3 & -\widetilde{A}_2 \\ A_{31} & 0 & A_{11} & A_{32} & 0 & A_{12} & A_{33} & 0 & A_{13} & -\widetilde{A}_3 & 0 & -\widetilde{A}_1 \\ A_{21} & A_{11} & 0 & A_{22} & A_{12} & 0 & A_{23} & A_{13} & 0 & -\widetilde{A}_2 & -\widetilde{A}_1 & 0 \end{bmatrix} \tag{4.38}$$

where, $\widetilde{A}_1 = A_{11} + A_{12} + A_{13}$, $\widetilde{A}_2 = A_{21} + A_{22} + A_{23}$, and $\widetilde{A}_3 = A_{31} + A_{32} + A_{33}$ and all the terms of '**B**' are constants.

Substituting equation 4.26 into equation 4.18, one get:

$$(\dot{\bar{\varepsilon}}_R)^2 = \dot{\boldsymbol{\varepsilon}}^{T}\mathbf{D}\dot{\boldsymbol{\varepsilon}} = \mathbf{v}^{T}\mathbf{B}^{T}\mathbf{DBv} = \mathbf{v}^{T}\mathbf{Pv} \tag{4.39}$$

where, $\mathbf{P} = \mathbf{B}^{T}\mathbf{DB}$

and the variation of effective strain rate $\dot{\bar{\varepsilon}}_R$ may be expressed as:

$$\delta\dot{\bar{\varepsilon}}_R = \frac{1}{\dot{\bar{\varepsilon}}_R}\delta v^{T}\mathbf{P}v \tag{4.40}$$

Substituting equation 4.25 & 4.40 into equation 4.22 at the elemental level and assembling the element equations with global constraints, one get:

$$\sum_{j}^{N} \delta\mathbf{v}^{T}\left[\int_{V_j}\frac{Y_R}{\dot{\bar{\varepsilon}}_R}\mathbf{P}v\,dV - \int_{S}T\mathbf{u}\,dS - \int_{S_i} f\mathbf{u}\,dS\right]_{(j)} = 0 \tag{4.41}$$

where, (j) indicates the j^{th} element and 'N' the total number of elements. As the variation δv is arbitrary, equation 4.41 results into the stiffness equations.

The inversion of the flow rule equation 4.15 can be expressed as:

$$\boldsymbol{\sigma} = \frac{Y_R}{\dot{\bar{\varepsilon}}_R}\mathbf{D}\dot{\boldsymbol{\varepsilon}} \tag{4.42}$$

where, for the axisymmetric case, 'D' may be expressed as:

$$\mathbf{D} = \begin{bmatrix} \frac{4-A}{A(3-A)} & \frac{A-2}{A(3-A)} & \frac{A-2}{A(3-A)} & 0 \\ & \frac{4-A}{A(3-A)} & \frac{A-2}{A(3-A)} & 0 \\ \text{Sym} & & \frac{4-A}{A(3-A)} & 0 \\ & & & \frac{1}{A} \end{bmatrix} \tag{4.43}$$

where, the stress and strain-rate vector are defined as:

$\boldsymbol{\sigma}^T = \{\sigma_r, \sigma_z, \sigma_\theta, \sigma_{rz}\}$ & $\dot{\boldsymbol{\varepsilon}}^T = \{\dot{\varepsilon}_r, \dot{\varepsilon}_z, \dot{\varepsilon}_\theta, \dot{\gamma}_{rz}\}$ respectively.

Then, from the requirement that $\boldsymbol{\sigma}^T\dot{\boldsymbol{\varepsilon}} = Y_R\dot{\bar{\varepsilon}}_R$, one get:

$(\dot{\bar{\varepsilon}}_R)^2 = \dot{\boldsymbol{\varepsilon}}^T\mathbf{D}\dot{\boldsymbol{\varepsilon}}$ & $\mathbf{P} = \mathbf{B}^T\mathbf{D}\mathbf{B}$

4.2.3 Interfacial Friction Conditions

Friction conditions at the die-preform interface is a mixed type and play a major role in influencing various deformation characteristics like metal flow, stress acting on the dies, load and energy requirements etc.

On the surface S_i the die and preform interface, the interfacial friction in terms of nodal point forces can be representation as:

$$f_s = \sum_{j=1}^{N}\int_{S_i} f\mathbf{u}dS \tag{4.44}$$

where, 'f_s' is the load vector of tangential nodal point forces on surface S_i.

The interfacial frictional constraint between the die and sintered materials is represented by either a constant frictional shear stress or Coulomb coefficient of friction. Considering constant friction coefficient 'μ', the magnitude of frictional stress 'f_s' which is dependent on the magnitude of relative sliding and the directions opposite to each other, the relationship can be expressed as.

$$f_s = -\mu f_n \frac{\mu_s}{|\mu_s|} \cong -\mu f_n \left[\frac{2}{\pi}\tan^{-1}\frac{\mu_s}{\mu_0}\right] \quad (4.45)$$

'f_n' is the global nodal point force in the normal direction on S_i, 'μ_s' the sliding velocity of the sintered material relative to the die, and 'μ_0' the small positive number compared to 'μ_s'. Finally, for solution to converge, Newton-Raphson iterative method is used to solve the equation 4.41 and the relative density can be upgraded.

The volumetric strain-rate related to the density-rate may be expressed as:

$$\dot{\varepsilon}_v = \mathbf{C^T v} = -\frac{\dot{\rho_o}}{\rho_o} \quad (4.46)$$

where, relative density ρ_o is defined as:

$$\rho_o = \frac{V_b}{V_b + V_v} \quad (4.47)$$

where, V_b being volume of the base metal and V_v as volume of the voids. Thus, the relative density may be expressed as:

$$\rho_o = \rho_{io}\exp(-\int \dot{\varepsilon}_v dt) \cong \rho_{io}(1 - \Delta\varepsilon_v) \quad (4.48)$$

ρ_{io} is the instantaneous relative density and $\Delta\varepsilon_v$ is the change of volumetric strain in one deformation step. Thus, the average density ρ_{ao} is as:

$$\rho_{ao} = \frac{\sum \rho_{io} V_i}{\sum V_i} \quad (4.49)$$

Where ρ_{io} and V_i are the instantaneous relative density and the volume of an element, respectively.

CHAPTER 5

FEM ANALYSIS OF OPEN-DIE SINTER-FORGING OF DIFFERENT GENERIC SHAPED PREFORMS

This chapter deals with finite element simulation of open-die sinter-forging of aluminum metal powder preforms at different deformation speeds. Preforms with three different generic shapes *i.e.* hollow, truncated conical and irregular trapezoidal have been considered under open-die sinter-forging process in all the three sections of the chapter. The idea was to envelope various types of generic shapes of the preforms, which can be added or subtracted during solid modeling to create any complex shaped components.

The influence of die velocity, internal energy dissipations, die loads, final bulged shape of preforms, strains at preform free surfaces, respective strain rates and their interrelationships, have been investigated and displayed graphically. The finite element simulation of sinter-forging of the sintered aluminium preforms was performed using DEFORM^{TM} software and simulation results with corresponding experimental results were compared with respect to each other. DEFORM -2D and 3D based on finite element method, has proven to be accurate and robust in industrial application for more than two decades. The simulation engine is designed to analyze the two-dimensional (2D) and three dimensional (3D) flow of complex metal forming processes with different material models, porous material model for forming PM products, rigid- plastic model used for predicting large deformation material flow.

It includes the provision of providing detailed material properties such as Young's modulus, strain hardening exponent, relative density and strength coefficient, etc., as input to the preprocessor before running solver. Besides material properties, preprocessor also require input of detailed process parameters such as friction coefficient, punch velocity and the dimensions of die, etc. which is the prime necessity to get the accurate

output or simulated results. Self-contact boundary condition with robust remeshing allows a simulation to continue to completion even after a lap or fold has formed (2D, 3D).

5.1 FEM SIMULATION OF OPEN-DIE SINTER-FORGING OF HOLLOW PREFORM

The simulation of cold open-die sinter-forging of sintered hollow aluminium preforms has been performed using DEFORM^{TM}-2D software, which is based on the Lagrangian incremental finite element code.

5.1.1 Finite Element Formulation

As mentioned in previous chapter yield function for porous materials, the yielding is influenced not only by deviatoric stress component but also the hydrostatic stress. And in general, considering that the material to be isotropic, and that the deformation does not produce anisotropy, the yield function for porous materials including both the first invariant of the stress tensor and the second invariant of the deviatoric stress tensor can be represented as mentioned in equation 4.14.

Using the above yield function flow rules can be used as mentioned in equation 4.15, and corresponding effective stress and strain rates can be evaluated using equations 4.17 and 4.18 respectively.

Further, for numerical simulation of sintered forged component starts with the following variational form expressed as

$$\delta\pi = \int_V Y_R \, \delta\dot{\bar{\varepsilon}}_R \, dV - \int_{S_f} f \, \delta u \, dS = 0 \qquad (5.1)$$

Where V is the control volume of the porous body and δ denoted variation.

5.1.2 Discretization

The solution of above equation by the finite element method requires discretization of this control volume by number of elements linked through nodes. The element used for discretization is 2D QUAD Axi-symmetry isoparametric element, with bilinear shape function for two dimensional and axisymmetric deformations and for three dimensional cases four-node 3D Tetrahedral elements been used for meshing three dimensional deformations. The elemental velocity field, strain rate vector, and both 'N' and 'B' matrix been derived and shown in equation 4.26-4.29 and 4.33-4.39 respectively. During forging process the deformations are usually very large, as a result large strains distort the initial mesh in such a degree that a new mesh i.e. remeshing is necessary in order to continue the simulation. The selected elements got the capability of adapting the remeshing functionality. The axi symmetric model of the preform, been modeled to take the advantage of axi-symmetric condition.

5.1.3 Interfacial Friction Model

The interfacial friction conditions and selection of the corresponding friction factors during the analysis of various categories of sinter-forging processes under consideration in the present research work was based on the ring compression tests performed using hollow Aluminium metal powder preforms. The data for the change in outer and inner radii of hollow preform during deformation were recorded and friction factors were obtained, using equation 4.45. Based on the data recorded and after findings, it is modeled in the present simulation.

5.1.4 Material Properties

In finite element modeling, the real material behavior is often categorized to facilitate the analysis. To model the material during computer simulation, the flow stress was assumed to be the function of strain, strain rate and temperature, which is expressed as *Kobayashi. et.al.* [22]:

$$\sigma_o = f(\varepsilon, \dot{\epsilon}, t) \qquad (5.2)$$

In the present case, the stress-strain curve for the sintered aluminium preforms was not available in the library of the software, hence, based on the data recorded a stress-strain relationship of form $\bar{\sigma} = A\bar{\varepsilon}^{m}$ **MPa** was formulated and added to its library. Figure 5.1 shows the flow stress of the sintered aluminium material, which was added to the DEFORM library. The properties of sintered aluminium preform material are given in table 5.1.

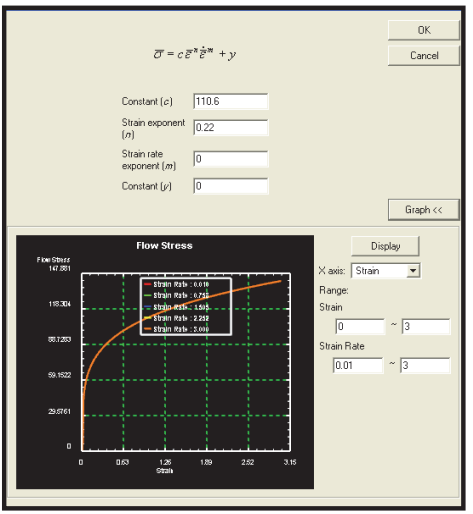

Figure 5.1: Flow Stress Curve of Sintered Aluminium Preform.

TABLE 5.1: Material Property of Sintered Aluminium Preform.

Sl. No.	Material Property	Value
1.	Yield tensile strength	6.25 MPa
2.	Ultimate tensile strength	18 MPa
4.	Initial density	2×10^{3} Kg/m^{3}
5.	Stress-strain relationship	$\bar{\sigma}=110.6\,\bar{\varepsilon}^{0.22}$MPa

5.1.4 Computational Conditions

The geometry of the die platens were generated in DEFORM software and were modeled as rigid, parallel and flat bodies with plastic preform placed in between them. The geometry of preforms were generated using CATIA V5.0 software using part design module/workbench and data was imported to DEFORM software in form of STL files. The three different compacts with the required dimensions, i.e. outer radius 'r_o' equal to 12 mm, inner radius 'r_i' equal to 4.0, 6.0, 8.0 and 10.0 mm (with shape complexity factor C_p 3.0, 2.0, 1.5 and 1.2, respectively) and height 'H' equal to 10 were modeled. Effective coefficient of interfacial friction was considered, *i.e.* 0.3 for lubricated frictional conditions respectively as shown in figure 5.2. The entire model is meshed with 2D Quad Axi-symmetry isoparametric element. Total number of elements used was 2000 with a size aspect ratio of '1' to have uniform mesh as shown in figure 5.3.

The complete upset-forging simulation was performed in 20 steps having time for movement of the die platens in each step equal to 0.2 seconds. The maximum formability of the sintered aluminium hollow preform was found to be about 40 percent at room temperature under lubricated conditions during experiments, which kept as the standard for the design criterion of the upset-forging process during simulation. To illustrate the effect of deformation characteristics and die speed on the magnitude of various power dissipations, die load and strains rates involved during open die forging of hollow preform.

The computational conditions including geometries are as follows:

H = 10 mm, r_o = 12 mm, μ = 0.3 & 0.01, $\rho_i = 2 \times 10^3$ kg/m^3, σ_0 = 6.25 MPa and C_p = 2.0, 1.5 and 1.2 respectively), die velocities (U) = 5, 10, and 100 mm/sec.

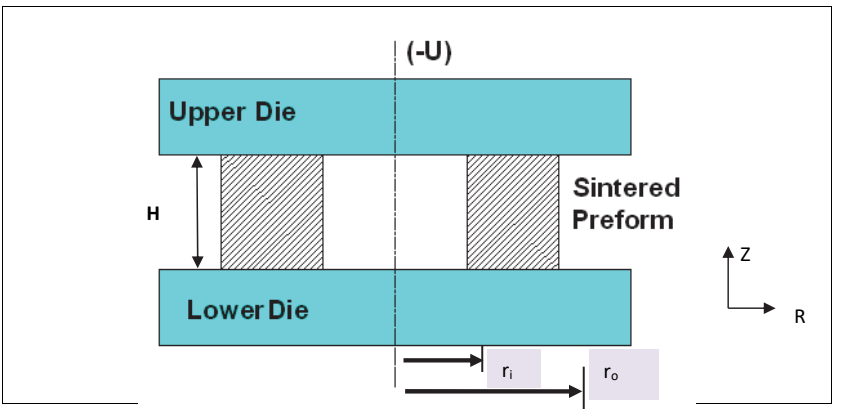

Figure 5.2: Schematic Diagram of Open-Die Sinter-Forging of Hollow Preform.

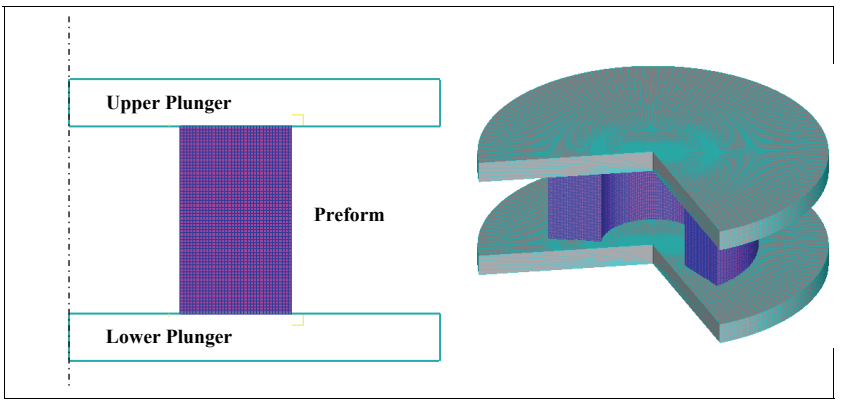

Figure 5.3: Models of Meshed 2D Axi-Symmetric and 3D Hollow Preform.

The variation of effective strain, effective stress, effective strain rate, forging load and internal energy dissipation with sinter-forging time were plotted for three different die velocities. The distribution of total displacement, effective stress, effective strain and velocity vector in form of color codes and contours on the preform surface were obtained. To investigate these distributions over the profile, preform slicing was done and the results were again plotted. The effect of die velocity, preform aspect ratio on energy dissipations, die loads have been investigated and results for the deformation modes have

been compared. The validation of the simulation was done by comparing its results with the experimental results and was found to reasonably agree with each other, which indicated that finite element simulation represents fairly well with the present sinter-forging process.

5.1.5 Parametric Analysis

Figure 5.4 and 5.5 shows the preform profile during various stages of upset-forging. It is evident that as lower die travel increases preform deforms and bulges. The bulging pattern (flow of preform) depends totally on interfacial friction conditions, and the direction of material flow (frictional shear stress) depends upon the position of neutral radius. As shown when the neutral radius lies within inner radius, the material flows throughout in outward direction on the hollow preform, when it lies in between the inner and outer radii of the hollow preform, the flow of material observed flowing inwards for inner region and outwards for outer region.

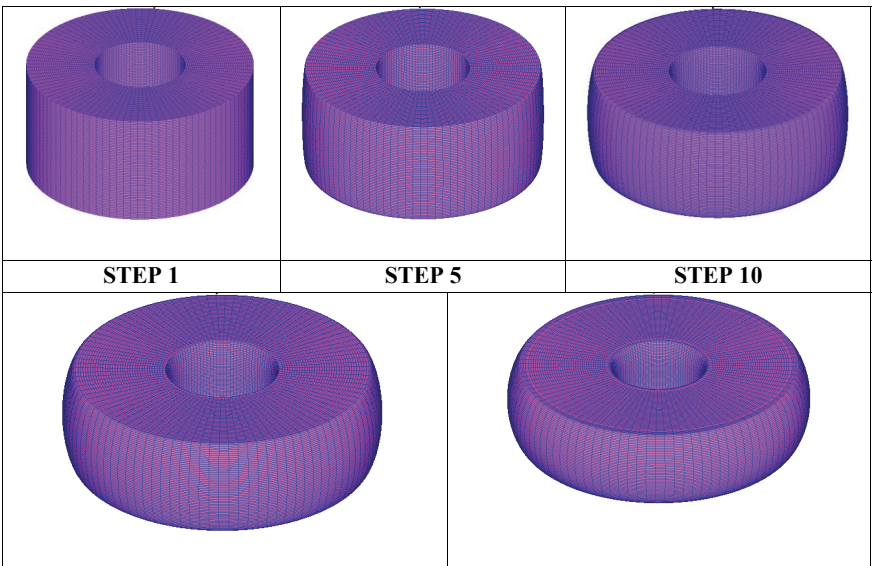

STEP 1	STEP 5	STEP 10
STEP 15	STEP 20	

Figure 5.4 : Sinter-Forging Stages of Hollow Preform with Smaller Inner Diameter.

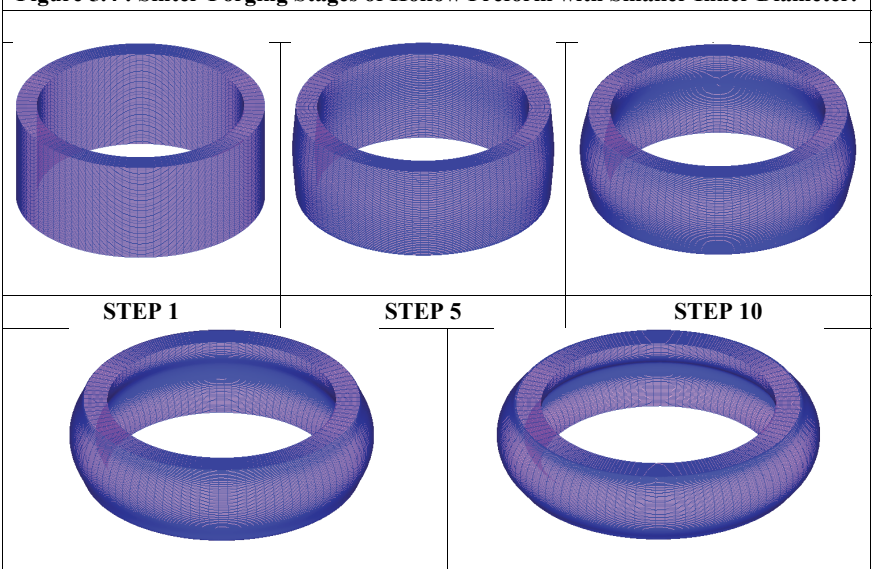

STEP 1	STEP 5	STEP 10
STEP 15	STEP 20	

Figure 5.5 : Sinter-Forging Stages of Hollow Preform with Larger Inner Diameter.

Figure 5.6 shows the distribution of the total displacement of the preform in vertical direction and may be seen that the middle portion of the preform has been displaced maximum.

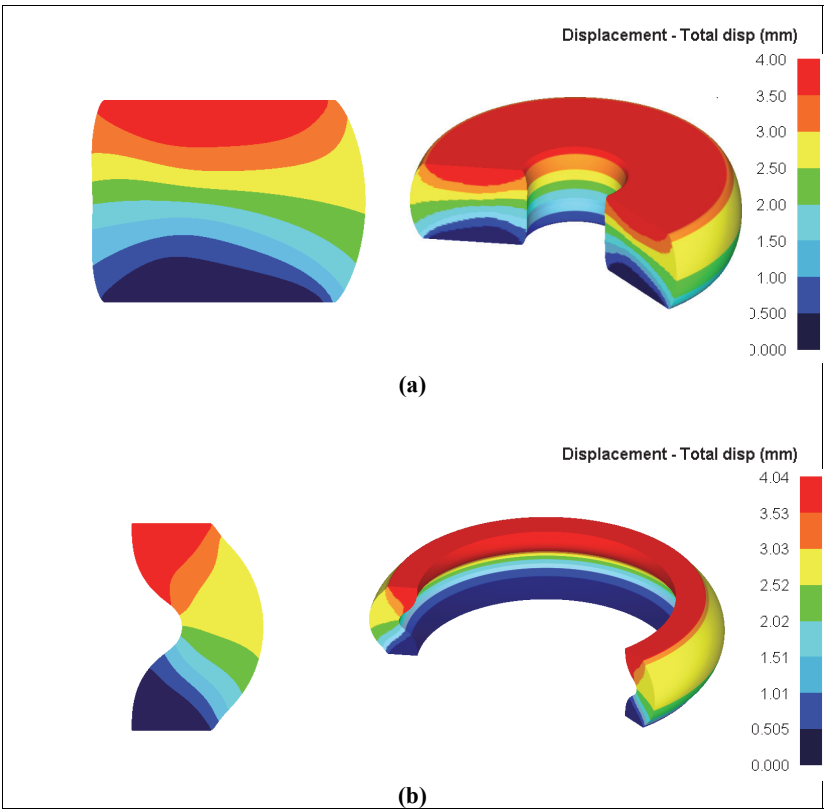

Figure 5.6 (a) & (b): Displacement Profiles during Open-Die Sinter-Forging of Hollow Preform with Smaller and Larger Inner Diameter respectivley.

The distribution of effective strain is shown in figure 5.7 and it is clearly evident that effective strain is in the range of 0.89 to 1.19 mm/mm and 0.7 to 1.05 mm/mm for both preforms, of shape complexity factor C_p 3.0 and 1.2, on the peripheral region of the preform surface.

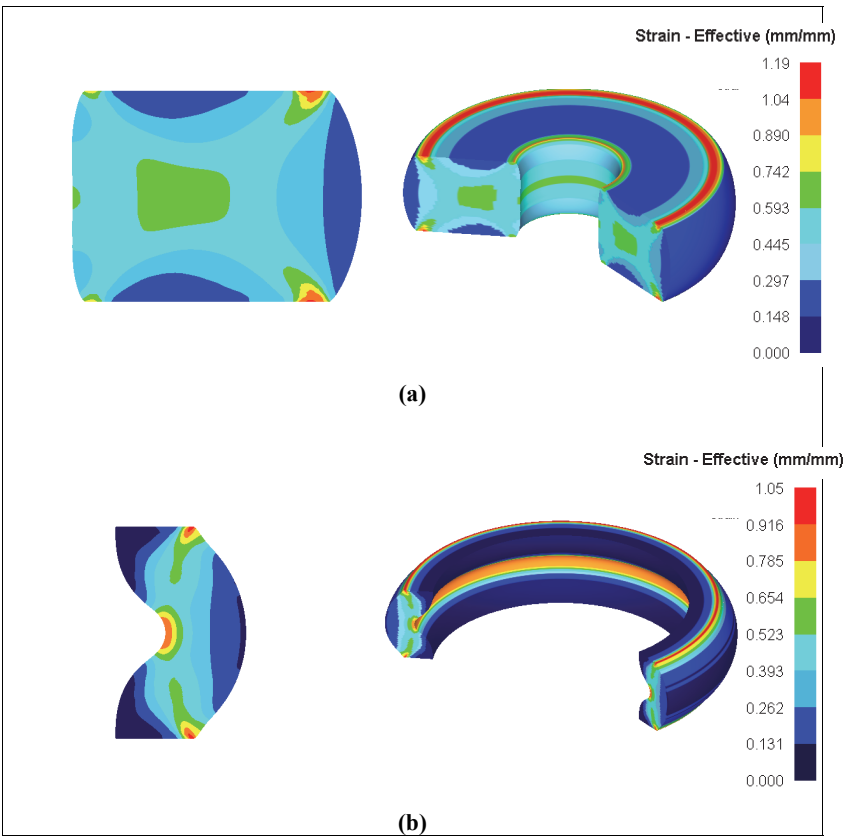

Figure 5.7 (a) & (b): Effective Strain Distribution during Open-Die Sinter-Forging of Hollow Preform with Smaller and Larger Inner Diameter respectivley.

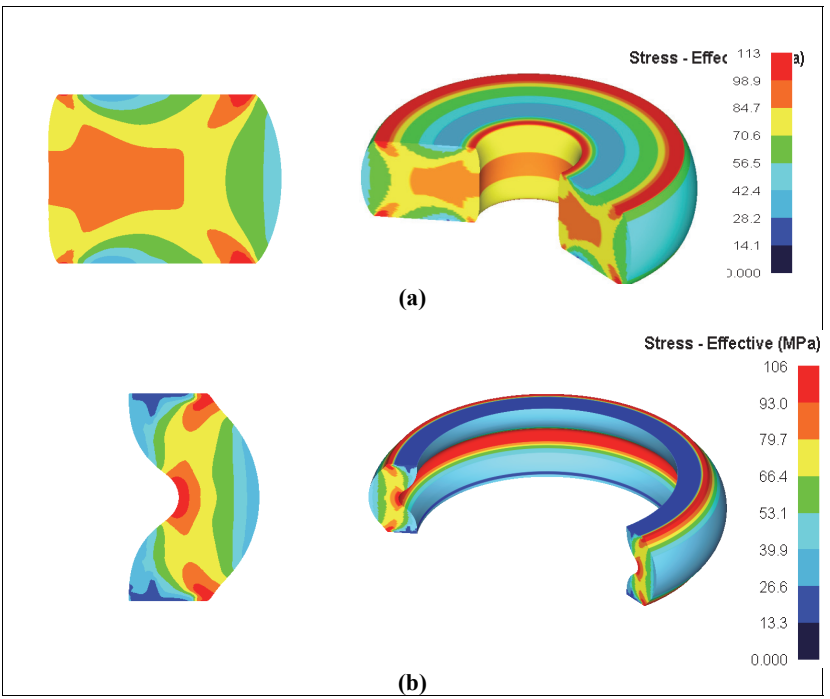

Figure 5.8 (a) & (b) : Effective Stress Distribution during Open-Die Sinter-Forging of Hollow Preform with Smaller and Larger Inner Diameter respectivley.

Figure 5.8 shows the effective stress distribution over the preform surface at the end of upset-forging simulation. The maximum effective stress of the order of 113 MPa and 104 MPa for both larger and smaller inner diameter based on the shape complexity factor C_p 3.0 and 1.2, was found highest at the inner region and least at the outer region. To illustrate the distribution of stress at the various height sections of the preform, the preform was sliced vertically at an angle and the stress distribution in form of contours were also plotted. The high stress concentration was found to be at the edges of the preform and at the inner region resulting the possibility of fracture at these points.

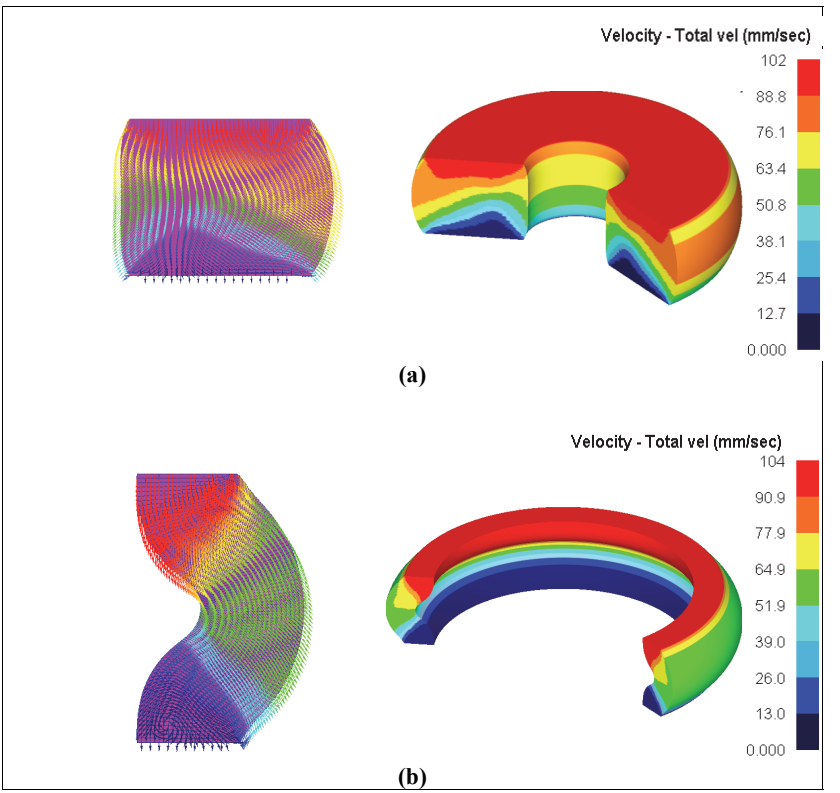

Figure 5.9 (a) & (b) : Velocity Vector Distribution during Open-Die Sinter-Forging of Hollow Preform with Smaller and Larger Inner Diameter respectivley.

Figure 5.9 shows the velocity vector distribution on the preform surface and the maximum velocity in the order of 104 mm/s was found on the vertical surfaces, which are flowing radially outwards, and on the interfacial regions of the preform during upset-forging process. Figure 5.10 and 5.11 shows the variation of the effective strain and effective stress with the percentage in reduction of height and was found to increase exponentially initially and then remain fairly constant at the end of the upset-forging operation. The effective stress was found to be higher for lower die velocity and preforms

with smallest inner radius, whereas the effective strain was found to highest for the highest die velocity with smallest inner radius of the preform.

Figure 5.12 shows the variation of internal energy dissipation with reduction in height at various die velocities. It is evident that internal energy dissipation increases exponentially with die velocity. In addition, it is observed that the internal energy dissipation is higher for preform with higher shape-complexity factor, indicating that solid discs having, same dimensions that of hollow discs requires higher internal energy for deformation.

Figure 5.13 shows the experimental and simulated results of variation of forging load with height reduction for different shape complexity factor, under high interfacial frictional condition at die travel with 100 mm/sec. It is evident that die load increases with increase in height reduction and is higher for higher shape complexity factor.

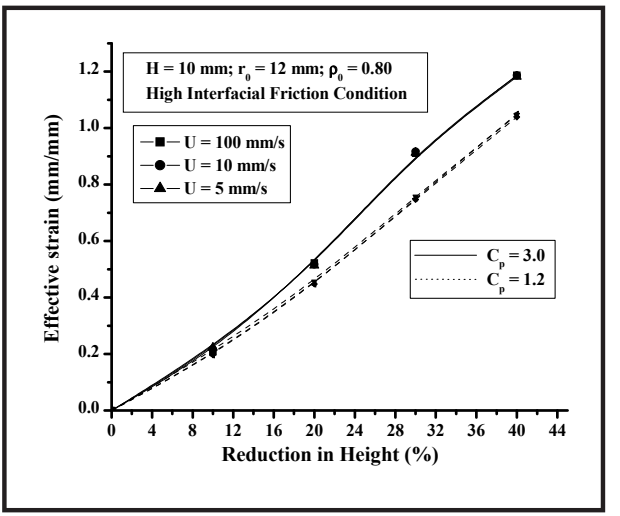

Figure 5.10: Variation of Effective Strain with Height Reduction during Open-Die Sinter-Forging of Hollow Preform.

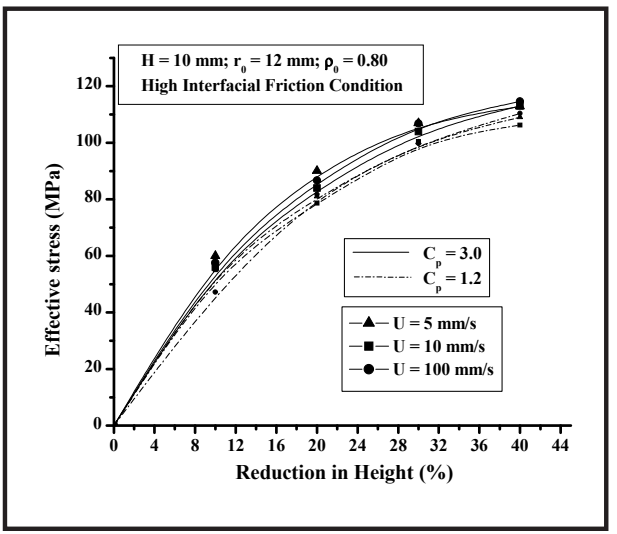

Figure 5.11: Variation of Effective Stress with Height Reduction during Open-Die Sinter-Forging of Hollow Preform.

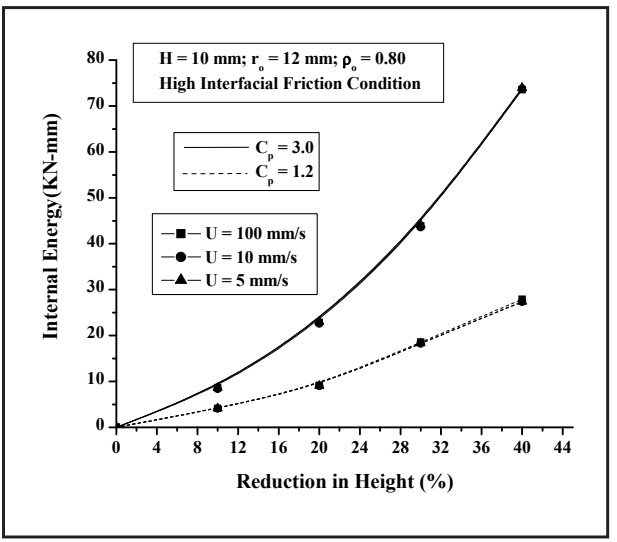

Figure 5.12: Variation of Internal Energy with Height Reduction during Open-Die Sinter-Forging of Hollow Preform.

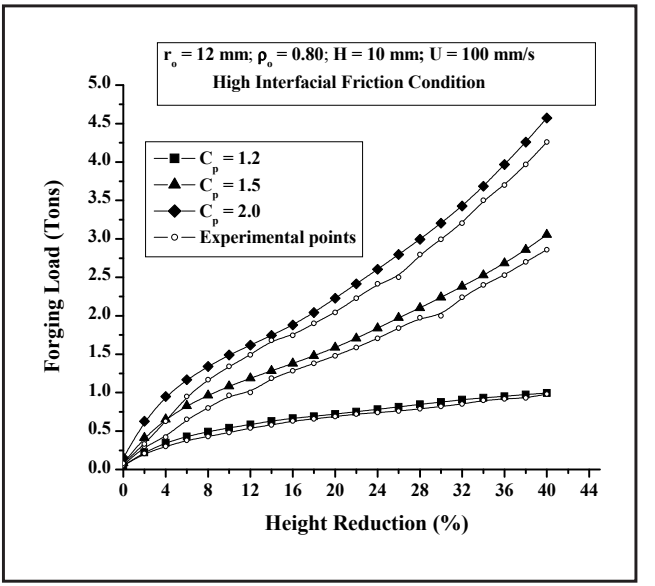

Figure 5.13: Variation of Forging Load with Height Reduction during Open-Die Sinter-Forging of Hollow Preform.

5.2 FEM SIMULATION OF OPEN-DIE SINTER-FORGING OF TRUNCATED CONICAL PREFORM

5.2.1 Computational Conditions

The present analysis deals with computer simulation of upset-forging of sintered aluminium truncated conical preforms. Figure 5.14 shows the upset-forging of truncated conical sintered preform between two perfectly flat, parallel and rigid die platens, where upper die platen is stationary and lower die platen is moving upwards with velocity 'U'. The geometry of the die platens were generated in DEFORM software and were modeled as rigid, parallel and flat bodies with plastic preform placed in between them. The geometry of preforms were generated using CATIA V5.0 software using part design module/workbench and data was imported to DEFORM software in form of STL files.

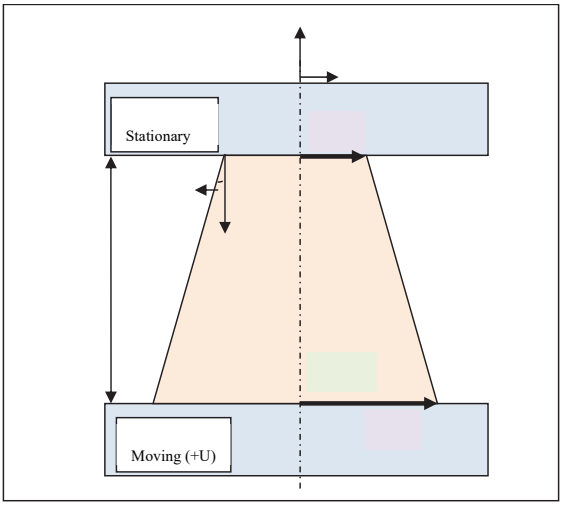

Figure 5.14: Schematic Diagram of Open-Die Sinter-Forging of Truncated Conical Preform.

The three different preform dimensions with height equal to 17 mm, larger radius equal to 12 mm and half cone angle equal to 15^0, 10^0 and 5^0 respectively were considered. Two different values for effective coefficient of interfacial friction were considered, *i.e.* 0.05 and 0.3 for lubricated and unlubricated frictional conditions respectively. Tetrahedral elements with a mesh of 10894 numbers with a size aspect ratio of 2 were used to mesh the truncated conical preforms, in order to better scope the upset-forging process as shown in figure 5.15. The complete upset-forging simulation was performed in 24 steps having time for movement of the die platens in each step equal to 0.311 seconds. The maximum formability of the sintered aluminium preforms was found to be about 45 percent at room temperature under lubricated conditions during experiments, which kept as the standard for the design criterion of the sinter-forging process during simulation. Material property based on data recorded and stress-strain relationship of form $\bar{\sigma}=110.6\,\bar{\varepsilon}^{0.22}$ MPa was formulated i.e. and added to its library.

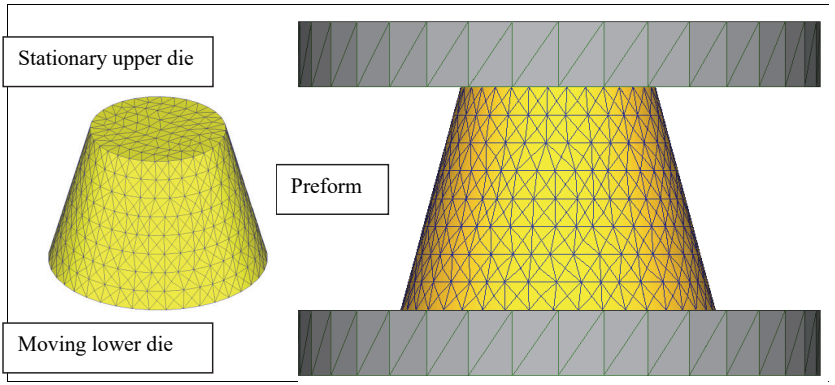

Figure 5.15: Models of Meshed Truncated Conical Preform with Tetrahedral Mesh.

To illustrate the effect of deformation characteristics and die speed on the magnitude of various power dissipations, die load and strains rates involved during upset-forging of conical preform, the computational conditions including geometries are as follows:

H = 17 mm, r_{to} = 12 mm, μ = 0.3 & 0.01, $\rho_i = 2 \times 10^3$ kg/m^3, σ_0 = 6.25 MPa and C_f = 1.6, 1.3 and 1.1 ($\alpha = 15^0$, 10^0 and 5^0 respectively, U = 10, 100 and 150 mm/sec.

5.2.2 Parametric Analysis

Figure 5.16 shows the preform profile during various stages of upset-forging. It is evident that as lower die travel increases preform deforms and slightly bulges. This is due to the formation of conical wedge of relatively undeformed metal immediately below the preform surface, where die-workpiece interfacial friction retards its plastic flow. Figure 5.17 shows the distribution of the total displacement of the preform in vertical direction during various stages of sinter-forging process, and may be seen that the lower surface of the preform has been displaced maximum and the upper surface the minimum due to the upper stationary die and lower moving die. The maximum value was seen in the range of 3.93 to 7.83 at the lower region of preform.

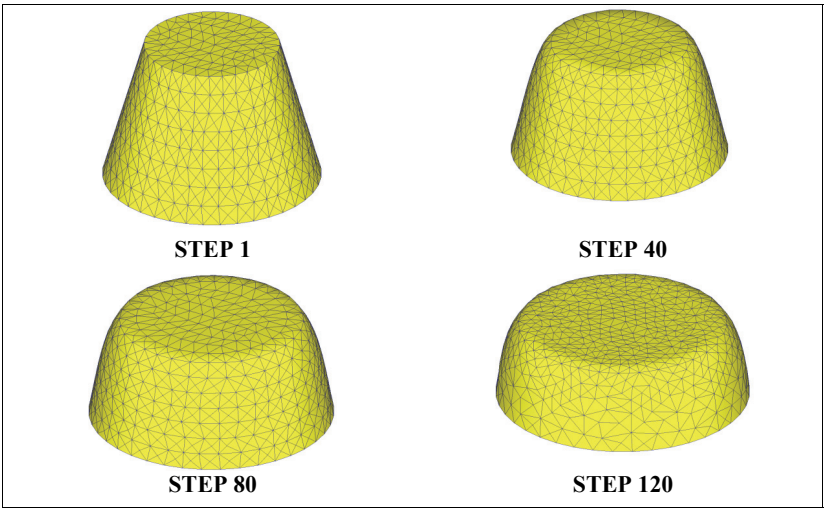

Figure 5.16: Preform Profiles during Open-Die Sinter-Forging of Truncated Conical Preform.

Figure 5.18 shows the effective stress distribution over the preform surface during various stages of sinter-forging simulation. It may be noted from the figure that nine/tracking points were considered over the preform surface at the various node points of the meshes and the stress values were measured at these points. The maximum stress of the order of 119 MPa was found at the peripheral region and least at the central region.

To illustrate the distribution of stress at the various height sections of the preform, the preform was sliced vertically and the stress distribution in form of contours were also plotted as shown in figure 5.19. The high stress concentration was found to be at the edges of the preform and the possibility of fracture was high at these points.

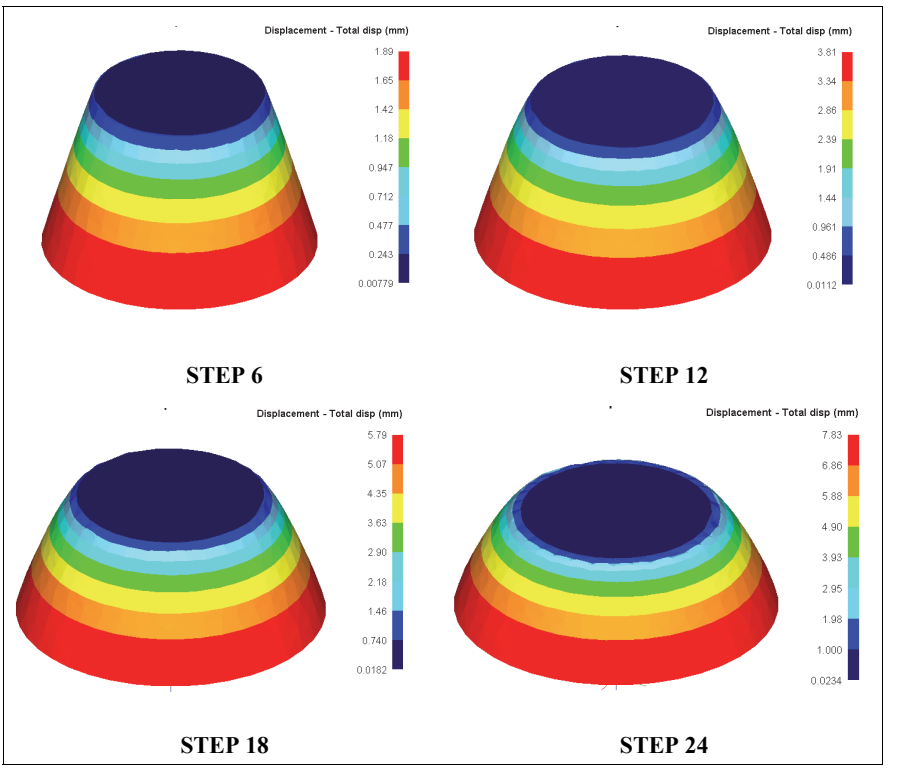

Figure 5.17: Distribution of Total Displacement during Open-Die Sinter-forging of Truncated Conical Preform.

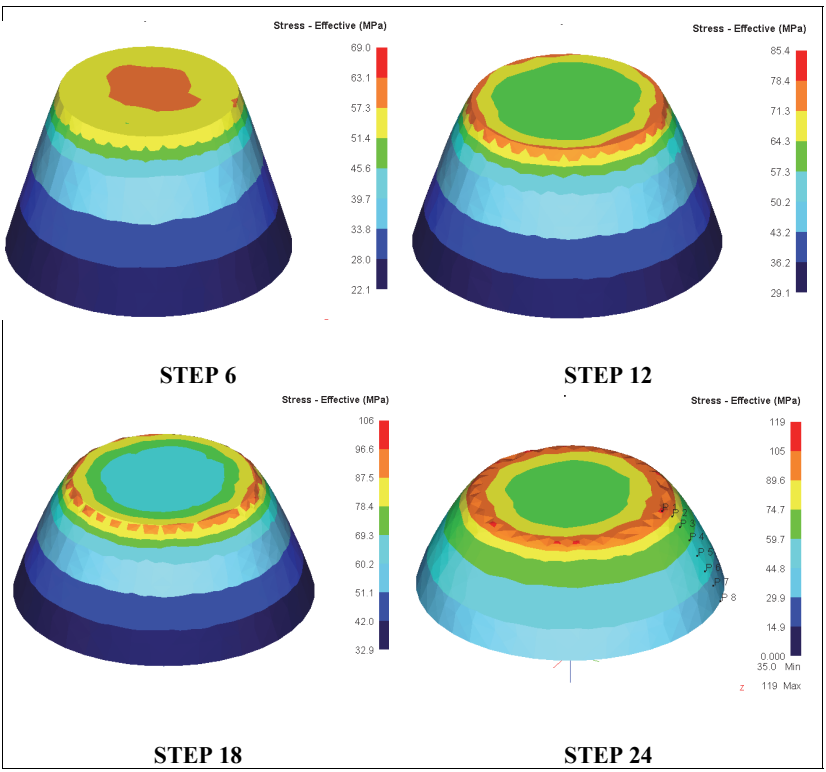

Figure 5.18: Effective Stress Distribution on the Preform Surface during Open-Die Sinter-forging of Truncated Conical Preform.

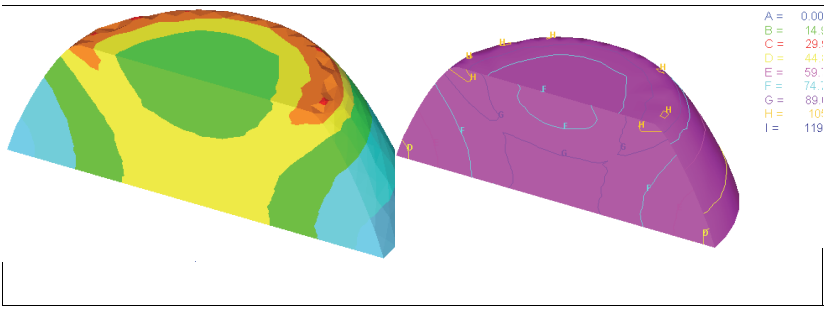

Figure 5.19: Effective Stress Distribution and Contour Profile on the Sliced Preform Surface during Open-Die Sinter-forging of Truncated Conical Preform.

The distribution of effective strain is shown in figure 5.20 and it is clearly evident that effective strain in the range of 1.2-1.6 mm/mm was found at several places on the preform surface. Figure 5.21 shows the velocity vector distribution on the preform surface and the maximum velocity in the order of 11-12 mm/sec was found on the vertical surfaces which are flowing radially outwards during upset-forging process and the least velocities were found on the interfacial regions of the preform.

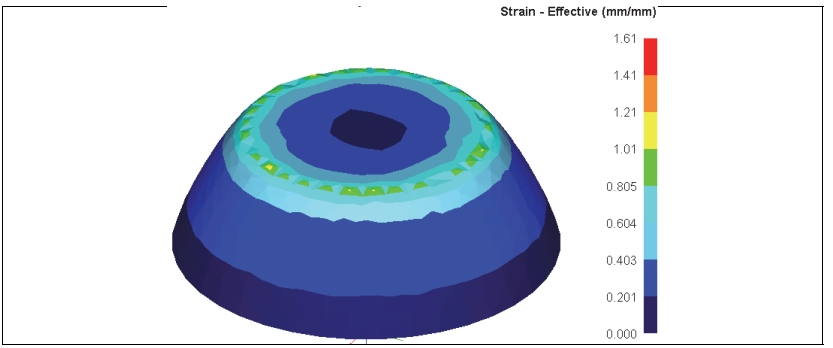

Figure 5.20: Effective Strain Distribution on the Preform Surface during Open-Die Sinter-forging of Truncated Conical Preform.

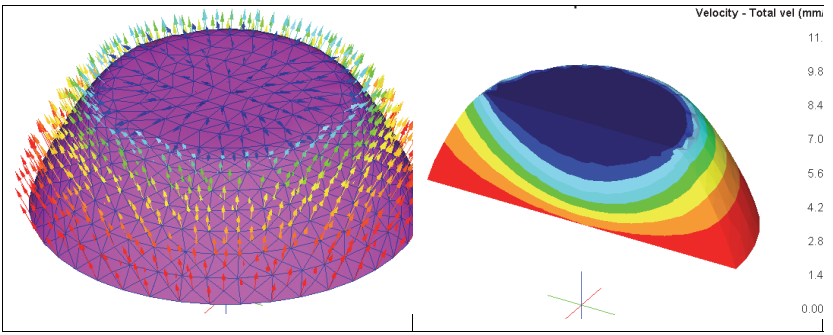

Figure 5.21: Velocity Vector Distribution on the Preform Surface during Open-Die Sinter-forging of Truncated Conical Preform.

Figure 5.22 and 5.23 shows the variation of the effective strain and effective stress with the upset-forging time or stroke and was found to increase exponentially initially and then remain fairly constant at the end of the upset-forging operation. The effective stress

was found to be higher for lower die velocity and preforms with smallest conical angle, whereas the effective strain was found to highest for the highest die velocity and least cone angle of the preform.Figure 5.24 shows the variation of internal energy dissipation with die velocity for different shape-complexity factor under high interfacial friction condition during open-die sinter-forging of truncated conical preform. It is apparent from the figure that internal energy dissipation increases exponentially with the increase in die velocity and becomes comparable with internal and frictional shear energy dissipations during sinter-forging operation, especially at higher die velocity. Thus, the magnitude of internal energy dissipation is fairly appreciable during mechanical processing of sintered materials at high die speeds and must be considered for accurate measure of die loads. The internal energy dissipation curves are also higher for low shape-complexity factors, which indicate that as the shape of the truncated conical preform approaches to that of an enclosing cylinder, energy dissipated in the form of internal forces also increases. Hence, cylindrical preforms require more internal energy for deformation, as compared to conical ones for the same amount of preform material.

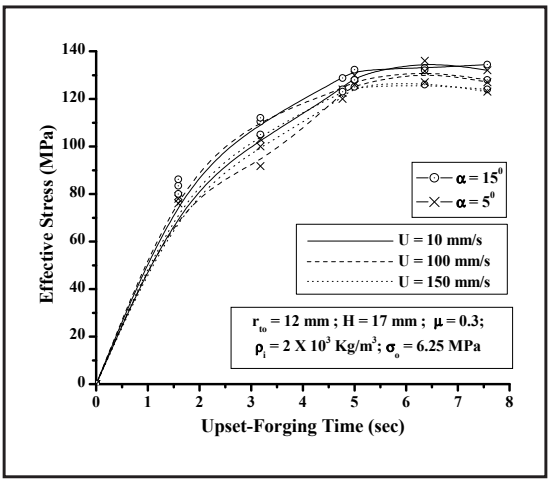

Figure 5.22: Variation of Effective Stress during Open-Die Sinter-forging of Truncated Conical Preforms.

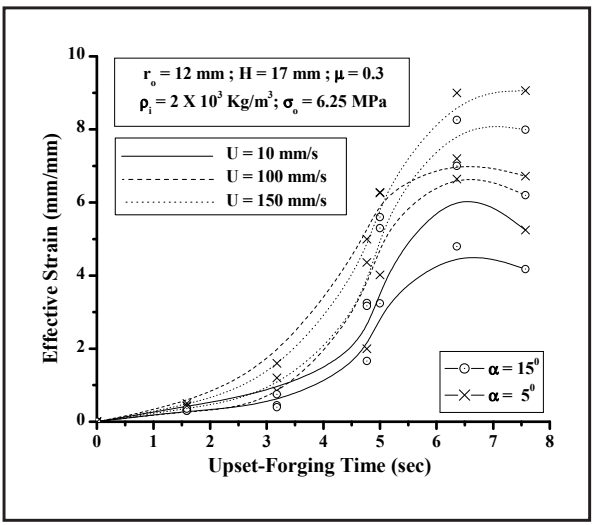

Figure 5.23: Variation of Effective Strain during Open-Die Sinter-forging of Truncated Conical Preforms.

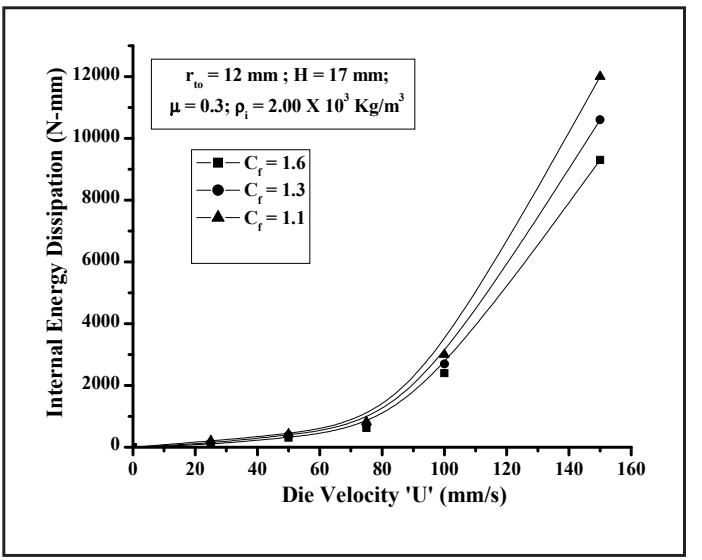

Figure 5.24: Variation of Internal Energy Dissipation with Die Velocity during Open-Die Sinter-Forging of Truncated Conical Preforms.

5.3 FEM SIMULATION OF OPEN-DIE SINTER-FORGING OF IRREGULAR TRAPEZOIDAL PREFORM

5.3.1 Computational Conditions

The finite element simulation of cold open-die forging of aluminium trapezoidal preforms has been performed using DEFORM software. To model the material during computer simulation, the stress-strain data for sintered aluminium trapezoidal preforms was uploaded to the material library of the software by conducting simple compression tests at different die speeds, i.e. different strain rates and corresponding stress-strain curves of type $\bar{\sigma} = A\bar{\varepsilon}^{n}\dot{\bar{\varepsilon}}^{m}$ MPa was generated as shown in figure 5.25, where 'A' was 110.6 MPa, 'n' was 0.22 and 'm' was 0, 0.75 and 1.5.

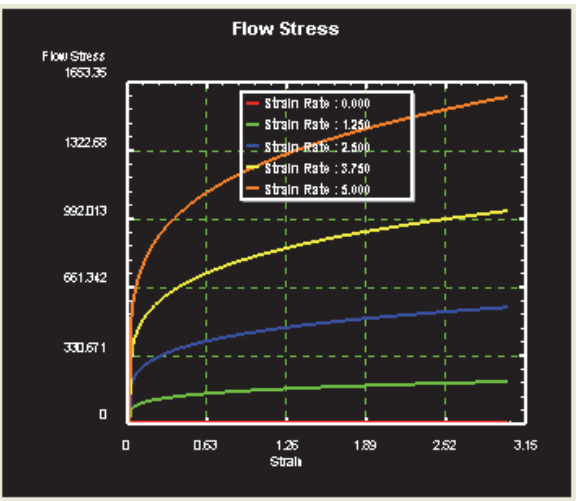

Figure 5.25: Flow Stress (MPa) of Sintered Aluminium Preform at Strain Rate Coefficient of 1.5.

The geometry of forging dies was generated in DEFORM software and were modeled as rigid, parallel and flat bodies with plastic trapezoidal preform placed in between them. The geometry of preform was generated using CATIA using part design workbench and data was imported to DEFORM in form of STL files. Three different die velocities of

10, 100 and 150 mm/sec respectively corresponding to strain rate coefficient of 0, 0.75 and 1.5 as described above were considered during the finite element simulation of sintered aluminium trapezoidal preform.

Tetrahedral elements 53468 numbers with size aspect ratio of 2.5 were used to mesh the preforms and finer meshes were generated close to the face edges of preform in order to better scope the forging process as shown in figure 5.26.

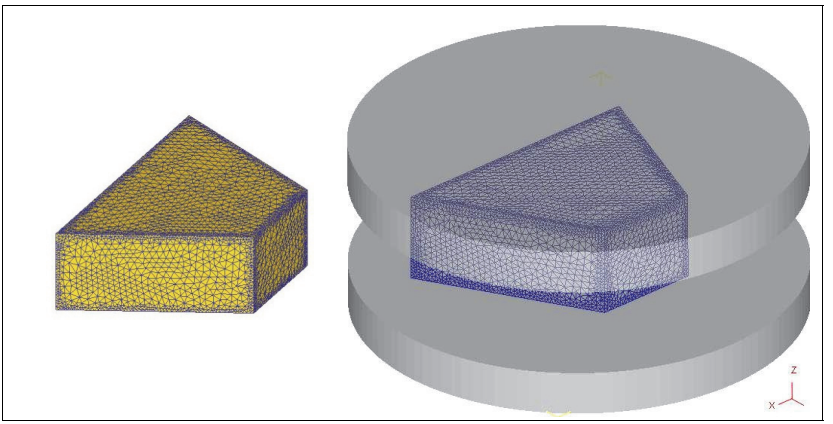

Figure 5.26: Models of Meshed Irregular Trapezoidal Preform with Four Noded Tetrahedral Elements

The complete open-die sinter-forging simulation was performed in 20 steps, each having stroke movement of 0.22 mm. The deformation criterion considered was the maximum forgeability of sintered aluminium trapezoidal preforms, which was experimentally found to be about 47%. The variation of effective stress, strain, strain-rate, forging load and internal energy dissipation with forging time was plotted for different die velocities. The distribution of total displacement, effective stress, strain and velocity vector in form of color codes and contours on preform surface were also obtained. To investigate these distributions over the preform vertical profile, sliced models were also generated.

5.3.2 Parametric Analysis:

A typical data of preform and deformation characteristics compatible with corresponding experimental work has been considered to illustrate the dynamic effects on the magnitude of various energies, die load and strains rates involved during open-die sinter-forging of irregular trapezoidal preform and is given as follows:

H = 10 mm; ρ_o = 0.80; ρ_i = 2 x 10^3 kg/m^3; σ_0 = 6.25 kg/mm^2; μ = 0.30 (high interfacial friction) and 0.01 (low interfacial friction); C_q = 0.85 and 0.60, U = 10, 100 and 150 mm/sec with three different strain rates coefficients 'm' equals to 0, 1.5 and 3 respectively.

Figure 5.27 shows the various stages of the trapezoidal preform during open-die forging. It is evident that as preform deforms, its height decreases and length, as well as breadth increases with slight bulging. Figure 5.28 shows the distribution of the total displacement of the trapezoidal preform during various stages of sinter-forging process, and can be seen the flow of material, bulging characteristic is uniform in all the lateral sides of preform, satisfying the regions being having kinematically admissible velocity field.

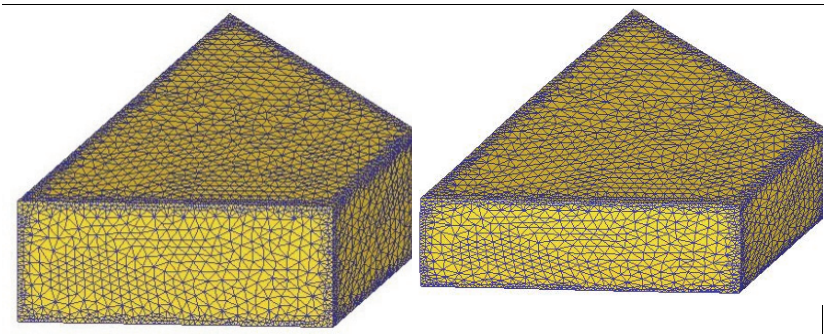

STEP 1 **STEP 5**

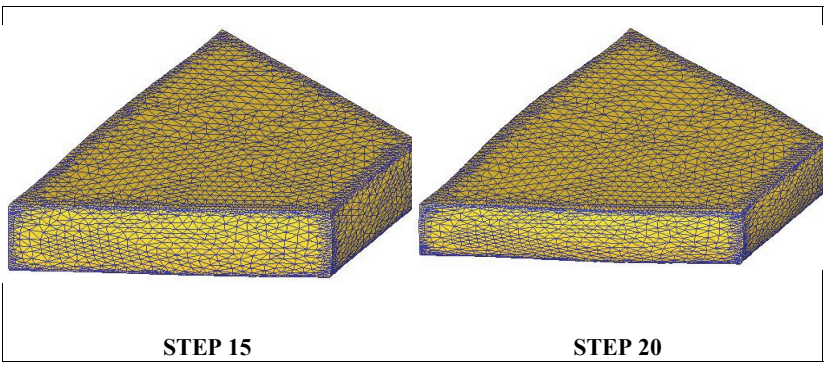

STEP 15 STEP 20

Figure 5.27: Various Stages of Irregular Trapezoidal Preform during Open-Die Sinter-Forging.

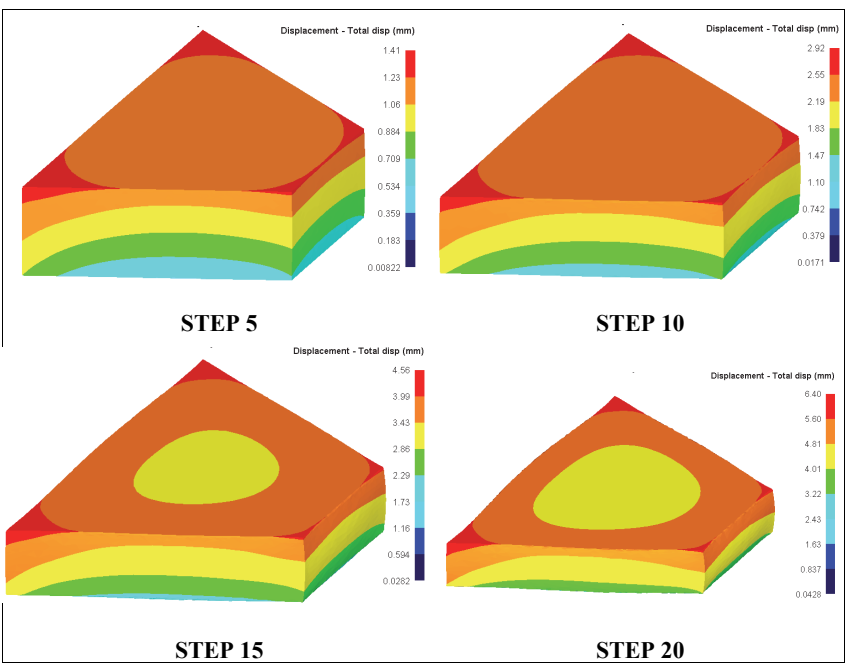

STEP 5 STEP 10

STEP 15 STEP 20

Figure 5.28: Distribution of Total Displacement of the Irregular Trapezoidal Preform during Various Stages of Open-Die Sinter-Forging Process.

To illustrate the distribution of effective stress at various height sections of the preform, it was sliced vertically and stress distribution was plotted as shown in figure 5.29. The magnitude of effective stress was computed and it can be observed that maximum stress in the order of 26200, 2170 and 129 MPa respectively, at different strain rate coefficient values 'm' equals to 0, 0.75 and 1.5 when the die velocity is 100 mm/sec at the peripheral region. It was also found about 64 -97, 544-1090 and 3280-13100 MPa respectively, in the central region of preform. With increase in strain rate the effective stress observed has also increased. Due to stress concentrations at the edges, the chances of preform fracture were maximum at these regions.

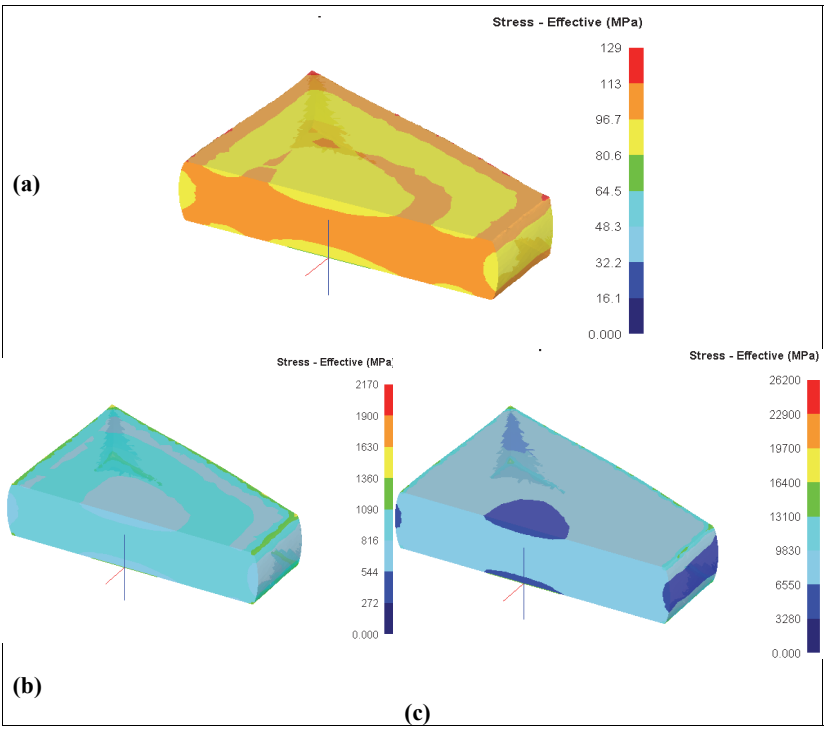

Figure 5.29 (a), (b) & (c): Effective Stress (MPa) distribution on Sliced Irregular Trapezoidal Performs at different Strain Rate Coefficients of 0, 0.75, and 1.5 respectively.

The distribution of effective strain is shown in figure 5.30 and it is clearly evident that it is in the order of about 2.01, 1.22 and 1.05 mm/mm at preform edges, where the chances of fracture were maximum, and observed that at higher coefficient of strain rate the effective strain is less with same die velocity. Also, the central region of sliced vertical profiles of preforms experienced strains in the magnitude of about 0.25-1, 0.3-0.7, and 0.2-0.6 mm/mm respectively.

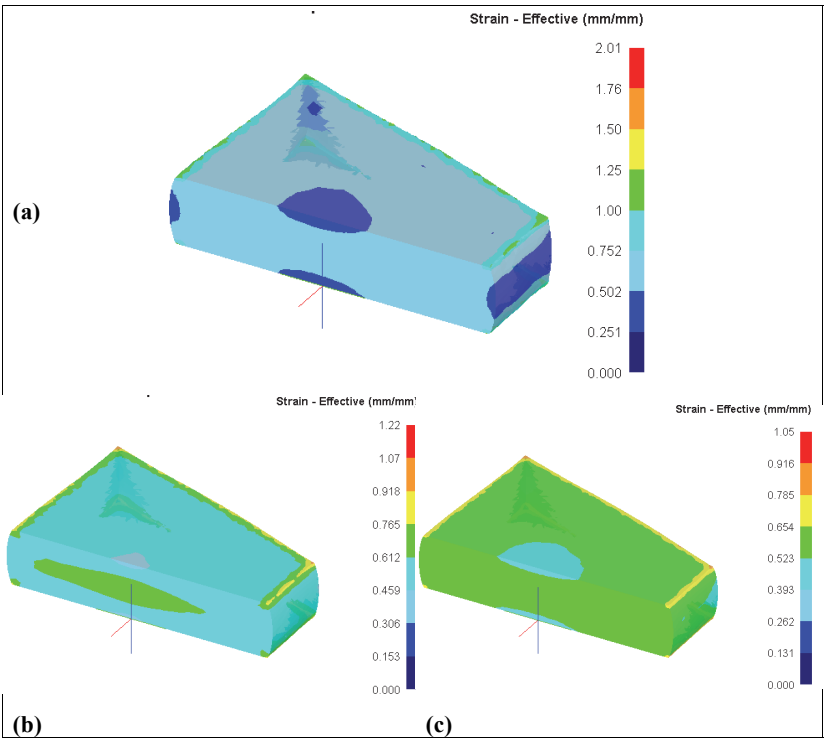

Figure 5.30 (a), (b) & (c): Effective Strain (mm/mm) distribution on Sliced Irregular Trapezoidal Performs at different Strain Rate Coefficients of 0, 0.75, and 1.5 respectively.

Figure 5.31 shows the velocity vector distribution on preform surface, which shows that velocity in the order of 181 mm/s was found on the peripheral vertical surfaces, which

are flowing radially outwards during open-die forging process. The central regions experienced least velocities in the range of 67-113 mm/s. It can also be noted that flow of material is from central to peripheral regions of the preform in vertically downward directions. The central region near the interface of preform bottom face and die exhibit zero velocity flow, indicating the presence of sticking region where dead regions of zero velocity are present.

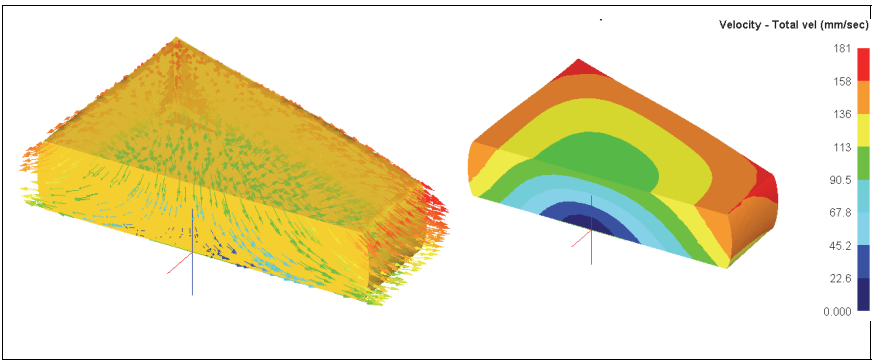

Figure 5.31: Distribution of Velocity Field (mm/sec) on Sliced Irregular Trapezoidal Perform during Open-Die Sinter-Forging Process.

Figures 5.32 (a), (b) & (c), and 5.33 shows the variation of the effective stress (MPa) and effective strain (mm/mm) respectively with forging stroke (mm) during open-die forging of sintered aluminium trapezoidal preform. It is clearly evident from the figure 5.32 that effective stress increases with forging stroke/height reduction and is higher for higher die velocity and higher strain-rates. It can be noticed that stress increases rapidly in the initial stages of deformation and then increases gradually till the preform fractures. This is due to the fact that initially compaction of preform is high and compression is low and preform is utilizing major external power supplied by die platens for closing of pores till its relative density reaches to a point that appreciable compression/deformation initiates.

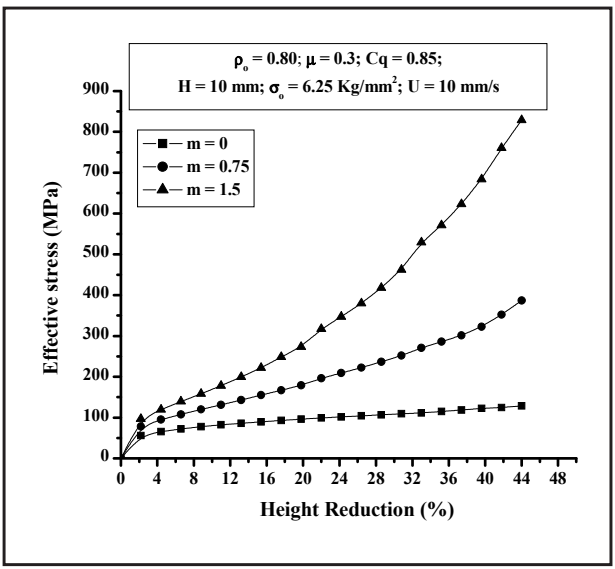

(a)

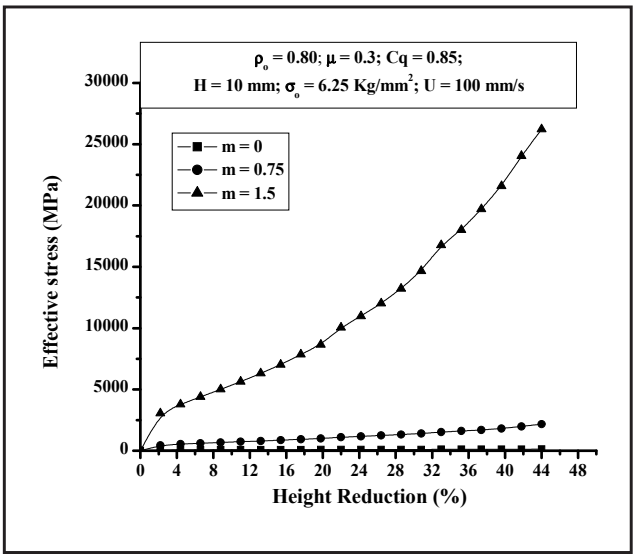

(b)

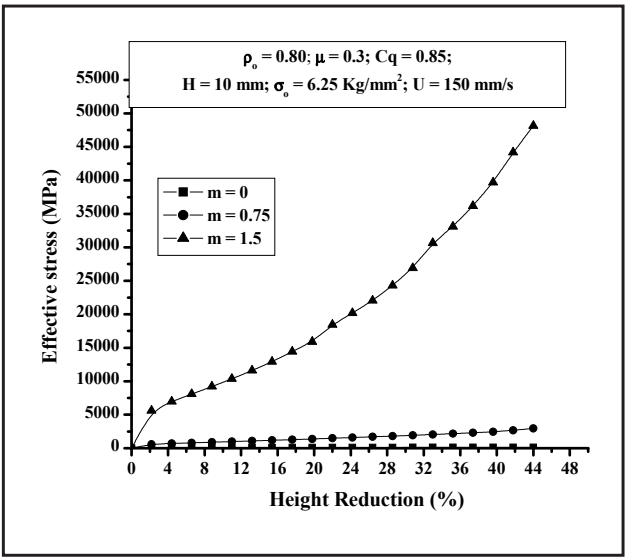

(c)

Figure 5.32 (a), (b) & (c): Variation of Effective Stresses (MPa) at different Die Velocities with % Height Reduction during Open-Die Sinter-Forging of Irregular Trapezoidal Preform.

Figure 5.33 shows the corresponding values of the effective strain and it is evident that strain increased exponentially throughout the process of the upset-forging operation with percentage of height reduction and are higher for lower strain-rate for same die stroke.

The variation of total energy supplied by die platens for deformation with die stroke or percentage of reduction is shown in figure 5.34 and it can be seen that it increases almost linearly with the die stroke. Also, the energy dissipations are higher for the given die velocity and at higher strain-rates. The increase in the amount of energy dissipations for higher die velocity and strain-rates signifies that effect of die speed and strain rates are vital deformation characteristics of a forging process and must be taken into consideration during analysis in of dynamic effects.

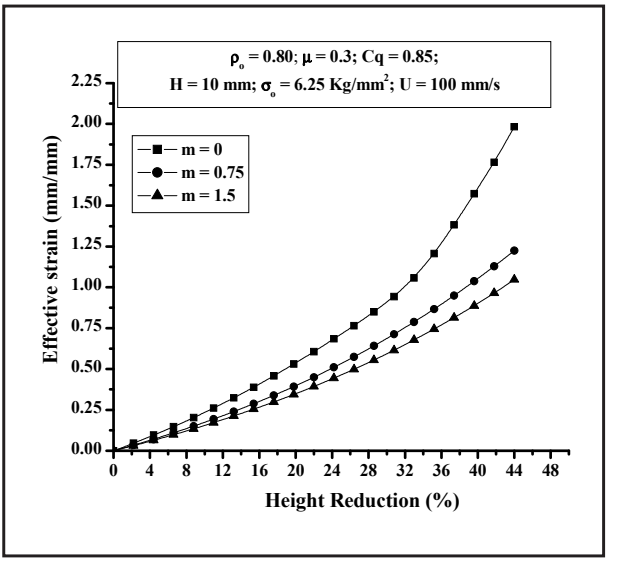

Figure 5.33: Variation of Effective Strain (mm/mm) with % Height Reduction during Open-Die Sinter-Forging of Irregular Trapezoidal Preform.

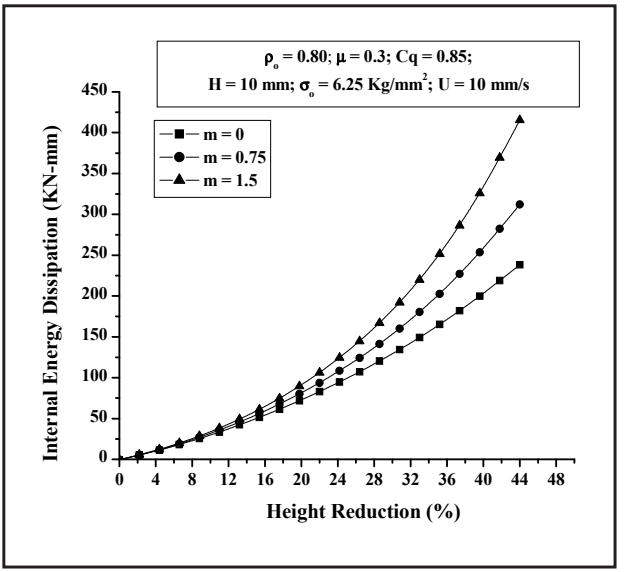

Figure 5.34: Variation of Internal Energy Dissipation (KN-mm) with % Height Reduction during Open-Die Sinter-Forging of Irregular Trapezoidal Preform.

Figure 5.35 shows the variation of forging load with die stroke during cold open-die forging of trapezoidal preforms. It is clearly visible from the figure that forging load increases rapidly during the initial stage of deformation and then increases gradually in a linear manner with respect to forging stroke or time. This is attributed due to the fact that relative density of preform increases rapidly during the initial stage of deformation leading to higher resistance to deformation. Thus, higher loads are required for deformation during this stage. After this stage, the rate of preform densification is slow and major proportion of the energy is utilized in the deformation of preforms. Also, it is observed that the die loads are higher for higher die velocity and strain-rates.

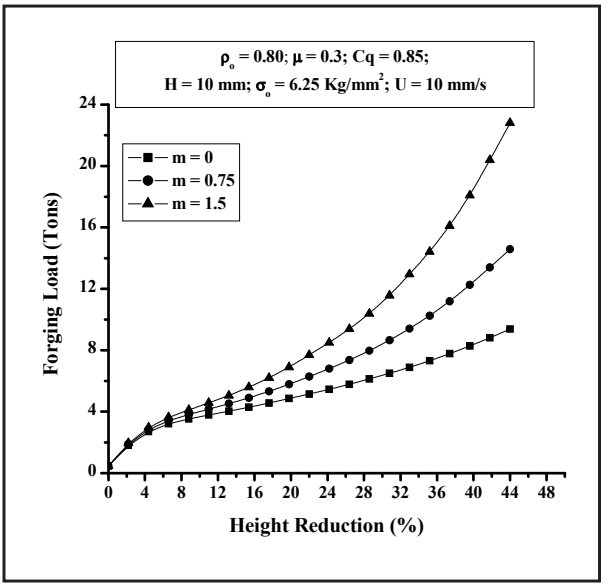

Figure 5.35: Variation of forging load (tons) with die stroke during Open-Die Sinter-Forging of Irregular Trapezoidal Preform.

CHAPTER 6

FEM ANALYSIS OF CLOSED-DIE SINTER-FORGING OF DOUBLE-HUB FLANGE PREFORMS

This chapter deals with the finite element analysis of the precision net-shape closed-die sinter-forging of Aluminium metal powder preforms into double-hub flange components. In general, closed-die forging process is an extremely complex process with regards to the variables, like designing workpiece geometry, material, and tool and die geometry, and the amount of deformation etc. To achieve and determine the optimum means for production of high-quality products at lowest cost and least time, the designer has to predict and estimate the maximum stress distribution on the dies, the maximum load required by the equipment and the total energy necessary to complete the deformation, further enabling the calculations of strains and stresses on the dies during the forging process. Many researchers had investigated these forming processes using both experimental and theoretical methods, but the results obtained didn't shown general agreement. At the same time, due to the complexity of the deformation and the imperfection of the experimental and analytical results, there are still many problems yet to be reported.

The objective of this work is to simulate and investigate the effect of die velocity, preform aspect ratio on internal energy dissipations, die cavity fills, and die loads requirements during closed-die sinter-forging process of double-hub flange preforms. The stresses, strain rates and strain distributions at different positions of the workpiece and at different forging times during the process were analyzed and presented graphically. Also, the deformation zones were analyzed in details to investigate the associated deforming patterns using finite element method based application (DEFORM Software).

6.1 COMPUTATIONAL CONDITIONS DURING FEM ANALYSIS

The simulation of net-shape sinter-forging of cylindrical preform and into double-hub flange components is performed by placing the preform within the two rigid closed die-halves comprising of upper punch, counter lower punch and container as shown in schematic diagram figure 6.1 and was performed using Deform ^{TM} -3D software, which is based on the incremental Lagrangian finite element code.

The geometry of the forging dies was generated in Deform ^{TM} software and was modeled as rigid, parallel and flat bodies with plastic preform placed in between them. The components of the model, i.e. geometry of preform, upper plunger, container, lower plunger was generated using CATIA V5.0 software using part design module / workbench and data was imported to the Deform ^{TM} software in form of STL files. The cylindrical preform with the required dimensions depending upon the shape-complexity factors was modeled and located centrally with the axis of closed-die as shown in figure 6.2. The preforms were forged to various die travels (height reductions), till it touched the middle of container and the die corner fillings were complete. The figure shows the two stages of deformation, i.e. free barreling stage and constraint deformation stage where die corners are formed and filled.

The 4-Noded Quadrilateral, large strain axi-symmetric element with 2000 numbers were used to mesh the preform for performing the sinter-forging process assuming axi-symmetric conditions, i.e. the geometry of every plane radiating out from the centerline was considered identical. The axis of symmetry of the model is fixed in the ‘x’ direction, as shown in figure 6.3. The figure shows the meshed 2D axi-symmetric and 3D model of the preform.

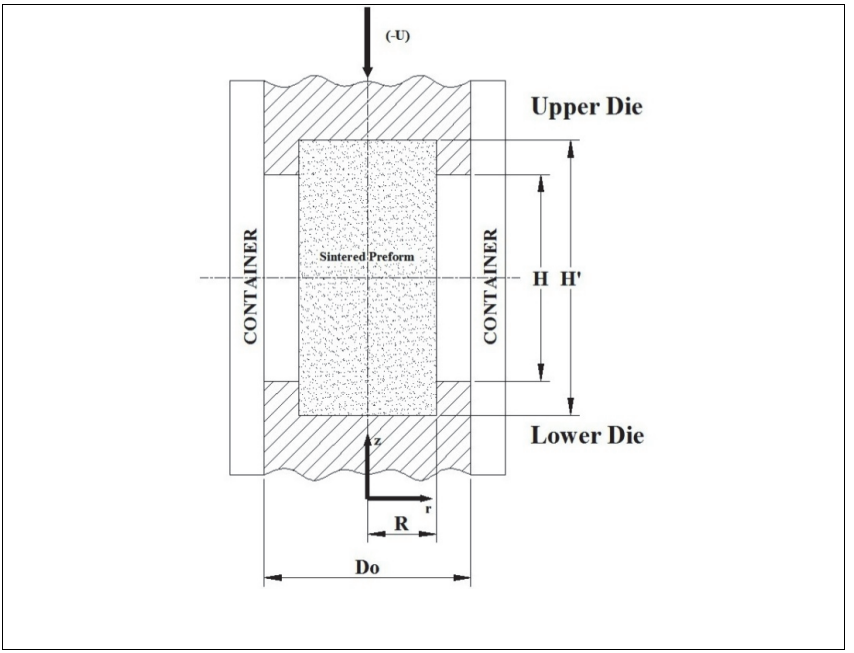

Figure 6.1: Schematic diagram of Closed-die Sinter-Forging of Double-Hub Flange Preform with Upper Die, Container, Preform and Lower Die.

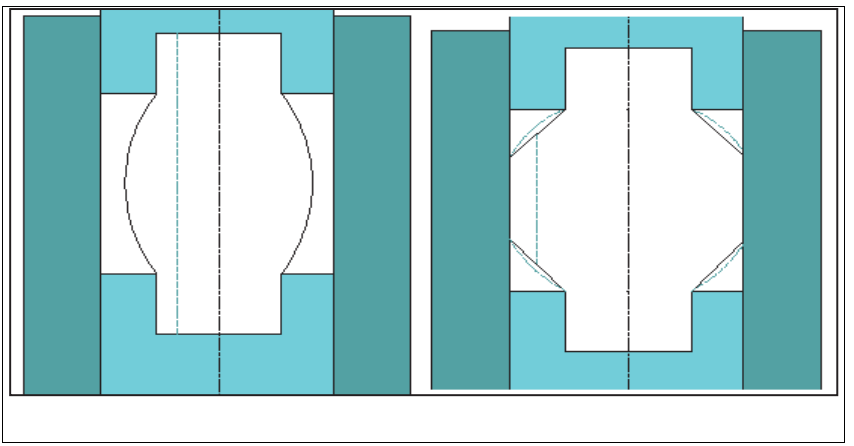

Figure 6.2: Deformation Stages during Closed-Die Sinter-Forging Process.

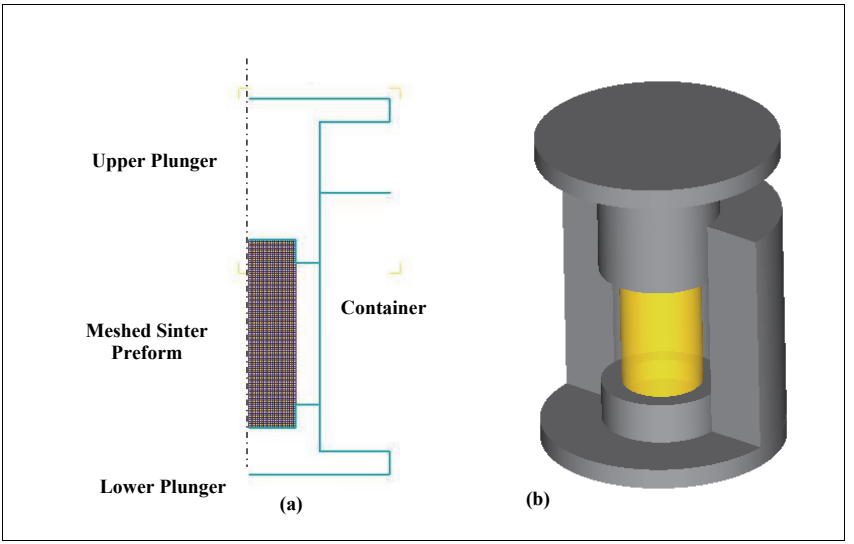

Figure 6.3 (a) & (b): Models of Meshed 2D Axi-Symmetric and 3D Cylindrical Preform.

The deformation was carried at three different velocities of 1, 10 and 100 mm/sec. The stress-strain data for the sintered aluminium performs was recorded experimentally and the corresponding stress-strain curve data of form $\bar{\sigma} = A\bar{\varepsilon}^{n}$**MPa** was generated and added to its material property library. The material flow stress obtained during experimentation was modeled depending upon the stress-strain curve data with 'A' as 110.6 and strain coefficient n = 0.22. The effective coefficient of interfacial friction was considered as 0.3 for lubricated inter-facial frictional conditions, which was obtained after performing the ring compression tests under the lubricated (graphite paste) conditions. Figure 6.4 (a) shows the experimental flow curve of the sintered aluminium material, which was later added to the DEFORM material library as shown in figure 6.4 (b).

Experimental Data

Stress Values	Strain Values
0.00	29.58
0.02	44.71
0.06	59.15
0.17	74.41
0.36	88.13
0.74	103.55
1.36	118.30
2.36	133.55
3.74	147.88

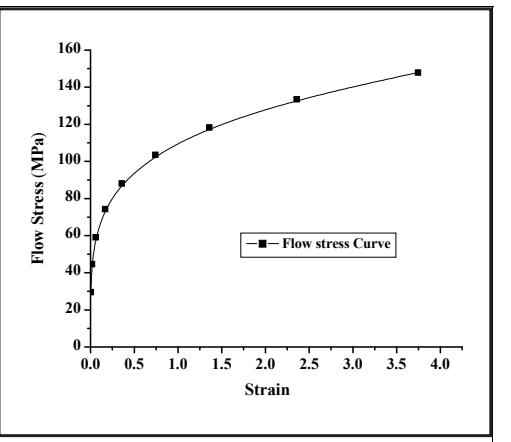

Figure 6.4 (a) : Flow Stress Curve of Sintered Aluminium Preform based on the Experimental Data.

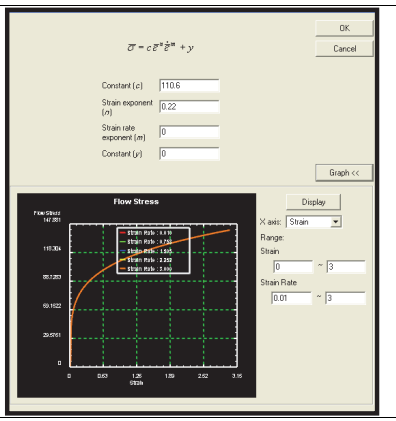

Figure 6.4 (b): Flow Stress Curve of Sintered Aluminium Preform added in Deform Software.

The complete sinter-forging simulation was performed in 20 steps having stroke movement of the die platens in each step and equal to the required reduction in the height of the preform based on the shape complexity factors. The deformation criterion considered is based on the maximum formability of the sintered aluminium preforms,

which was experimentally found to be about 44 percent. Considering typical data of preform and deformation characteristics as; R = 10 mm; D_o = 30 mm; H = 30, 22.5 and 15 mm.

The variation of effective strain, effective stress, effective strain rate, forging load and internal energy dissipation with sinter-forging time were plotted for different die velocities. The distribution of total displacement, effective stress, effective strain and velocity vector in form of color codes and contours on the preform surface were obtained. To investigate these distributions over the profile, preform slicing was done and the results were again plotted. The effect of die velocity, and preform aspect ratio on the energy dissipations, die cavity fills and the die loads were investigated and results for the deformation modes were compared. The validation of the simulation was done by comparing its results with the experimental results and was found to reasonably agree with each other, which indicated that finite element simulation represents fairly well with the present sinter-forging process.

6.1.1 Parametric Analysis

Figure 6.5 shows the preform profile during various stages of the closed-die sinter-forging. It is evident that as the lower die travel increases, the preform deforms and slightly bulges radially outwards because of the die-workpiece interfacial friction, which retards its plastic flow as in case of conventional open-die sinter-forging, till it reaches and touches the middle of container sidewalls. During this stage of deformation, contact with container wall is around the mid height of workpiece and corner regions of die cavity remain unfilled. The subsequent stage consists of constrained deformation of bulged preform, where corners are formed and filled.

Figure 6.6 shows the distribution of the total displacement of the preform in both the direction and may be seen that the surface of the preform has been displaced away from the preform centre towards the die cavity and was maximum at the middle and the upper portion of the preform. As the deformation progress further, results the material to fill in the entire die-cavity. When the height reduction was 44 percent, the maximum

displacement at the middle portion of preform surface observed was 6.62 mm, gradually moving away towards the upper die region.

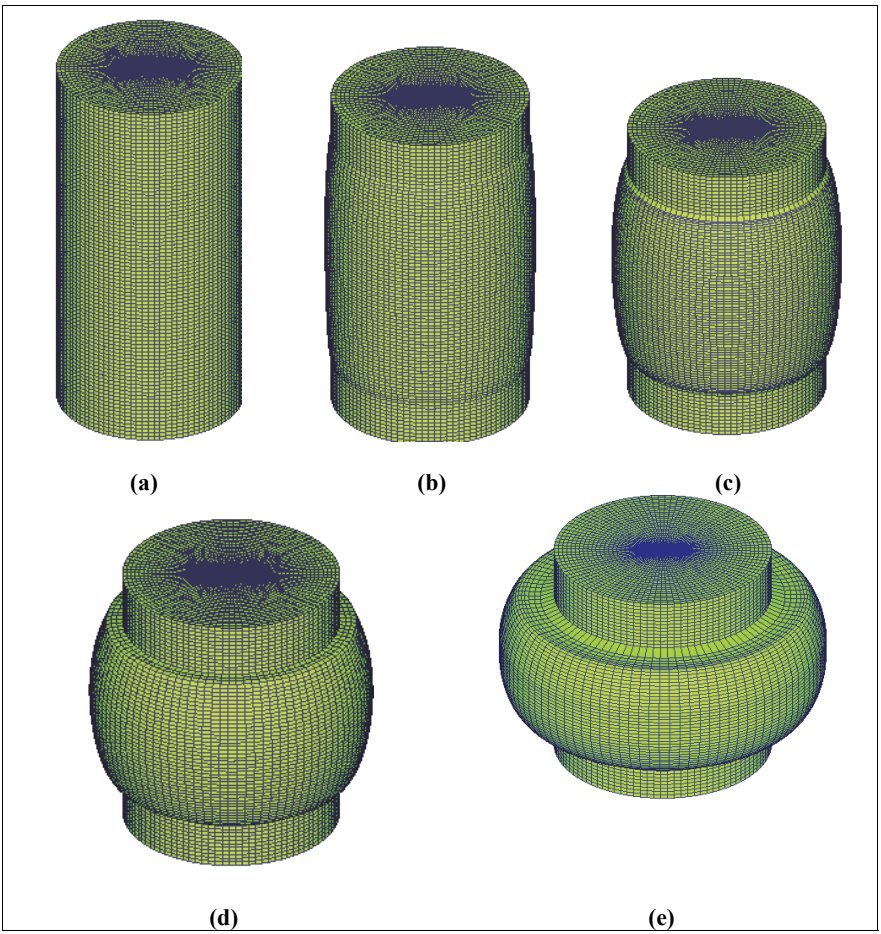

Figure 6.5 : Preform Profiles during Closed-Die Sinter-Forging of Double-Hub Flange Preform.

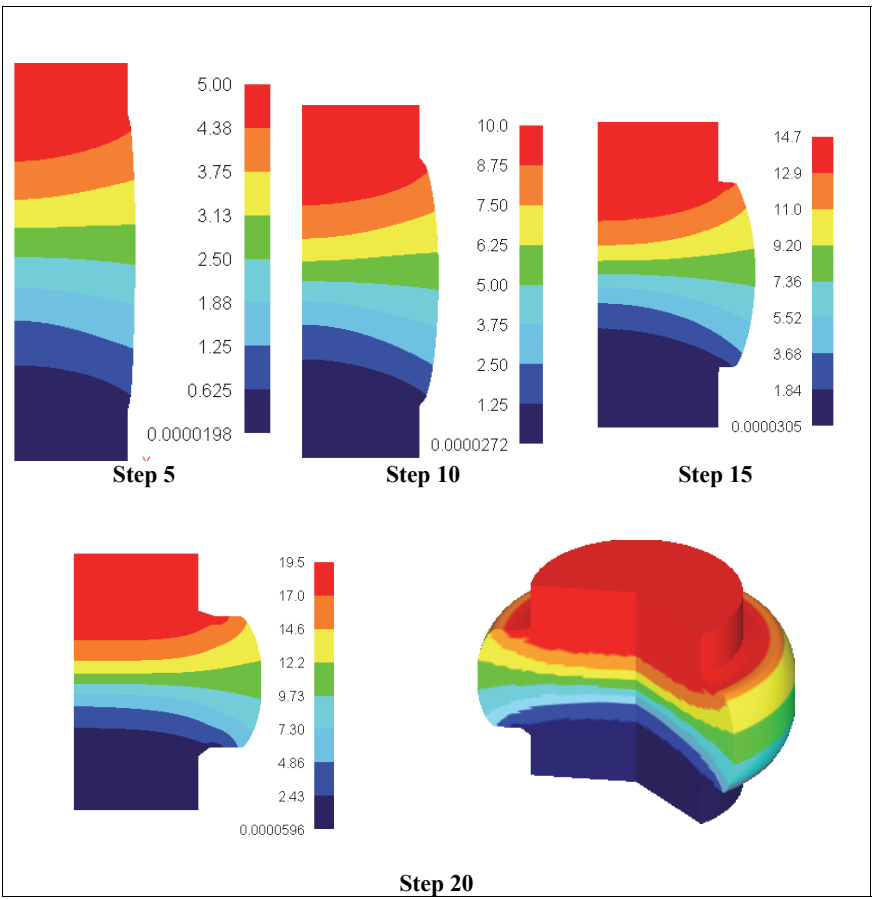

Figure 6.6: Distribution of total Displacement on the Preform Surface during Closed-Die Sinter-Forging of Double-Hub Flange Preform.

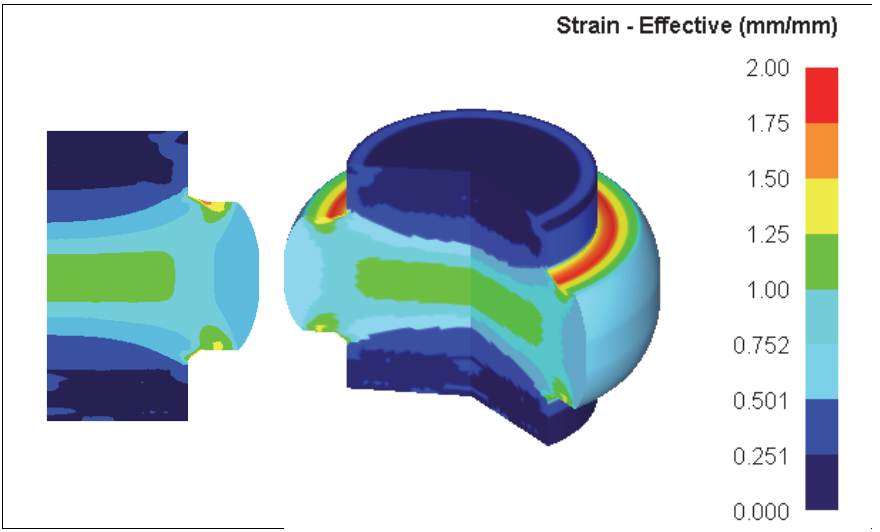

Figure 6.7: Effective Strain Distribution on the Preform Surface during Closed-Die Sinter-Forging of Double-Hub Flange Preform.

The distribution of the effective strain is shown in figure 6.7 and it is clearly evident that the effective strain in the range of 0.5-1.19 mm/mm was found at the peripheral region on the preform surface. Figure 6.8 shows the effective stress distribution over the preform surface at the end of the closed-die sinter-forging process, when the specimen with unity aspect ratio is considered to be deforming under high die velocity of 100 mm/sec. The value of stresses in the order of 90 to 129 MPa found to be decreasing from the die surface to the middle portion of the specimen. To illustrate the distribution of stress at various height sections of the preform, the preform was sliced vertically and the stress distribution in form of solid colors was also plotted. The highest stress concentration was found to be at the upper surface and edges of the preform, which is in contact with upper die, having a value in between 100 to 129 MPa, confirms the possibility of fracture at these points. This is because of the plastic deformation and the sliding of the preform on the die surface.

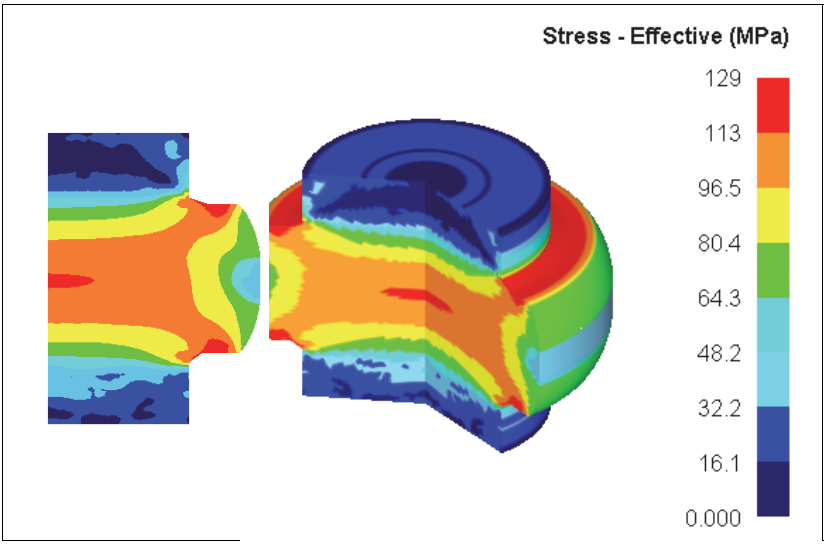

Figure 6.8: Effective Stress Distribution on the Preform Surface during Closed-Die Sinter-Forging of Double-Hub Flange Preform.

Figure 6.9 shows the velocity vector distribution on the preform surface and the maximum velocity in the order of 70 to 112 mm/sec was found on the vertical surfaces, which are flowing radially outwards during closed-die sinter-forging process and the least velocities were found on the interfacial regions of the preform. At the early stage of deformation the magnitude of the material flow rate was found to be higher and towards downward the direction of forging, later flowing towards the upper side with slower rate after touching the container wall.

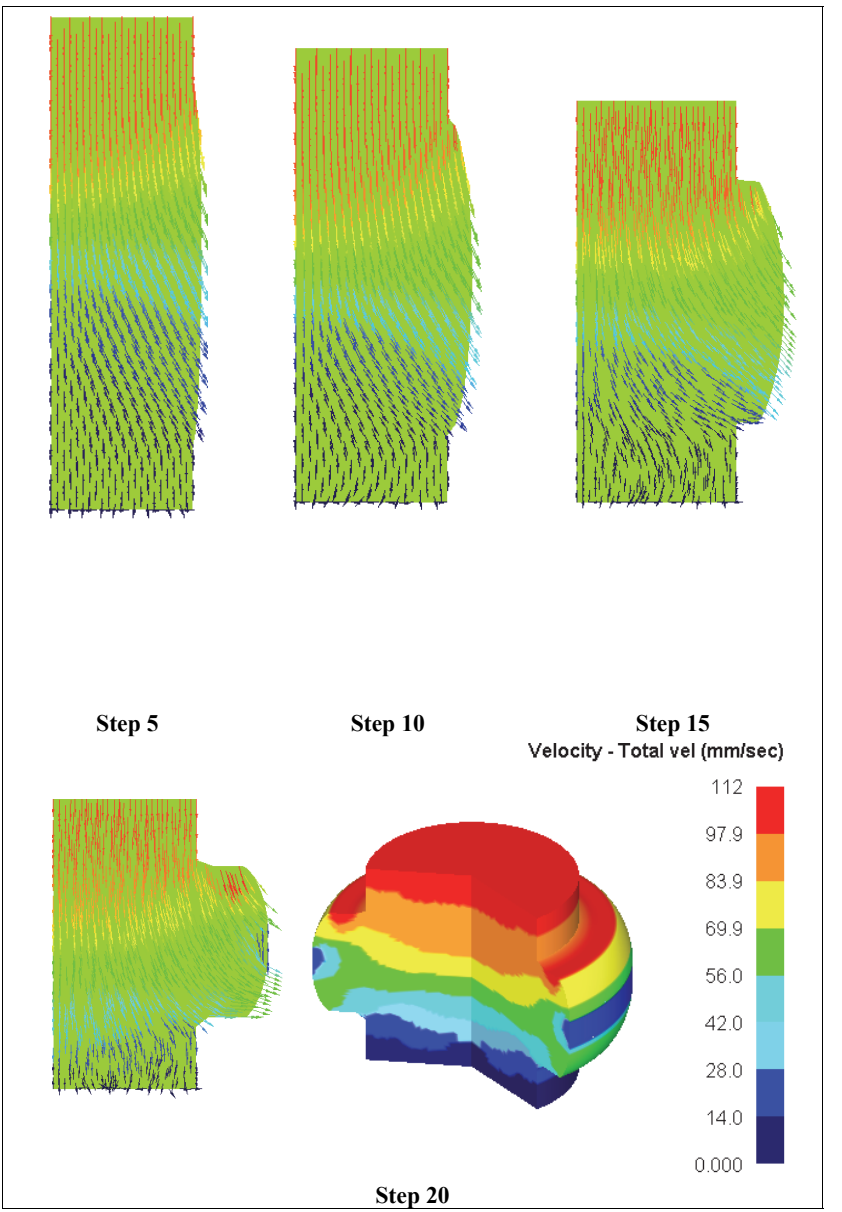

Figure 6.9: Velocity Vector Distribution on the Preform Surface during Closed-Die Sinter-Forging of Double-Hub Flange Preform.

Figure 6.10 and 6.11 shows the variation of the effective stress and effective strain for H/D_o ratios at different velocities with reduction of height. It was found to increase exponentially initially and then remain fairly constant at the end of the sinter-forging operation. The effective stress and effective strain was found to be higher for lower H/D_o ratio preforms. This is due to early densification of shorter preforms and also, when it comes in contact with the container wall the high constraint deformation and resistance against metal flow during final stages of the die filling results higher values.

Figures 6.12 shows the variation of external energy supplied by the die platens with height reduction, and it is found to increases exponentially with the die movement, indicating that internal energy dissipation is appreciable at high-speed deformation. Also, the curves are lower, for lower-shape complexity factors and higher for lower die velocity indicating the increase in the internal energy requirement. This may be due the fact that during early stage of deformation the sintered material which is occupied in both the recesses of upper and lower die considered as a large sized dead zone absorbs large amount of external energy supplied by die platens to impart the required inertia and with higher squeezing effect into cavities of impression.

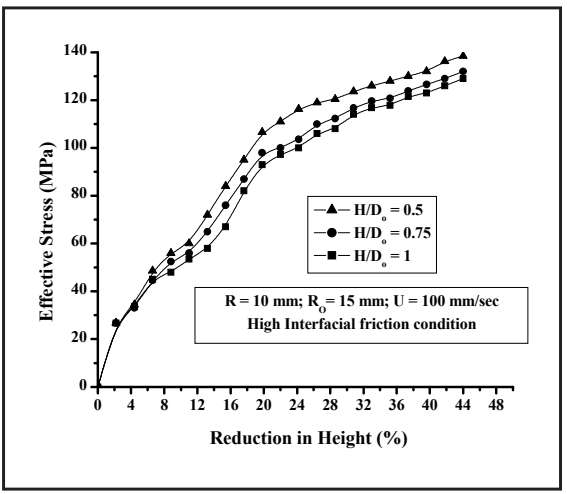

Figure 6.10: Variation of Effective Stress with % Height Reduction during Closed-Die Sinter-Forging of Double-Hub Flange Preform.

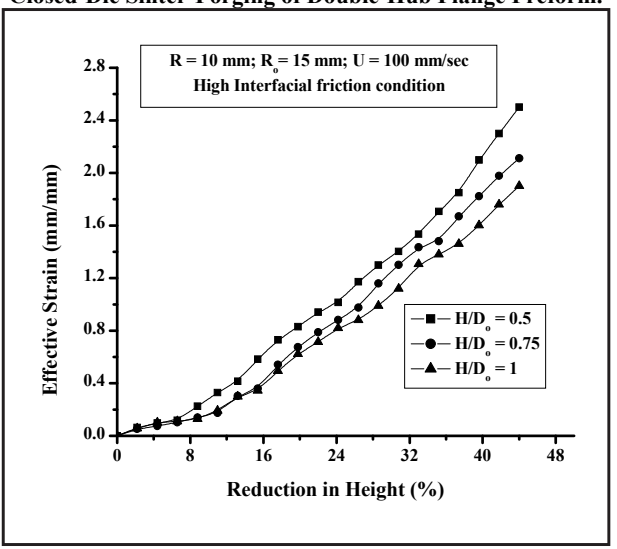

Figure 6.11: Variation of Effective Strain (mm/mm) with % Height Reduction during Closed-Die Sinter-Forging of Double-Hub Flange Preform.

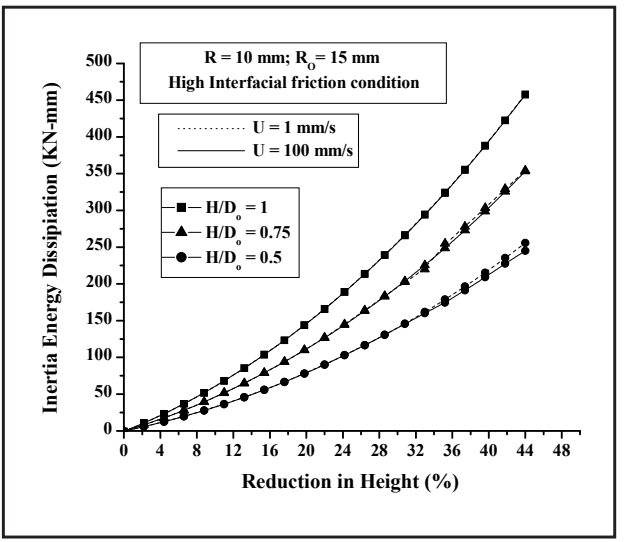

Figure 6.12: Variation of External Energy with % Height reduction for Different Die Velocities during Closed-Die Sinter-Forging of Double-Hub Flange Preform.

CHAPTER 7

FEM ANALYSIS OF ROTARY SINTER-FORGING OF CYLINDRICAL PREFORMS

This section deals with the three dimensional finite element simulation of the rotary sinter-forging of the axi-symmetric Aluminium cylindrical preforms using DEFORM-3D software. Rotary forging process is the most complicated of all the forging processes, as it involves the combinational effect of the rolling and the pressing action between the fixed flat bottom die and the rotating or swiveling upper die with an inclined conical working face. The workpiece is deformed gradually between an upper conical die having orbital motion with an inclined rotating axis, and the lower die, which moves upwardly (sometimes lower die is stationary and upper die is moving downward along with the rotary motion). Thus, when the workpiece is pressed repeatedly for several times, plastic deformation of the workpiece will be completed perfectly. There are several advantages also, e.g. the load requirement to carry out the deformation is very low due to the relatively small area of the instantaneous contact surface. This leads to high tooling life and requirement of low capacity presses resulting into reduced initial investment and maintenance cost. Also, the rotary motion substantially reduces the interfacial friction leading to better metal flow in the radial direction and further reducing the deformation load. The schematic representation of rotary-forging is shown in figure 7.1.

From the above description, it can be seen that rotary sinter-forging process is a complex metal forming process. Therefore, it is necessary to establish a reasonable 3D FE model to investigate the rotary forging process. The variation in the forging load against the reduction in height of the preform, and the change in the geometry of the preforms were critically analyzed. The effective strain and effective stress distribution were plotted, to understand the nature of the stress and strain involved in the indented contact area, as well as during sweeping of the indented contact area over the entire top surface of the preform.

Figure 7.2 shows the shape of the indented conical contact surface on the top of the cylindrical preform.

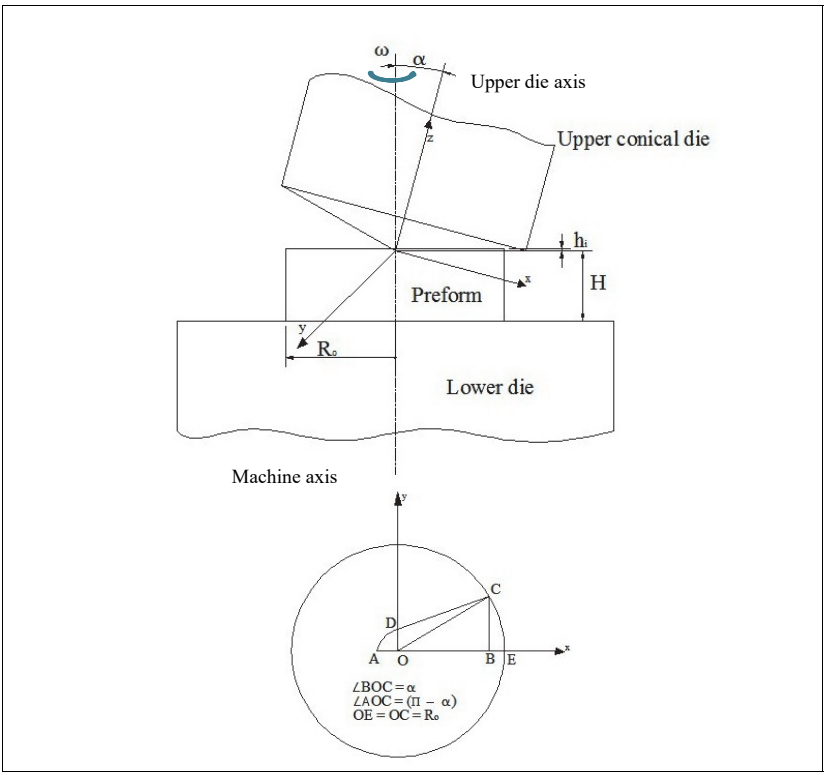

Figure 7.1: Schematic Diagram of the Rotary Sinter-Forging of the Cylindrical Preform.

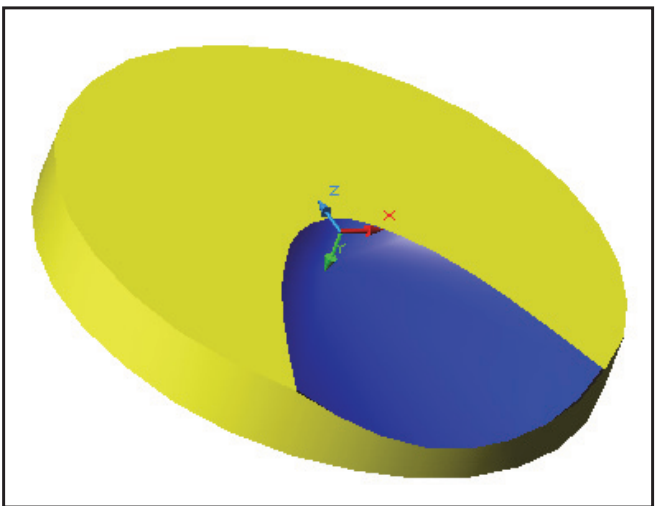

Figure 7.2: Illustration of Conical Indented Contact Area on the Top Surface of the Cylindrical Preform.

7.1 COMPUTATIONAL CONDITIONS DURING FINITE ELEMENT ANALYSIS

The simulation of rotary sinter-forging of axi-symmetric cylindrical preform was performed using Deform ^{TM} -3D software, which is based on the implicit Lagrangian finite element code. The rotary forging dies were modeled as rigid bodies with required dimensions using CATIA software (as *.CATPART files) and later imported as STL files as shown in figure 7.3. The geometry of the axi-symmetric cylindrical preform with required dimensions was modeled in the Deform software. In the coordinate system as shown in figure, the upper die is to rotate only about the axis while its other degrees of freedom are constrained. Similarly, the lower die is constrained to translate only along the axis while its other degrees of freedom are also constrained.

There is also a possibility during orbital rotation of the upper die, that the cylindrical preform may struck and rotate along with the die. To avoid this, constraint been exerted between the bottom surface of the workpiece and the top surface of the lower die, considering it to be as sticking zone. There are two contact pairs; one between the conical

surface of upper die and the upper end surface of the cylindrical preform and the other in between the upper surface of the lower die and lower surface of the cylindrical preform. The two contact pairs were inter-connected allowing to have relative sliding motion of the two surfaces, contributing to the interfacial friction condition of the contact pairs as per the coulomb friction model. The effective coefficient of interfacial friction was considered as 0.3 and 0.05, which were computed during the ring compression tests.

The cylinder preform considered in the analysis is a 3D deformable porous body with initial density of 0.8 and the entire preform body was discretized with 17528 numbers of tetrahedral elements. Finer meshes were generated close to the face edges in order to better scope the forging process. During simulating large plastic deformation processes, because of flow of the materials, there are severe chances of the mesh distortion, which may lead to the loss of the computation precision. To overcome these problems the meshing was done with the tetrahedral elements, as it has the capability to readapt and remesh at critical situations and reduce the distortion of the elements, as well as control the mode of zero energy. The corresponding stress-strain curve data of form $\bar{\sigma} = A\bar{\varepsilon}^{m}$ MPa was generated based on the basic experimentation and added to its material library.

The complete rotary sinter-forging simulation was performed in 10 steps having stroke movement of the die platens in each step equal to 0.25 mm, and the variation of forging load, and internal energy dissipation with height reduction, die velocities, angular velocities, half cone angles, and sinter-forging time were analyzed. The distribution of total displacements, effective stresses, effective strains and velocities in the form of color codes and contours on the preform surface were plotted.

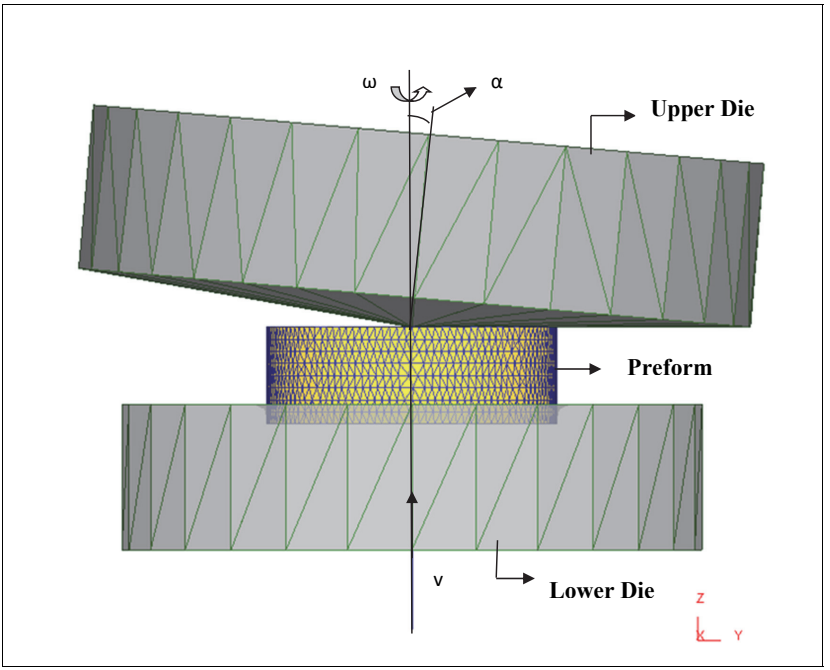

Figure 7.3: Finite Element Meshed Model With 4-Noded Tetrahedral Elements during Rotary Sinter-Forging Process.

7.1.1 Determination of Key Forming Conditions

In rotary sinter-forging, the relative movement between the preform and upper conical die is a spiral feed, and the outline and the shape of the contact zone can be obtained geometrically. As shown in the figure 7.1, the cone axis of upper conical die is swelled by an angle 'α' with respect to vertical axis, which is also its skew contact angle. This makes its nearest generator to the preform top surface horizontal. It is assumed that initially, the upper conical die is fed axially to an indentation depth 'h_i' into the preform top surface having initial height and radius as 'H' and 'R_o' respectively. This conical indented contact area is projected on the *'XOY'* plane.

In rectangular coordinate system, the equation of the upper conical surface of the cylindrical preform can be expressed as:

$$z \cos \alpha + x \sin \alpha \square S = 60v/n \tag{7.1}$$

where 'α' is the inclination angle of upper die, 'v' is the feed rate of the lower die, 'n' is the rotational speed of the upper die around the machine axis, and 'S' is the feed amount per revolution.

The equation for conical surface of upper conical die is given as *Zhang M.* [143]:

$$x^2 + y^2 - \left(\frac{z^2}{\tan^2 \alpha}\right) = 0 \tag{7.2}$$

$$\left(\frac{z \cos \alpha}{h_i}\right) - \left(\frac{x \tan \alpha}{h_i \cos \alpha}\right) = 1 \tag{7.3}$$

Equations 6.2 and 6.3 are solved simultaneously and hence, equation for conical indented surface created on top surface of cylindrical preform is given as:

$$y^2 = \left(\frac{h_i^2}{\tan \alpha \cos^2 \alpha}\right) + \left(\frac{2h_i}{\tan \alpha \cos^3 \alpha}\right) x - \left(\frac{1}{\cos^4 \alpha} - 1\right) x^2 \tag{7.4}$$

Neglecting higher order terms of equation 6.4 for simplicity, the equation for curve 'ADC' in 'XOY' plane may be given as:

$$y = \left(\frac{h_i}{\tan \alpha}\right) \left[\left(\frac{2x \tan \alpha}{h_i}\right) + 1\right]^{1/2} \tag{7.5}$$

The equation of preform top surface in 'XOY' plane is a circle and may be expressed as:

$$x^2 + y^2 = R_0^2 \tag{7.6}$$

The coordinates of points 'A' and 'C' can be obtained by simultaneously solving equations 6.5 and 6.6 and are given as:

$$\left(x_A, y_A\right) \equiv \left(-\frac{h_i}{2\tan\alpha}, 0\right) \tag{7.7}$$

a)

$$\left(x_C, y_C\right) \equiv \left\{\left[R_0 - \frac{h_i}{\tan\alpha}\right], \left[\left(\frac{h_i}{\tan\alpha}\right)\left(\frac{2R_0\tan\alpha}{h_i} - 1\right)^{1/2}\right]\right\} \tag{7.7}$$

b)

The equation for curve 'ADC' may also be expressed in polar coordinates as [159]:

$$r = \left[\frac{h_i}{\tan\alpha(1+\cos P\theta)}\right] = \left[\frac{2R_0 Q}{(1+\cos P\theta)}\right] \tag{7.8}$$

where,

$$Q = \left(\frac{h_i}{2R_0\tan\alpha}\right) \text{ and } P = \left(\frac{\pi}{2\alpha}\right)$$

7.1.2 Parametric Analysis

During axial feed of the lower die, the contact area between the dies and Aluminium cylindrical preform increases from zero and attain a certain value rapidly, and then increases gradually. As the upper conical die rotates / oscillates about the axis of the die, the small indented contact area is swept over the entire cylindrical surface leading to the decrease in the height of the preform. Figure 7.4 shows the variation of total displacement on the Aluminium cylindrical preform at different percentage of reduction when half cone angle of upper conical die is 5^0, die velocity is 1 mm/sec, angular velocity is 10.47 rad/sec and interfacial frictional coefficients is 0.05. The result has been plotted arbitrarily at any instance of rotary forging process and it can be noticed that maximum displacement / deformation is at the central region of the preform, which is due to the axial feed of the lower die. The maximum displacement observed is about 4.24 mm at the central region and this gradually decreases towards the periphery. The maximum radial displacement been observed is 1.94 mm, which is comparable with the

experimental results. As the process continues, the top surface tends to become flat and the indented area is swept over the entire preform top surface.

Figure 7.5 shows the effective stress distribution on the cylindrical preform during at different percentage of reductions. It was found that the high stress zones are located at the contact areas between the die and preform, and then it progresses along the circumferential direction. With increase in the percentage of height reduction, the complete preform has developed the stress zone and the stress concentrations are higher at the contact areas. The maximum effective stress observed was about 145 MPa at the central region.

Figure 7.6 shows the distribution of the effective strain on the cylindrical preform at different percentage of reductions. As the upper die is already indented to a very small amount, during the action of axial feed of lower die and orbital motion of upper conical die, the contact surface at the central region near the upper conical die is under plastic deformation state. With reduction in height, this plastic deformation zone grows gradually towards radial direction and axially towards the lower end surface of the preform. The plastic deformation being larger near the upper die and preform contact surface as compared to the lower die contact surface, mushroom shape of the deformed preform was seen. When the height reduction was 25%, the maximum and minimum effective strain values observed were 3.47 and 0.457, respectively.

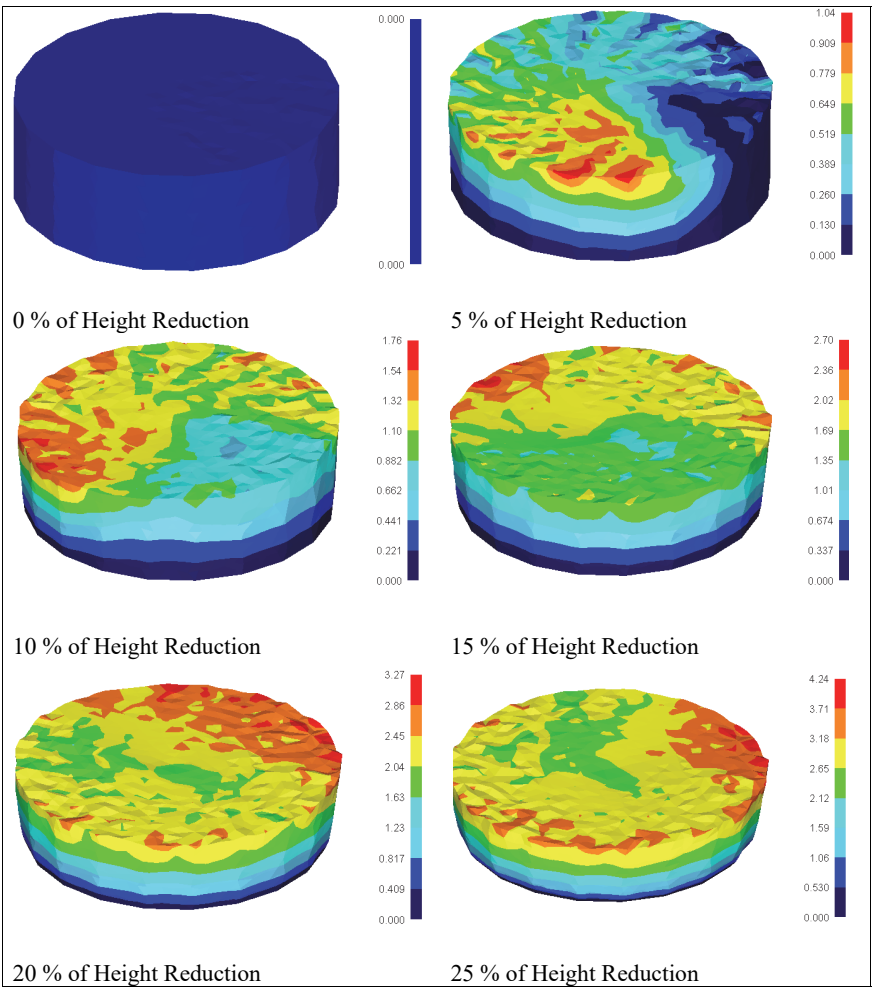

Figure 7.4: Variation of Total Displacement on the Cylindrical Preform during Rotary Sinter-Forging at different % of Height Reductions.

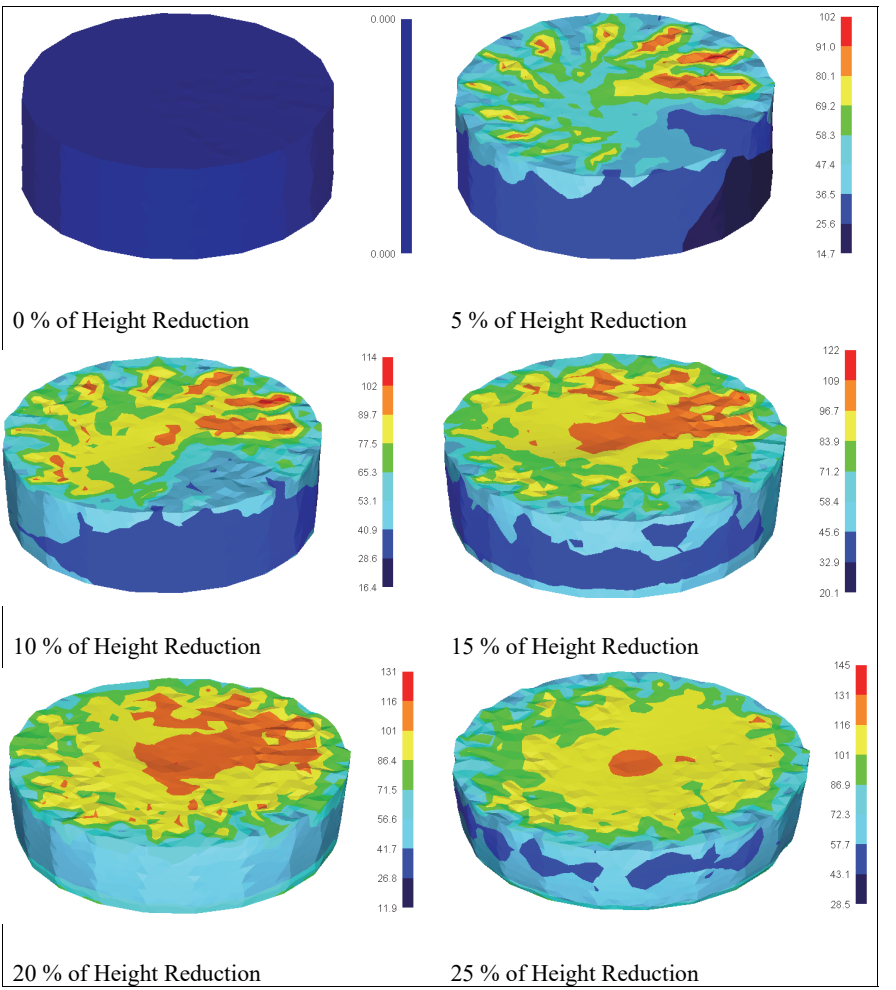

Figure 7.5: Variation of Effective Stress Distribution on the Cylindrical Preform during Rotary Sinter-Forging at different % of Height Reductions.

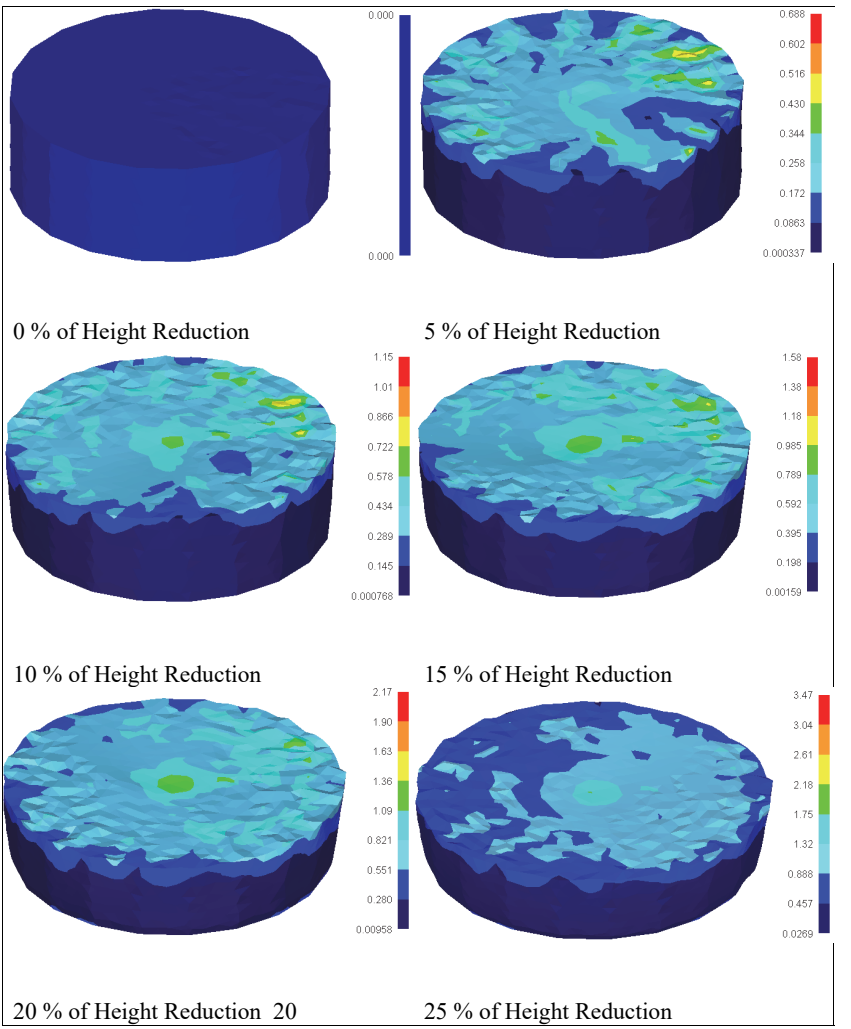

Figure 7.6: Variation of Effective Strain Distribution on the Cylindrical Preform during Rotary Sinter-Forging at different % of Height Reductions.

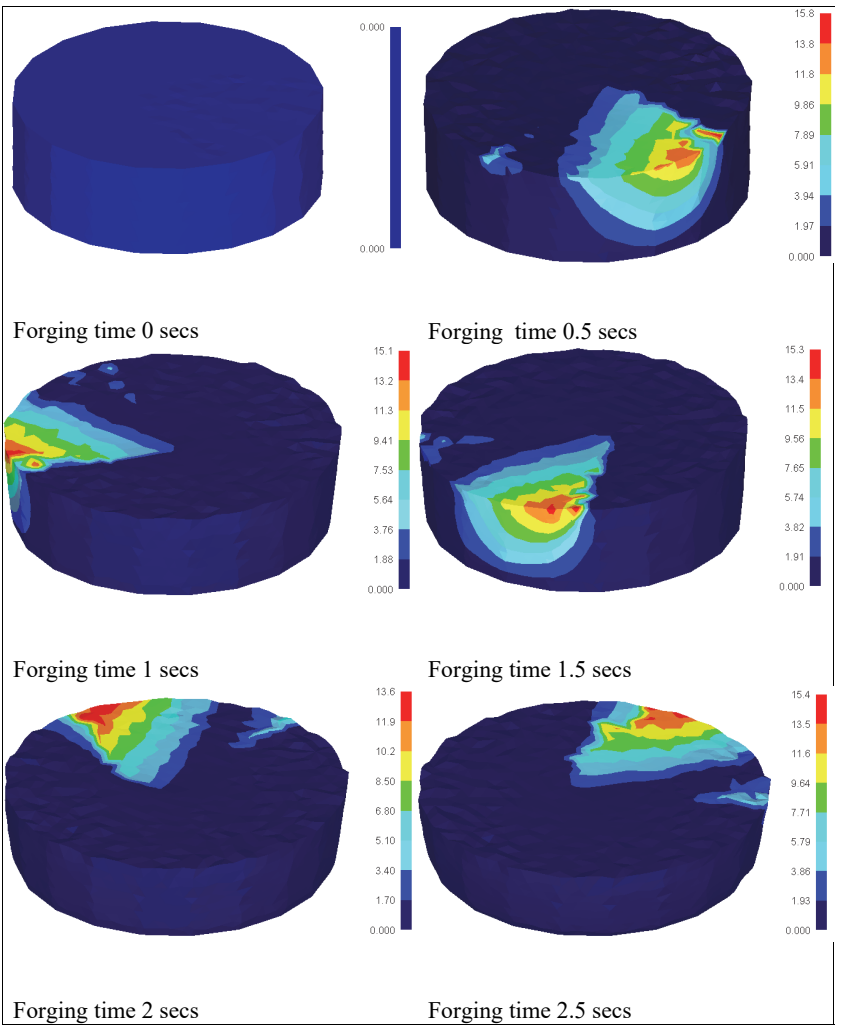

Figure 7.7: Velocity Distribution on the Cylindrical Preform during Rotary Sinter-Forging at different Forging Times.

Figure 7.7 shows the velocity distribution on the cylindrical preform during rotary sinter-forging at different forging times. The maximum velocity in the order of 7.65-15.3 mm/sec was found on the peripheral and vertical surfaces of the preform at the time of forging, which were flowing radially outwards and the least velocities were observed at the central regions of the preform.

Figure 7.8 shows the variation of change in the diameter of the upper surface of the cylindrical preform during rotary sinter-forging with forging time. It can be seen that the simulation results are in good agreement with experimental ones after 25% of height reduction with the maximum relative error of approximately 3.5%.

Figure 7.9 shows the variation of the contact area between the upper die and preform at different half cone angles of upper conical dies during rotary sinter-forging with the height reduction. As the nature of contact surface between the upper conical die and preform is dynamic with respect to the contact area size and position (due to oscillatory/rotary motion), its analysis is bit complicated. The contact area is found to increase rapidly initially with the indentation and then remain fairly constant. The steady state is reached at the end of the intermittent axial and rotary motion of the dies.

Figure 7.10 (a) and (b) shows the variation of the average forging load during rotary sinter-forging with height reduction for different die velocities, angular velocities and interfacial friction conditions. It was observed, the die load was maximum during higher die velocity of the lower die and at lower angular velocity of the upper conical die under low interfacial frictional condition.

Figure 7.10 (c) shows the variation of average die load during rotary sinter-forging with of height reduction at different half cone angles of the upper conical die. It is observed that the die loads are maximum for lower tilt angle and lower interfacial frictional condition. With the increase of the inclination or tilt angle of the upper die (half cone angle), the deformation becomes more inhomogeneous and the die load and angular moment gradually decreases. It was noticed that the metal flow and degree of inhomogeneous deformation of preform can be more effectively controlled by the tilt angle with smaller feed amount per revolution, while the die load and moment can be

more effectively controlled by the tilt angle with a larger feed amount per revolution (indentation depth). The variation of internal energy dissipation with height reduction for different die velocities during rotary sinter-forging is shown in figure 7.11. It is observed at the beginning of rotary forging process, the internal energy dissipation starts from minimum value and with the increase in forging time or height reduction, the value increases gradually. The curves for energy dissipation are higher for lower tilt angle or half cone angles. This is due to the fact that lower tilt angles/half cone angles will generate larger contact area and hence higher die loads to carry the deformation leading to higher energy consumption, thus, losing the main advantage of rotary-forging over conventional flat-die forging of lower die loads. It may be concluded that rotary forging process must be carried with higher half cone angle dies or higher tilt angles or higher skew contact angles, satisfying the developed 3D FE model as a reasonable one.

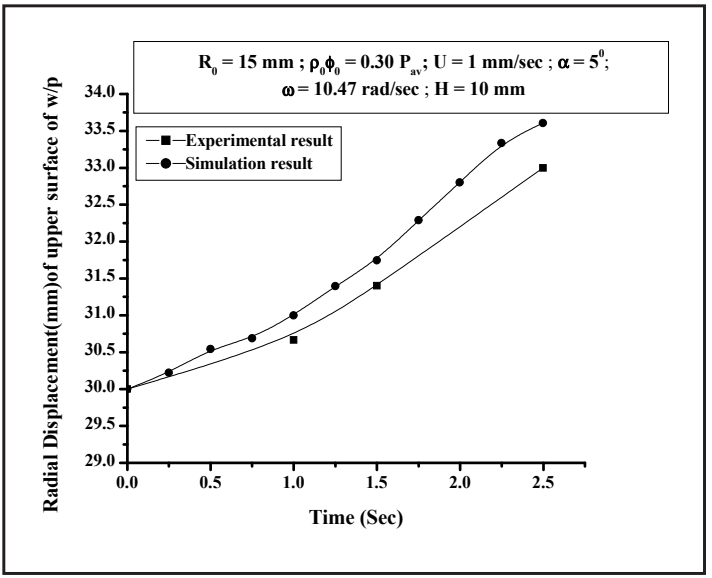

Figure 7.8: Variation of Diameter of Upper Surface of the Cylindrical Preform during Rotary Sinter-Forging.

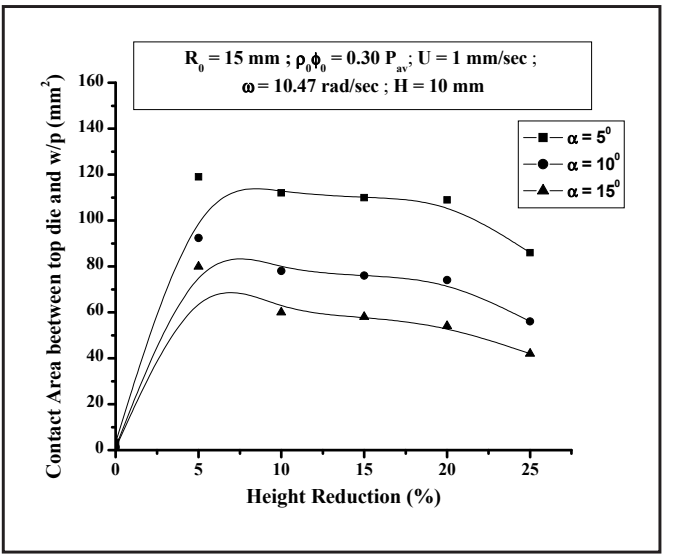

Figure 7.9: Variation of Contact Area with Height Reduction during Rotary sinter-Forging.

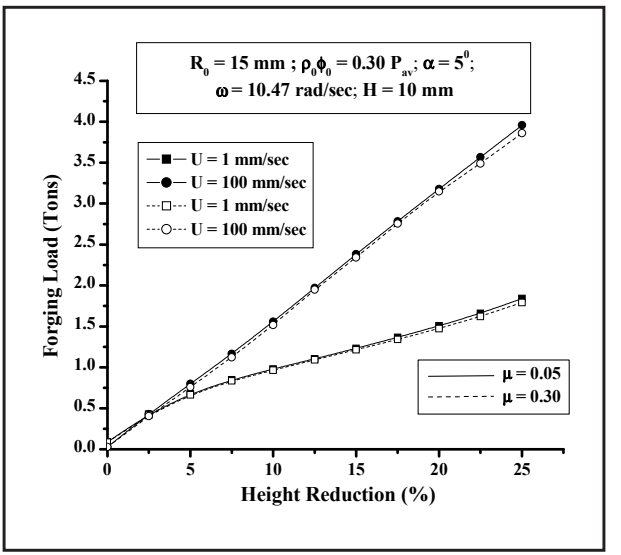

Figure 7.10 (a): Variation of Forging Load with Height Reduction during Rotary Sinter-Forging for different Die Velocities.

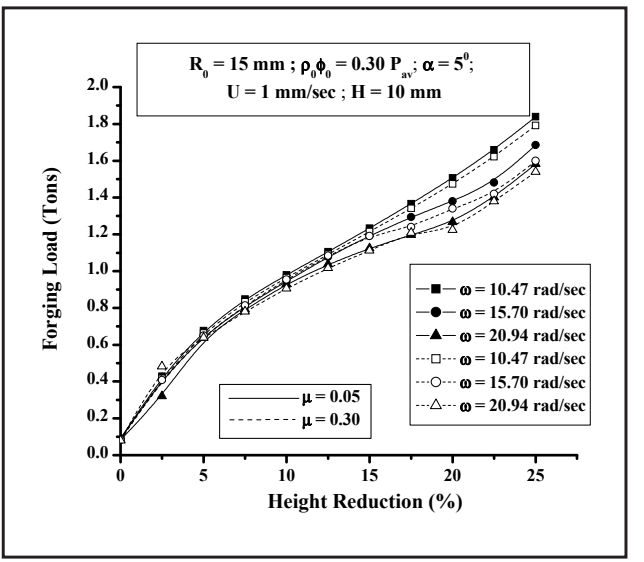

Figure 7.10 (b): Variation of Forging Load with Height Reduction during Rotary Sinter-Forging for different Angular Velocities.

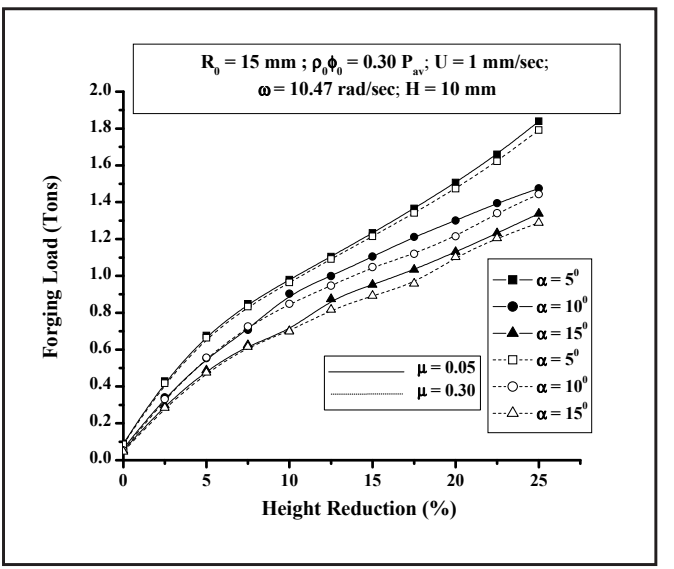

Figure 7.10 (c): Variation of Average Die Load with Height Reduction during Rotary Sinter-Forging for different Half-Cone Angles of Upper Conical Dies.

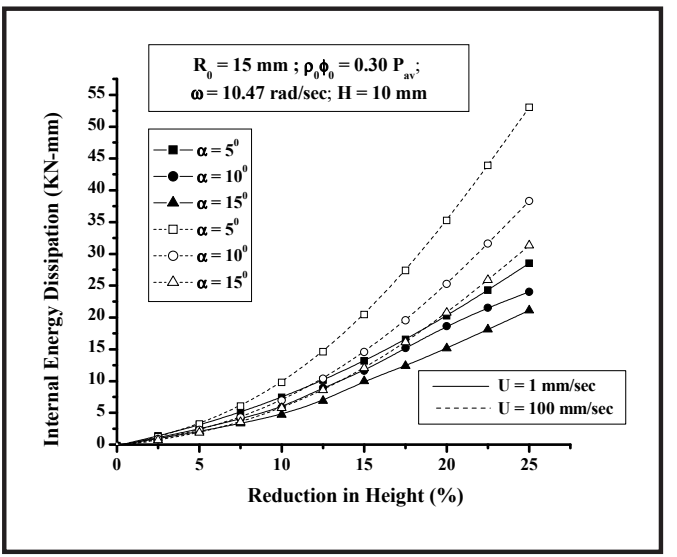

Figure 7.11: Variation of Internal Energy Dissipation with Height reduction during Rotary Sinter-Forging for different Half-Cone Angles and Die Velocities.

CHAPTER 8

CONCLUSIONS AND SCOPE FOR FUTURE WORK

The research work in the present thesis clearly established the significance of both experimental and finite element simulation based investigations onto deformation characteristics during sinter- forging process of aluminium preforms. The effect of die velocity on effective stress, effective strain, effective strain-rate, total internal energy dissipation, average die load, flow velocity and other related deformation characteristics at room temperature has been critically explored. Preforms with three different generic shapes *i.e.* hollow, truncated conical and irregular trapezoidal have been considered under open-die sinter-forging process, followed by the investigations into flashless closed-die sinter-forging of cylindrical preforms into double-hub flange components and rotary sinter-forging of axi-symmetric preforms. Entire computational modeling and simulation results presented here have been obtained using codes of DEFORM^{TM} finite element software, which considers the material model as porous and large strain model based on the implicit Lagrangian finite element codes.

During investigations various deformation characteristics, like percentage in height reduction, change in radius, corresponding forging load and preform relative densities, on sintered aluminium preforms, with different shape complexity factors during open die, flashless closed-die and rotary based sinter-forging process was conducted considering different velocities with high and low interfacial friction conditions.

The results and discussion clearly pointed out that deformation behavior effects significantly with increase in the die speed during various sinter-forging processes and hence, must be considered during analyses. The research work in the present thesis may be summarized into important conclusions along with major conclusions, which are as follows:

- The compact relative density increases with decrease in powder particle size, due to better consolidation of powder particles, when are in the order of 40 microns or less. Increases with increase in compaction pressure, sintering temperature due to decrease in the inter particles pore sizes leading to the better consolidation of the powder particles within the deforming compacts and due to some kind of diffusion process happening within the performs during sintering, which leads to better bonding between the powder particles, as well as, decreases the inter particle pore sizes.
- The compacts with higher l/d ratio show more densification as compared to the shorter ones because of better material flow, and increases with increase in height reduction and become comparable to that of wrought materials at the end of forging operation. The lubricated performs exhibit better densification than the unlubricated ones.
- The forgeability of the sintered compacts without the occurrence of cracks was evaluated, and it was found to be about 42% (in case of compact having higher l/d ratio under lubricated interfacial friction conditions i.e. vaseline lubricant on die and preform surface). As l/d ratio decreases, the forgeability also decreases and it is found to be low and vary between 30 to 35 percent under dry friction conditions.
- The curve between axial strain and forging load for sintered material was plotted and was found to be quite different from that of the wrought materials and steels. The curve is found to be asymptote along x-axis and the strain increases very slowly initially. This is attributed due to the simultaneous compaction and compression of the compacts. This indicates that some amount forging load and energy are expended during the compact densification.

  Thus confirming that, the interfacial friction condition, preform densification and yield criterion for sintered porous material are the cornerstones of the present research work and strongly influence the forging of sintered materials.

- During finite element simulation on sinter-forging processes of hollow preforms, the deformation of hollow preforms had revealed two different types of flow behavior of inner diameter with smaller value of percent change, depending upon the interfacial frictional conditions. The direction of material flow (frictional shear stress) depends upon the position of neutral radius. When the neutral radius lies within inner radius, the material flows throughout in outward direction on the hollow disc preform, when it lies in between the inner and outer radii of the hollow preform, the flow of material observed flowing inwards for inner region and outwards for outer region. In truncated conical preform, it is seen the lower surface of the preform has been displaced maximum and the upper surface minimum due to the upper stationary die and lower moving die and due to low magnitude of interfacial friction at smaller diameter. The sinter-forging of irregular polygonal preform pointed that there is some kind of symmetry in material flow about the planes passing through the proposed engraved lines on the preform top surface. The lines remain straight during sinter-forging operation, confirming that there is no shear flow or velocity jumps along the boundaries of proposed velocity zones. The flow of material, bulging characteristic is uniform in all the lateral sides of preform, satisfying the regions being having kinematically admissible velocity field.
- The relative density of sintered preforms has been found to increase with increase in the die velocity, forging load and percent height reduction. The preforms deformed under higher die velocities has been found to be more densified, as compared to those deformed at lower die velocities, probably due to the impact loading and small contact time. The preforms deformed under rotary sinter-forging has been found to be less densified, as compared to the preforms deformed under open-die and closed-die sinter-forging operations, due to small forging loads. The preform densification has been found to be highest at the end of die filling during closed-die sinter-forging operation, as compared to other sinter-forging operations and becomes almost comparable to that of corresponding wrought metals at the end.

- The variation of effective strain and effective stress with the percentage in reduction of height was found to increase exponentially initially and then remain fairly constant at the end of the upset-forging operation. The effective stress was found to be higher for lower die velocity and preforms with smallest inner radius, whereas the effective strain was found to highest for the highest die velocity with smallest inner radius of the preform during finite element simulation of hollow preforms. In case of sintered conical aluminium preforms the effective stress and effective strain were found to increase gradually initially but fairly rapidly later on. Whereas in irregular trapezoidal preforms effective stress was found to increase rapidly during the initial stage of deformation, where as effective strain exhibited the same behavior during the end of deformation.
- The variation of internal energy dissipations with shape-complexity factors during open-die sinter-forging of different preforms has also been investigated. It has been found that the energy requirements are higher for enclosing shapes of preform *e.g.* internal energy dissipation is higher for enclosing cylindrical shape of preform, as compared to the actual truncated conical preform. This has been attributed due to the large amount of sintered material associated with such enclosing shapes.
- The forging load requirement for hollow disc, truncated conical and irregular polygonal preforms has also been compared for the same amount of deformation, sintered material, interfacial friction condition and die velocities. It has been found that the forging load required to deform irregular polygonal preform is higher than truncated conical, which is further higher than hollow disc preform. This has been attributed due to high constraint deformation associated with the irregular polygonal preforms and better radial flow of material in case of hollow disc preforms. And also, increase in forging load and total energy dissipations during deformation with die velocity confirmed the importance of inertia effects during high-speed deformation processes.
- During finite element simulation of, it is observed that the effective stresses and effective strains for H/D_o ratios at different die velocities with the percentage change in height reduction, was found to increase exponentially initially and then

remain fairly constant at the end of the sinter-forging operation. The effective stress and effective strain was found to be higher for lower H/D_o ratio preforms. The preforms with higher aspect ratio deforms at higher forging loads, exhibits higher percent change in height, as compared to the shorter preforms and make contact with die container walls earlier. The contact area is large for same forging load, as compared to the shorter preforms, leading to high interfacial friction shear energy dissipations.

- The variation of external energy supplied by die platens with percentage of height reduction, during flashless closed-die sinter-forging of cylindrical preform into double-hub flange component, found to increase exponentially with the die movement, indicating that inertia power dissipation is appreciable at high-speed deformation, the curves are lower, at lower shape complexity factor and higher value at lower die velocity indicating increase in inertial power requirement.
- The forging load decreases with die velocity and increases exponentially with the die cavity fills during complete filling stage i.e. forcing of sintered materials into the cavities of impressions. This is because sinter-forging operations at higher die speeds are characterized by very small contact time under load, which restricts the internal heat generated during plastic working to dissipate quickly and hence, reduces the resistance of sintered materials against deformation.
- During finite element simulation of rotary sinter-forging of axi-symmetric preform, it's been found, the average forging load with % of height reduction with respect to axial feed is found maximum for higher die velocity and maximum for lower die velocity with change in angular velocities under low interfacial frictional condition. The final rotary forging load at different 'α 'angles found to be maximum for lower tilt angle under lower interfacial frictional condition and with increase in inclination or tilt angle of the upper die, the deformation becomes more inhomogeneous and the axial forging load and angular moment gradually decreases.
- The variation curves of internal energy dissipation with % of height reduction for different die velocities during rotary sinter-forging. It is observed at the beginning of cold rotary forging process, the internal energy dissipation starts from zero

value and with the increase in forming time or % of height reduction, the value increased gradually with lower tilt angle, satisfying the developed 3D FE model as a reasonable one.

- The effective stress distribution on the axi-symmetric cylindrical preform during rotary sinter-forging process at different percentage of reductions. It is found that the stress zone is maximum at the contact areas between the die and preform at first, and then it progresses along the circumferential direction. With increase in percentage of height reduction, the complete preform has developed the stress zone and the stress concentrations are higher in the contact areas at that instant of process and rest of non- contact area with relatively smaller values of effective stress. Effective strain on the axi-symmetric cylindrical preform during rotary sinter-forging at different percentage of reductions found to be maximum at the central region near the upper die which satisfies the yield condition at early stage and comes to the plastic deformation state, with further reduction in height, this plastic deformation zone grows gradually towards radial direction and axially towards the lower end surface of the preform. The plastic deformation being larger near the upper die and preform contact surface then the lower die contact surface, mushroom shape of the deformed preform is seen.

It is expected that the present research work will be useful for understanding the complex interaction among various deformation characteristics during cold open-die forging of sintered preforms having complex profiles. Also, the finite element simulation performed along with the modeling of material properties, interfacial composite frictional conditions, yield criterion and compatibility conditions can be effectively utilized to investigate the deformation behavior of such sintered materials.

REFERENCES

1. Kuhn H. A. & Lawley A., “Deformation characteristics of iron powder compacts”, Modern Development in Powder Metallurgy, Princeton, vol. 4 (1970) p. 463.

2. Cull G. W., “Mechanical and metallurgical properties of powder forging”, International Journal of Powder Metallurgy, vol. 13/26 (1970) p. 156.

3. Davies R. & Mark J. B., “The production of components by forging of powder preforms”, Proceedings of 13th International MTDR Conference, Birmingham, UK, (1972) p. 463.

4. Antes H. W., “Powder forging fundamentals”, ASM Source Book on Powder Metallurgy, Compiled by Bradbury S., Ohio, US, (1979) p. 144.

5. Brown G. T. & Jones P. K., “Experimental and practical aspects of powder forging process”, International Journal of Powder Metallurgy, vol. 6, No. 4 (1970) p. 29.

6. Nishino Y. Kirigaya S. & Mitsubishi Kinzoku K.K., “Elimination of sintering steps in powder metallurgy hot forging process”, Modern Development in Powder Metallurgy, Princeton, vol. 9 (1976) p. 509.

7. “Ctrp_0407_powder_forged_connecting_rods”, http://www.circletrack.com/enginetech.

8. Downey C. L. & Kuhn H. A., “Designing powder metallurgy preforms for forging axisymmetric parts”, ASM Source Book on Powder Metallurgy, Compiled by Bradbury S., Ohio, US, (1979) p. 129.

9. Jones P. K., “The technical and economic advantage of powder forged products”, International Journal of Powder Metallurgy, vol. 13 (1970) p. 114.

10. Wisker J. W. & Johns P. K., “The economics of powder forging relative to competing processes-present and future”, Modern Developments in Powder Metallurgy, Princeton, vol. 7 (1974) p. 33.

11. “Powder metallurgy and particulate materials”, Vision and technology road map, U.S. Department of Energy, Office of Industrial Technologies, (2001).

12. “European Powder Metallurgy Association”, www.epma.com/economic-advantages.

13. “Powder metallurgy growth in automotive market”. A report by Ryuichiro Goto, APMI (2003).

14. “State of the PM Industry in North America-2011”, Michael E. Lutheran, President, Metal Powder Industries Federation.

15. Sutradhar G., Jha A.K. & Kumar S., “Production of sinter-forged components”, International Journal of Materials Processing Technology, Elsevier, vol. 41 (1994) p.143.

16. “Powder Metallurgy Growth in the Automotive Market Brazil”, Technical Program Committee, American Powder Metals Industries (APMI) International.

17. “Metal Powders to 2015” published by The Freedonia Group in December (2011).

18. “The story of Powder Metallurgy in India”, http://www.ipmd.net/articles/001197.html, 29th March, (2011).

19. Rama Mohan T.R, Consultant Powder Metallurgy, “Ceramics and Diamond Tools”, Asian Metallurgy Summit (2011).

20. Antes H. W., “Present status and potential of powder metallurgy forming”, Powder Metallurgy in Defense Technology, vol. 3, (1977), p. 29.

21. Krishna B.V., Venugopal P. & Rao K. P., “Use of powder metallurgy preform as a alternating to produce bimetallic tubes”, Material Science & Technology, vol. 21, No. 6 (2005) p. 630.

22. Kobayashi S., Oh S.I. & Altan T., “Metal forming and the finite element method”, Series in Advance Manufacturing, Oxford University Press (1989).

23. Jeswiet J., Geiger M., Engel U., Kleiner M., Schikorra M., Duflou J. & Neugebauer R., “Metal forming progress since 2000”, CIRP Journal of Manufacturing Science & Technology, vol. 1, p. 2.

24. “DEFORM User’s Manual 2000”, Scientific Forming Technologies Corporation, Columbus, Ohio.

25. Hirschhorn J.S., “Introduction to Powder Metallurgy”, American Powder Metallurgy Institute, (1976), p.3.

26. Morgan W. R. & Sands R.L., “Isostatic compaction of metal powders”, Metals and Materials, vol. 3, No. 5 (1969), p. 85.

27. Alexander J. M. & Quainton D. R., “On the isostatic compaction and hydrostatic extrusion of iron powder”, Proceedings of the 12th International MTDR Conference, Birmingham, UK, (1971), p. 51.

28. Shima S. & Oyane M., “The inter-relation between density and hardness in the isostatic compaction of powders”, Proceedings of the 13th International MTDR Conference, Birmingham, UK, (1972), p. 471.

29. Fischmeister H. F., “Powder compaction: fundamentals and recent developments”, Proceedings of Institution of Mechanical Engineers, UK, vol. 196 (1982), p. 105.

30. Stein E. M., Rvan J., Orsdel. & Schneider P.V., “High velocity compaction of iron powder, Metal Progress”, vol. 85 (1964), p. 83.

31. Wang S. & Davies R., “Some effects of high speeds in metal powder compaction”, proceedings of the 9th International MTDR Conference, Birmingham, UK, (1968), p. 331.

32. Elwakil S. D. & Davies R., “High-speed compaction of metal powders”, Proceedings of the 13th International MTDR Conference, Birmingham, UK, (1972), p. 435.

33. Vitvaz P. A. & Roman O. V., “Impulse compacting of powder materials”, Proceedings of the 13th International MTDR Conference, Birmingham, UK, (1972), p. 442.
34. Kumar K. S., Lawley A. & Antes H.W., “Thermal mechanical processing of iron powder for high compressibility”, Proceedings of Europe International Powder Metallurgy Conference, Florence, (1982), p. 437.
35. Wang J. C. & Nadkarni A.V., “Theoretical analysis of powder compaction and density distribution in long parts”, International Journal of Powder Metallurgy, vol. 37 (1981), p. 371.
36. Biner S. B. & Spitzig W. A., “Densification of iron compacts with various initial porosities under hydrostatic pressure”, Acta Metallurgica, vol. 38 (1990), p. 603.
37. Kim H. S., “Densification mechanism during hot isostatic pressing of stainless steel powder compacts”, International Journal of Material Processing Technology, Elsevier, vol. 123 (2002), p. 319.
38. Jha A.K., "Deformation characteristics and fracturing of sintered copper powder strips during cold forging", Journal of Mechanical Working Technology, vol. 16 (1988), p. 145.
39. Chandramouli R., Pandey K.S., Kandavel T.K., Ashokkumar T. & D., “Influence of material flow constraints during cold forming on the deformation and densification behavior of hypoequited P/M ring performs”, Springer-Veloog London Limited (2006), p. 6.
40. Zape G., “The mechanical properties of hot pre-compacted iron-nickel sintered alloys”, International Journal of Powder Metallurgy, vol. 13, No. 26 (1970), p. 130.
41. Ward M. & Biullington J. C., “Effect of zinc stearate on apparent density, mixing and compaction and ejection of iron powder compacts”, International Journal of Powder Metallurgy, No. 4 (1979), p. 201.
42. Lindskog P., “The effect of phosphorous additions on the tensile, fatigue and impact strength of sintered atomized iron powder”, Source Book on Powder Metallurgy, ASM, 1979.

43. Kao A. & Koczak M. A., “Mixing and compacting behavior of ferrous powders”, International Journal of Powder Metallurgy and Powder Technology, vol. 16 (April-1980), p. 105.
44. Hwang B. & Kobayashi S., “Deformation characterization of powdered metals in compaction, International Journal of Machine Tool and Manufacture”, Pregamon, vol. 30 (1990), p. 309.
45. Brakpool J., “The effect of material characteristics on the compaction behavior of metal powders”, International Journal of Powder Metallurgy, vol. 48 (1992), p: 423.
46. Hamiuddin M. & Upadhyaya G. S., “Effect of nickel during sintering of iron containing phosphorus”, International Journal of Powder Metallurgy and Powder Technology, vol. 16 (1980), p. 57.
47. Hamiuddin M. & Upadhyaya G. S., “Effect of molybdenum during sintering of iron and iron phosphorus premix”, Powder Metallurgy, No. 3 (1980), p. 136.
48. Borland W. J. P. Evans J.P., Mardon P.G., Sutcliffe P.W. & Waldron W.B., “Effect of purity on sintering behavior and properties of iron compacts produced from fine powders”, Powder Metallurgy, No. 3 (1980), p. 146.
49. Tengzelius J. & Blande C. A., “High temperature sintering of powder metallurgy steels”, Proceedings of Europe International Powder Metallurgy Conference, Florence, (1982), p. 331.
50. Green R. J., “A plasticity theory for porous solids”, International Journal of Mechanical Sciences and Engineering, ASME, vol. 14 (1971), p. 215.
51. Downey C. L. & Kuhn H. A., “Deformation characteristics and plastic theory of sintered powder materials”, International Journal of Powder Metallurgy, vol. 7 (1971), p. 15.
52. Elwakil S. D., “Plasticity of sintered iron powder compacts”, Proceedings of 15th International MTDR Conference, Birmingham, UK, (1974), p. 68.
53. Shima S. & Oyane M., “Plasticity theory for porous metals”, International Journal of Mechanical Sciences and Engineering, ASME, vol. 18 (1976), p. 285.
54. Lewis R. W. & Khoei A. R., “A plasticity model for metal powder-forming processes”, International Journal of Plasticity, vol. 17 (2001), p. 1659.

55. Tabata T. & Masaki M., “A yield criterion for porous metals and analysis of axial compression of porous discs, Memories of Osaka Institute of Technology”, Series-B, Science and Technology, vol. 22, No. 2 (1978), p. 45.
56. Thomas J. T., “A new yield function for compressible powder metallurgy materials”, International Journal of Mechanical Sciences and Engineering, ASME, vol. 26 (1984), p. 527.
57. Kim K. T., Suh J. & Y. S. Kwon, “Plastic yielding for cold isostatically pressed and sintered porous iron under tension and torsion”, International Journal of Powder Metallurgy, vol. 33 (1990), p. 321.
58. Lee D. N. & Kim H. S., “Plastic yield behavior of porous metals”, International Journal of Powder metallurgy, vol. 35 (1992), p. 275.
59. Akisanya A. R., A.C.F. Cocks & N.A. Fleck, “The yield behavior of metal powders”, International Journal of Mechanical Sciences and Engineering, ASME, vol. 39 (1997) p. 1215.
60. Griffiths T. J., Davies R. & Bassett M.B., “Compactability equations for the powder forging processes”, International Journal of Powder Metallurgy, No. 4 (1976), p. 214.
61. Justino J.G., Alves M.K., Klein A.N. & Al-Qureshi H.A., “Constitutive model for the elastic-plastic analysis of porous sintered materials”, International Journal of Machine Tools and Manufacture, Elsevier, vol. 44 (2004), p. 1471.
62. Nakagawa T. et. al., “On the cold forging of sintered iron powder performs”, Proceedings of the 13th International MTDR Conference, Birmingham, UK, (1972), p. 455.
63. Huppmann W. J., “The effect of powder characteristics of the sintered forging process”, International Journal of Powder Metallurgy, vol. 13, No. 1 (1977), p. 36.
64. Standring P. M. et. al., “Theoretical investigation and analysis: powder compaction and sinter forging”, Journal of Mechanical Working Technology, Elsevier, vol. 4 (1980), p. 7.
65. Tabata T. & Masaki S., “Determination of the coefficient of friction in forging of porous metals from ring compression”, Journal of Mechanical Sciences and Engineering, ASME, vol. 20, No. 8 (1978), p. 505.

66. Tabata T., Masaki S. & Hosokawa K., "A compression test to determine the coefficient of friction in forging powder metallurgy preforms", International Journal of Powder Metallurgy and Powder Technology, vol. 16/2 (1980), p. 149.
67. Kim K. T., "Elastic-plastic responses of porous metals under triaxial loading", International Journal of Solids Structure, vol. 24 (1988), p. 937.
68. Kim K. T. & Suh, J, "Elastic-plastic strain hardening responses of porous metals", International Journal of Engineering Sciences, vol. 27 (1989), p. 767.
69 Kim K. T. & Kown Y. S., "Strain hardening response of sintered porous iron tubes with various initial porosities under combined tension and torsion", Journal of Engineering Materials and Technology, ASME, vol. 114 (1992), p. 213.
70. DeSilva M. G. & Ramesh K. T., "The rate-dependent deformation of porous pure iron", International Journal of Plasticity, vol. 13 (1997), p. 587.
71. Difai M. A., "The effect of presintering conditions on the cold forgeability of powder preform", Proceedings of the 15th International MTDR Conference, Birmingham, UK, (1974), p. 651.
72. Forguson B. L., Kuhn H.A., & Lawley A., "Fatigue of iron base powder metallurgy forgings", Modern Development in Powder Metallurgy, Princeton, vol. 9 (1977), p. 51.
73. Suh S. K. & Kuhn H. A., "Fracture modes and their prevention in powder metallurgy preforms", Modern Development in Powder Metallurgy, Princeton, vol. 9 (1977), p. 407.
74. Tiwari H. N. & Sharan R., "Forgeability evaluation of iron powder preform", Proceedings of 10th International MTDR Conference, Durgapur, India, (December-1982).
75. Chitkara N. R. & Liaghat G. H., "Working pressure, deformation modes and fracture in open-piercing of cylindrical disks made of compacted sintered aluminium powder", International Journal Advanced Manufacturing Technology, vol. 17 (2001), p. 889.
76. Marx J. B. et. al., "Some considerations of the hot forging of powder preforms", International Journal of Advanced Machine Tool Design and Research, Pregamon, vol. 10 (1971), p. 456.

7. Fischmeister H. F., Aren B., & Eastering K. E., “Deformation and densification of porous preforms in hot forging”, International Journal of Powder Metallurgy, vol. 14, No. 27 (1971), p. 144.
78. Cook J. P., “Manganese steels for powder metallurgy hot forming, International Journal of Powder Metallurgy and Powder Technology”, vol. 10, No. 1 (1974), p. 345.
79. Im. Y. T. & Kobayashi S., “Coupled thermo-viscoplastic analysis in plane-strain compression of porous materials”, Advanced Manufacturing Processes, vol. 1 (1986), p. 269.
80. Wang P. T. & Zaidi M. A., “Thermomechanical deformation of powder-based porous aluminium: part I. Evolution of pore structure”, International Journal of Powder Technology, vol. 66 (1991), p. 9.
81. Wang P. T. & Zaidi M. A., “Thermomechanical deformation of powder”, International Journal of Powder Technology, vol. 66 (1991), p. 21.
82. Rahman M. A., Sheikh M. N. E. I., “Workability in forming of powder metallurgy compacts”, Journal of Materials Processing Technology, Vol. 54 (1995), p. 97.
83. Huang C. & ChengJ., “An investigation into the forming limits of sintered porous materials under different operational conditions”, Journal of Materials Processing Technology, Vol. 148 (2004), p. 382.
84. Narayanasamy R. , Ramesh T. & Pandey K. S. “Some aspects of workability studies in cold forging of pure aluminium powder metallurgy compacts”, Material Science & Technology (2005), p.6.
85. Pokorska I., “Powder metallurgy materials in hot forming”, Institute of Materials, Minerals & Mining (2007), p-4.
86. Sutradhar G., Jha A.K. & Kumar S., “Cold forging of sintered iron-powder preforms”, International Journal of Materials Processing Technology, Elsevier, vol. (1995).
87. Das P., Sutradhar G., Chakraborty T., Patra S. & Mitra M., “Cold forging of sintered hollow polygonal disks with barreling”, Journal of Materials Science, Vol. 43 (2008), p. 3180.

88. Ibhadode A. O. A. & Dean T. A., “The influence of process variables on load and accuracy when forging in a completely closed cavity die”, Journal of Mechanical Engineers, vol. 202, No. B-4 (1988), p. 237.
89. Kwan C. T., “An analysis of the closed-die forging of a general non-axisymmetric shape by the upper-bound elemental technique”, International Journal of Materials Processing Technology, Elsevier, vol. 123 (2002), p. 197.
90. Altan T. & Fiorentino R.J., “Prediction of loads and stresses in closed-die forging”, Transactions of the Journal of Engineering for Industry, ASME, vol. 93 (1971), p. 477.
91. Singh S., Jha A.K. & Kumar S., “Upper Bound Analysis of Flashless Closed Die Sinter-Forging of Cylindrical Preform into Double-Hub Flange Component”, International journal of Manufacturing Technology & Research vol.3, (2007), No. 1&2, p. 68.
92. Altan T. & Henning H. J., “Closed-die forging of round shapes flash design and material savings”, Metallurgia and Metalforming, vol. 24 (1971), p. 83.
93. Shen G. Im Y.T. & Altan T., “Effect of flash dimensions and billet size in a closed-die forging of aluminum alloy part”, Proceedings of XVII NAMRC, Ohio, (1989), p. 34.
94. O’Connell M., Brett painter, Gary maul & Taylan altan, “Flashless closed-die upset forging-load estimation for optimal cold header selection”, International Journal of Materials Processing Technology, Elsevier, vol. 59 (1996), p. 81.
95. Takemasu T., Victor Vazquez., Taylan Atlan. & Brett Painter., “Investigation of metal flow and preform optimization in flashless forging of a connecting rod”, International Journal of Materials Processing Technology, Elsevier, vol. 59 (1996), p. 95.
96. Lee J., Young-Ho Kim. & Won-Byoung Bae., “A study on flash and flashless-precision forging by the upper-bound elemental technique”, International Journal of Materials Processing Technology, Elsevier, vol. 72 (1997), p. 371.
97. Akgerman N., Becker J. R., & Allan T., “Preform design in closed-die forging”, Metallurgia and Metalforming, vol. 26 (1973), p. 135.

98. Kim J. Y. & Chitkara N. R., “Determination of preform shape to improve dimensional accuracy of the forged crown gear form in a closed-die forging process”, International Journal of Mechanical Sciences, Pergamon, vol. 43 (2001), p. 853.
99. Stranding P.M. & Appleton E., “The kinematic relationship between angled die and workpiece in rotary forging”, Proceedings of 1st International Conference on Rotary Metal Working Processes, London, UK, (1979), p. 275.
100. Kubo K. & Hirai H., “Cold forging of powder preforms by the rotary forging technique”, Journal of Japan Society of Technology for Plasticity, vol. 18 (1977), p. 165.
101. Zhang M., “Calculating force and energy during rotating forging”, Proceedings of 3rd International Conference on Rotary Metal Working Processes, Japan, (1984), p. 115.
102. Jeswietm J., Geiger M., Engel, U. Kleiner, M., Schikorra M., Duflou J. & Neugebauer R., “Metal forming progress since 2000”, CIRP Journal of Manufacturing Science & Technology, vol. 1, (2008), p. 2.
103. Hayama M., “Theoretical analysis of rotary forging of cylindrical rod”, Journal of Japan Society for Technology of Plasticity, vol. 24 (1983), p. 386.
104. Kobayashi M., “Deformation behavior in simultaneous forward-backward extrusion upsetting by rotary forging”, Proceedings of 3rd International Conference on Rotary Metal Working Processes, Japan, (1984), p. 13.
105. Marciniak Z., “Rotary upsetting of flanges in warm forming temperature range”, Proceedings of 3rd International Conference on Rotary Metal Working Processes, Japan, (1984), p. 23.
106. Choi S., “Upper-bound analysis of the rotary forging of a cylindrical billet”, International Journal of Materials Processing Technology, Elsevier, vol. 67 (1997), p. 78.
107. Hwang B. & Kobayashi S., “Application of the finite element method to powdered metal compaction processes”, International Journal of Machine Tool & Manufucturing, (1991), p. 31, 123.

108. Im Y.T. & Kobayashi S., “Finite element analysis of plastic deformation of porous materials”. Metal Forming and Impact Mechanics., Pergamon Press, Oxford, (1985), p. 103.
109. Im Y.T. & Kobayashi S., “Analysis of axi-symmetric forging of porous materials by finite element method”. Advance Manufacturing Processes, vol. 1 (1986), p. 473.
110. Im Y.T. & Kobayashi S., “Finite element applications in forming billet and P/M preforms”. Proceedings of Euromech Colloquium on Modelling of Metal Forming Processes, Kluwer Sci., (1988), p. 217.
111. Ranek M. N., Aly Badawy. & Jong Jin Park., “Simulation of densification in powder metal forging”, International Journal of Materials and Manufacturing, ASME,, vol. 98 (1988), p. 340.
112. Fereshteh-Saniee F. & Jaafari M., “Analytical, numerical and experimental analyses of the closed die forging”, International Journal of Materials Processing Technology, Elsevier, vol. 125-126 (2002), p. 334.
113. Altan T., “Computer simulation to predict load, stress and metal flow in an axisymmetric closed-die forging, Metalforming: Interrelation Between Theory and Practice”, Edited by Hoffmanner A. L., Plenum Publishing Corporation, (1971), p. 249.
114. Majerus J. N., Jen K.P. & Gong H.” Quantitative comparison between precision closed-die forging-force data and computer simulations”, Journal of Engineering Materials and Technology, ASME, vol. 114 (1992), p. 465.
115. Jolgaf M., A.M.S Hamouda, S. Sulaiman & M.M Hamdan., “Development of a CAD/CAM system for the closed-die forging process”, International Journal of Materials Processing Technology, Elsevier, vol. 138 (2004), p. 436.
116. Kwan C. T., “A concave circular parallelepiped element and its applications to three-dimensional closed-die forging”, International Journal of Materials Processing Technology, Elsevier, vol. 123 (2002), p. 203.
117. Guangchun W., Kemin X. & Yan L., “Methods of dealing with some problems in analyzing rotary forging with the FEM and initial application to a ring workpeice”, Journal of Materials Processing Technology, vol. 73 (1997), p. 299.

118. Jang D.Y. & Liou J.H., “Study of stress development in axi-symmetric products processed by radial forging using a 3-D non-linear finite-element method”, Journal of Materials Processing Technology, vol. 74 (1998), p. 74.
119. Wang G. & Guoqun Z., “A three-dimensional rigid plastic FEM analysis of rotary forging deformation of a ring workpiece”, Journal of Materials Processing Technology, vol. 95 (1999), p. 112.
120. Yuan S., Wang X., Liu G. & Cho D., “The precision forming of pin parts by cold-drawing and rotary-forging”, Journal of Materials Processing Technology, vol. 86 (1999), p. 252.
121. Liu G., Yuan S.J., Wang Z.R. & Zhou D.C., “Explanation of the mushroom effect in the rotary forging of a cylinder”, Journal of Materials Processing Technology, vol. 151 (2004), p. 178.
122. Ameli A. & Movahhedy M.R., “A parametric study on residual stresses and forging load in cold radial forging process”, International Journal of Advanced Manufacturing Technology, vol. 33 (2007), p. 7.
123. Han X. & Hua L., “3D FE modeling simulation of cold rotary forging of a cylinder workpiece”, Materials and Design, vol. 30 (2009), p. 2133.
124. Han X. & Hua L., “3D FE modeling of cold rotary forging of a ring workpiece”, Journal of Materials Processing Technology, vol. 209 (2009), p. 5353.
125. Deng X., Hua L., Han X. & Song Y., “Numerical and experimental investigation of cold rotary forging of a 20CrMnTi alloy spur bevel gear”, Materials and Design, vol. 32 (2011), p. 1376.
126. Domblesky J.P., Shivpuri R. & Painter B., **“**Application of the finite-element method to the radial forging of large diameter tubes”, Journal of Materials Processing Technology, vol. 49 (1995), p: 57.
127. Lippmann H., “On the dynamics of forging, Proceedings of the 7th International MTDR Conference”, Birmingham, UK, (1966), p. 53.chit
128. Hilllier M. J., “Estimation of dynamic forces in very high speed impact forging”, Journal of Engineering for Industry, ASME, vol. 88 (1966), p. 369.

129. Osakada K., Oyane m. & and Tanaka. H., “Mechanical properties of mild steel after cold and warm high-speed forging”, Proceedings of the 12th International MTDR Conference, Birmingham, UK, (1971), p. 357.
130. Dean T. A. & Sturgess. CEN., “Dynamic effects during high-velocity compression testing”, Proceedings of the 12th International MTDR Conference, Birmingham, UK, (1971), p. 363.
131. Jones M. G. & C.E.N Sturgess., “Estimation of dynamic forces in high-speed compression using a free-flight impact forging device”, International Journal of Mechanical Sciences, ASME, vol. 13 (1971), p. 309.
132. Tobias S. A., Seikh A.D., Dean J.A. & Das M.K., “The effect of impact speed and lubricant in hot forging: Part 1. Interface friction and die cavity pressure”, Proceedings of the 9th International MTDR Conference, Birmingham, UK, (1968), p. 341.
133. Tobias S. A., Seikh A.D., Dean J.A. & Das M.K., “The effect of impact speed and lubricant in hot forging: Part 2. Metal flow and forging loads”, Proceedings of the 9th International MTDR Conference, Birmingham, UK, (1968), p. 347.
134. Chitkara N. R. & Bhutta M. A., “Dynamic heading of triangular, hexagonal, and octagonal shaped heads at high impact velocities: some experiments and an analysis”, International Journal Advanced Manufacturing Technology, vol. 18 (2001), p. 332.
135. Jha A.K. & S. Kumar, “Dynamic effects during high-speed sinter-forging process”, International Journal of Machine Tool Design and Research, Pergamon, vol. 36 (1996), p. 1109.
136. Singh S., Jha A.K. & Kumar S., “Analysis of dynamic effects during high-speed forging of sintered preforms”, Journal of Materials Processing Technology, 112(1), (2001b), p. 53.
137. Singh S., Jha A.K. & Kumar S., “Dynamic effects during sinter-forging of axi-symmetric hollow disc preforms”. International Journal of Machine Tools Manufacturing, 47(7-8), (2007a), p. 1101.

138. Singh S., Jha A.K. & Kumar S., "Upper bound analysis and experimental investigations of dynamic effects during sinter-forging of irregular polygonal preforms", Journal of Materials Processing Technology, 194(1-3), (2007b), p. 134.
139. Jha A.K. & Kumar S., "Forging of metal powder preform", International Journal of Machine Tool Design and Research, Pergamon, vol. 23/4 (1983) p. 201.
140. Lawley A., Chin Gilbert Y. (Ed.)., "Advances in Powder Technology", (1981) ASM Materials Science Seminar, ASM, New York, (1982).
141. Zhdannovich G. M., "Theory of Compacting of Metal Powders"', Translated from Teorizc Pressovaniya Metzllichaskikli Poroshkov, (1969) by the ForeignTechnology Division, WPAFB, Ohio, U.S.A. (Translation No. FTD-HC-23-77570) (29 June, 1971) pp. 1.
142. Kuhn H.A., "Deformation Process of Sintered Powder Metal, Ch. 14, Powder Metallurgy Processing: New Techniques and Analysis", Academic Press, New York (1978), p.99.
143. Zhang M., "Calculating force and energy during rotating forging", Proceedings of 3rd International Conference on Rotary Metal Working Processes, Japan, (1984), p. 115.
144. Doraivelu S., "A new yield function for compressible PM materials". International journal of Mechanical Sciences and Technology, (1984), p.527.
145. Mohanty T., "Upset-Forging Of Sintered Aluminium Truncated Conical Preforms", Advances In Production Engineering & Management/18546250, 20110601
146. Chandrasekhar P. & Singh S., FEM Simulation, Experimental Investigation and Upper Bound Analysis of Open-Die Forging of Sintered Truncated Conical Preforms of Aluminium Metal Powder, 3rd International & 24th All India Manufacturing Technology Design & Research - 2010 (AIMTDR – 2010). International Conference.
147. Chandrasekhar P. & Singh S., Analysis of Net-Shape Closed-Die Sinter-Forging of Centrally Located Cylindrical Preforms, SENRA Academic Publishers,

Burnaby, British Columbia, Canadian journal of pure and applied sciences, Vol. 5, No. 1, pp. 1419-1428, Feb 2011.

148. Chandrasekhar P. & Singh S., Finite Element Simulation of Cold Open-Die Forging of Sintered Aluminum Metal Powder Trapezoidal Preforms, Trends in Mechanical Engineering & Technology: An International Journal, Consortium e-Learning Network, STM Journal, 1 (2-3), pp: 18-28, 2011.

149. Chandrasekhar P. & Singh S., Investigating the Effect of Compaction Characteristics, Compact Shape and Interfacial Friction Conditions during Forging of Sintered Metallic Compacts, International Journal of Materials Sciences, 6 (3), pp: 357-371, 2011.

150. Chandrasekhar P. & Singh S., Investigation of Dynamic Effects during Cold Upset-Forging of Sintered Aluminium Truncated Conical Preforms, Journal of Materials Processing Technology, Elsevier, 211, pp: 1285-1295, 2011.

151. Chandrasekhar P. & Singh S., Finite Element Simulation of Forging of Aluminium Truncated Conical Sintered Preforms, Journal of Production Engineering, Institution of Engineers (India), 92, pp: 14-18, Sep 2011.